Trinity College Dublin
Coláiste na Tríonóide, Baile Átha Cliath
The University of Dublin

Tuneable plasmonic metasurfaces for on-chip beam steering applications using Vanadium dioxide

---

Matthieu Proffit

Supervisor: Pr Louise Bradley

School of Pysics

Trinity College Dublin, *the University of Dublin*

D02 PN40

Ireland

March 2023

A dissertation submitted to the University of Dublin in partial fulfilment of the requirements for the degree of MSC *(physics)*

Declaration

I declare that this thesis has not been submitted as an exercise for a degree at this or any other university and it is entirely my own work.

I agree to deposit this thesis in the University's open access institutional repository or allow the Library to do so on my behalf, subject to Irish Copyright Legislation and Trinity College Library conditions of use and acknowledgement.

I consent to the examiner retaining a copy of the thesis beyond the examining period, should they so wish (EU GDPR May 2018).

I have read and I understand the plagiarism provisions in the General Regulations of the University Calendar for the current year, found at http://www.tcd.ie/calendar.

I have also completed the Online Tutorial on avoiding plagiarism 'Ready Steady Write', located at http://tcd-ie.libguides.com/plagiarism/ready-steady-write.

Matthieu Proffit 08/2022

I would like to thank particularly my supervisor, Pr Louise Bradley for helping me throughout this project in the best possible way, with regular meetings, relevant papers, great support to write a paper and finally offering me the opportunity to finish the year with this MSc. I have to mention all the efforts from Stephen, especially at the beginning of the year to introduce me to the group and all the equipment training I went through with him. Finally, on a less scientific note, I would like to thank DUHAC and all the friends I made there, who made this year in Ireland a special one, I wish to come back there soon and keep these friendships in the future!

Contents

List of Figures

Nomenclature

Abbreviations

IMT	Insulator to Metal Transition
LIDAR	Light Detection And Ranging
MIT	Metal to Insulator Transition

Geometric variables

p	Array period [nm]
t_{Au}	Au layer thickness [nm]
t_{SiO_2}	SiO_2 layer thickness [nm]
t_{Ti}	Ti layer thickness [nm]
t_{VO_2}	VO_2 layer thickness [nm]
w	Antenna width [nm]

Variables

Φ	Phase angle [° or rad]
θ_i	Angle of incidence [° or rad]
θ_r	Angle of refraction (possibly anomalous) [° or rad]
φ	Vanadium dioxide phase (0=dielectric, 1=metallic)

Abstract

Resonant optical phased arrays are a promising way to reach fully reconfigurable metasurfaces in the optical and near-infrared (NIR) regimes with low energy consumption, low footprint, and high reliability. Continuously tunable resonant structures suffer from inherent drawbacks such as low phase range, amplitude-phase correlation, or extreme sensitivity that makes precise control at the individual element level very challenging. In this thesis, we introduce and investigate 1-bit (binary) control for beam steering as a control algorithm to bypass these issues. We consider a metasurface for beam steering using a nanoresonator antenna and explore the theoretical capabilities of such phased arrays.

Vanadium dioxide (VO_2) is a promising phase change material that exhibits a reversible structural transformation at a temperature of $\sim 68°C$ with its electromagnetic behaviour switching from dielectric to metallic. This broad optical properties modulation is easily triggered and makes VO_2 a prime candidate for tunable nanophotonic structures. A thermally realistic structure based on VO_2 sandwiched in a metal–insulator–metal structure is proposed and optimized using inverse design to enhance its performance at 1550 nm. Continuous beam steering over 90° range is successfully achieved using binary control, with excellent agreement with predictions based on the theoretical first-principles description of phased arrays. Furthermore, a broadband response from 1500 to 1700 nm is achieved. The robustness to the design manufacturing imperfections is also demonstrated. This simplified approach can be implemented to optimize tunable nanophotonic phased array metasurfaces based on other materials or phased shifting mechanisms for various functionalities.

Simultaneously, in this thesis we will observe that these nano-antennas are capable of significant amplitude modulation if tuned appropriately. If this effect is not desirable for phased arrays, it can be enhanced for color generation and narrowband or broadband tunable reflector applications. We investigate a simple switchable thin-film structure and compare its amplitude modulation capabilities compared to resonant structures.

Chapter 1

Introduction

For centuries, optical components were created using bulk components of various refractive indexes where light accumulates phase over a path much longer than its wavelength. With the advent of nanofabrication techniques, it has been demonstrated that manipulating light using metasurfaces was possible and could yield performances comparable if not better than bulk elements like lenses or prisms. As to this date, most optical metasurfaces have a functionality fixed at fabrication, the future of such metasurfaces is reconfigurability post-fabrication. Creating tunable metasurfaces would allow entire complex optical systems to be manufactured on-chip at a lower cost, with better reliability and energy efficiency.

Light Detection and Ranging (LIDAR) systems are of great interest to enhance machine vision capabilities, notably for the automotive industry that is putting tremendous R&D efforts into autonomous vehicles. The current use of complex mechanical systems to achieve beam steering at acceptable rates ($\sim$1 million points per second) over a large number of resolvable points (640*16 for the Valeo Scala LIDAR) yields high production costs and reliability issues. Flash LIDARs scan the entire field of view all at once but require high-energy flashes to receive enough photons in the detectors and therefore need large VCSEL arrays that are expensive and energy consuming.

RADAR systems encountered similar problems in the mid-20th century as the massive antenna required to obtain a sharp beam could not be steered mechanically fast enough. The use of phased arrays enabled fast scanning rates over a wide far-field with no moving parts by controlling the phase of a cluster of radio-waves emitters. Down-sizing phased arrays in the optical and NIR domain is no small task as the technologies used to control centimetric waves are not applicable to radiation at wavelengths of the order of a micron.

There are many challenges associated with such a technological breakthrough. At that scale,

nanofabrication techniques must be used which seriously impedes the range of materials and shapes of components. Furthermore, a device must be monolithic as assembling parts is out of the question at that scale. Tunable elements will also have to be included to control an output phase by user-controlled inputs, like a voltage. Several paths have been proposed and tested to achieve sub-wavelength reconfigurable phase control antennas, we will mostly focus on resonant antennas as this solution is simple, compact and energy efficient. A strong light-matter interaction at resonance within such antennas can yield a large phase shift with a relatively small change in wavelength for a given antenna or with a modification in the antenna properties for a given wavelength.
In order to reach full reconfigurability, a tunable element has to be included in each antenna, phase change materials are particularly well suited for this application as they offer a very high index modulation for low energy consumption. Vanadium dioxide (VO_2) in particular showcases an insulator to metal transition (IMT) around 68° that supports a wide optical index change ($\sim$ unity), that can be triggered easily and where intermediate material properties can be obtained. This makes VO_2 the perfect candidate for a tunable element in a resonant antenna phased array to achieve a compact, reliable and energy-efficient solution.
Resonant nanoantennas have already been investigated in the near-infrared (NIR) and optical domain and they suffer from inherent flaws like amplitude-phase correlation, non 2π phase shift and non-linearity between the input signal and output phase shift [1–7]. These flaws are inherently due to the resonant nature of the devices and cannot be individually mitigated without worsening one or more of these three problems. We propose a novel control algorithm, binary control, for beam steering that enables us to ignore all these issues and can be ideally implemented with resonant nano-antennas, unlike the usual ideal control scheme. The binary control algorithm is clear and simple to implement, enables continuous beam steering over a wide field of view and can be applied without any loss of generality to any phased array, regardless of the wave nature or scale.

In chapter 2 of this Thesis, we will first present classical phased array theory, the current state of the art in the optical/NIR domain and how they can be improved based on RADAR research. We will then investigate Vanadium dioxide, its optical properties, behaviour around transition and how it can be manufactured, with an emphasis put on pulsed laser deposition (PLD). We then present a number of articles that have each pushed the boundaries of resonant

optical/NIR metasurfaces in the past decade with theoretical and experimental investigations.

Chapter 3 will focus on theory, deriving a number of equations that will be useful later in the thesis and theoretically analysing binary control. We will see how well it performs compared to ideal control, the challenges associated with this novel control mode and how they are addressed. The robustness of binary control to manufacturing inaccuracies is also to be discussed as they are frequent in resonant nanostructures. The finite difference time domain (FDTD) method will also be shortly analysed as it is the main method used in this project to analyse the nanostructures, we will finish by a thorough description of the FDTD setups we used in this research project.

We will then focus in chapter 4 on inverse design, this design technique was used in this project to find and fine-tune a nanostructure with success. An overview of the subject will be provided to the reader along with a brief explanation of the common challenges associated with inverse design. The two algorithms we used are then presented along with their advantages and drawbacks. We motivate their choice in the final section as there are many methods to implement inverse design in practice.

In chapter 5, we will outline the design of a realistic resonant nanoantenna capable of dynamic phase control that ideally implements binary control in the NIR. We explain in detail the design process to achieve an individual thermally controlled phase shift for each antenna in a phased array and assess the performance of the structure. We also present variations on the design that have been obtained using the same design ideas but with different input design parameters like the operating wavelength, array period, or materials. This chapter will present in more detail work that has been published before the submission of this thesis, we refer to this article for a more concise version [8].

As we will see later, resonant nanostructures are capable of amplitude modulation, while this effect is problematic in phased arrays, it can be exploited separately in different devices. We will see in chapter 6 how VO_2 driven nanostructures are capable of reflectance modulation in the optical/NIR domains, for narrowband or broadband applications or even colour

generation.

We finish off this work with a conclusion where we outline future working directions that are certainly promising given the results shown in this thesis.

Chapter 2

Literature Review

2.1 Phased array

2.1.1 Phased array overview

Phased arrays are clusters of wave emitting devices that can achieve phase control for various applications. They are commonly used for beam-steering in the radio-frequency band to achieve very fast scanning rates that would be impossible using mechanical antenna steering. Phased arrays use far-field interference to obtain fully constructive interference in a chosen direction and destructive interference in all other directions. They require phase control at a sub-wavelength level hence their primary use in long radio-frequency waves where it is easier to create phase-modulating devices with sizes lower than the wavelength. Phased array principles can be used for any wave phenomenon, including mechanical waves (sound for example [9]) or optical/NIR applications although the physical implementation would be drastically different in these cases.

2.1.2 Phased array theory

In 1905, Karl Ferdinand Braun demonstrated enhanced transmission of radio waves in one direction [10], the first example of what later became known as phased arrays. With world war 2, and the use of radio waves in the military industry, phased arrays have known an era of development [11] with major industrial outputs like the PAVE PAWS radars. Since 2011 [12], we know that phase discontinuities can be used and tailored to alter the propagation of light, a major application of this idea is beam steering. By precisely modulating the phase discontinuity using a metasurface, we can obtain an anomalous reflection at an angle determined by the metasurface properties. In this subsection, we derive a formula for the phase profile necessary to achieve beam-steering.

Using the variables presented in figure 2.1 we calculate the phase profile to maximise amplitude at a given angle in the Fraunhofer conditions. As we use coherent incident light, all incident rays are in phase. To have maximum amplitude at $\theta = \theta_r$, we need to obtain constructive interference and therefore $\Delta\Phi_i + \Delta\Phi_s + \Delta\Phi(\theta_r) = 0[2\pi]$, with:

- $\Delta\Phi_i = k_0.\Delta x.sin(\theta_i)$ the incident phase delay
- $\Delta\Phi_s$ the phase difference at the metasurface level
- $\Delta\Phi(\theta) = k_0.\Delta x.sin(\theta)$ the reflected phase delay

$\Delta\Phi$ can be calculated for any angle θ, for the special angle of anomalous reflection θ_r only, we verify $\Delta\Phi_i + \Delta\Phi_s + \Delta\Phi(\theta_r) = 0[2\pi]$. We use the following sign conversion to maintain the x-y plots consistent with a increase in angle from left to right.

- + : clockwise angle
- - : counterclockwise angle

We obtain the following equation, usually referred to as the "generalised law of refraction" [12], we note that for regular surfaces with $\Delta\Phi_s = 0$, we obtain Snell's law.

$$sin(\theta_r) = \frac{\Delta\Phi_s}{\Delta x}\frac{\lambda}{2\pi} + sin(\theta_i) \tag{2.1}$$

A constant phase gradient achieves beam steering, by tuning the phase gradient, we can modify the angle of anomalous reflection. To implement this formula exactly over a metasurface, for a reconfigurable device, each antenna has to be able to achieve a 2π phase modulation. The final step, and a crucial one to understand phased array behaviour is the spatial discretisation, as antennas are discrete elements with a finite size, we have to sample the phase profile obtained from equation 2.1 at the antenna center. This sampling will have major effects on the phased array properties as it will create side lobes that can impede the device functionality. A radar detects the reflection from an eventual object and calculates the position of this object as it knows where the beam is directed at a given time : if a side lobe carries enough energy so that its reflection is also detected, one could miscalculate the position of an object. The only way to prevent that is to filter out low-energy reflected waves, the threshold depending on how strong the sides lobes are compared to the main beam, side lobe amplitude has therefore a direct impact on radar sensitivity. Phased arrays are complex

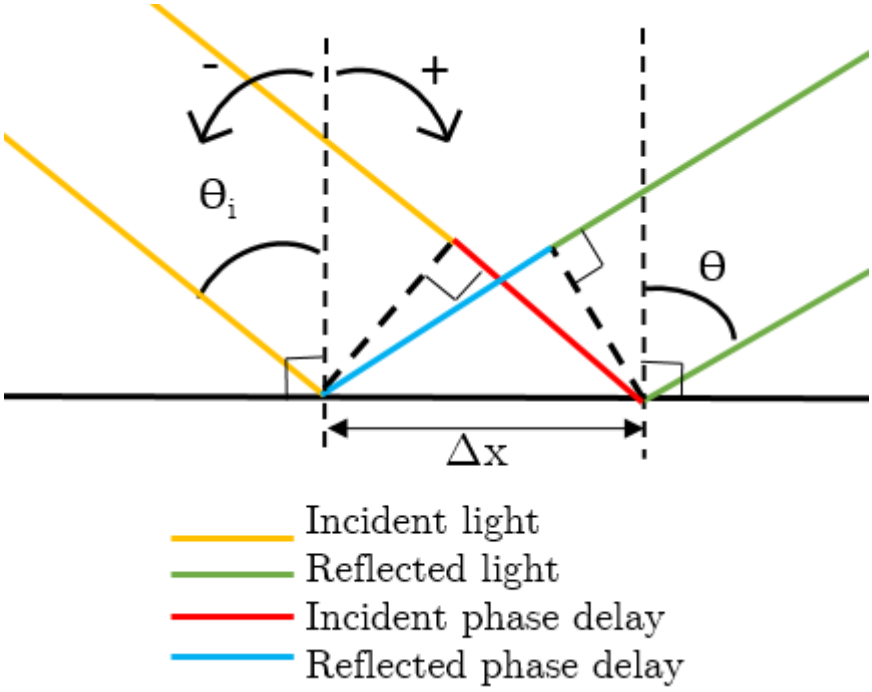

Figure 2.1: Phase delay schematic, Δx is the distance between two adjacent antennas (array period), θ_i is the angle of incidence and θ is the farfield angle that can take any value in $[-\pi/2; \pi/2$.

devices where analytical results are rarely obtained, their study relies on simulations and direct-simulations.

2.1.3 Optical and NIR phased arrays

Phased arrays enabled radars to move to the next level in terms of scanning speed, reliability, and precision compared to their mechanically steered counterparts. It is expected that LIDARS would see the same improvements, thus making them suitable for many machine-vision applications like in the automotive industry. Other applications like open-space optical communications would also benefit from the development of LIDARs The main challenge for optical phased arrays is the size of the components that has to be of the order of nanometers, this limits the variety and shape of the structures that can be used to achieve phase control at a sub wavelength scale. The automotive industry is mostly interested in non-visible radiations for computer vision and two wavelengths of interest have emerged : 905 nm and 1550 nm [13]. They are both transmitted through air and water (for rain/fog conditions) and the mass productions of lasers at these frequencies is achievable. For optical communications, 1550 nm is the wavelength of choice [14] as it minimises losses in optical fibers, a great variety

of lasers around this frequency has been developed and mass-produced which makes future industrial applications more viable.
Optical and NIR phased arrays can be classified into two main types of phase shifters:

- External phase shifters
- Resonant phase shifters

- External phase shifters typically use the thermo-optic effect, the output phase shift results from the change of refractive index with temperature over a long waveguide to change the time taken by light to travel the length of this waveguide [15–17]. As the thermo-optic effect is a very weak effect (for silicon $1,8.10^{-5}K^{-1}$ [18, 19]), it requires either a very long waveguide or a large temperature range, usually both. Efforts are made to lower the electric consumption of such phase shifters which is measured in mW/π, by using spiralling bent waveguides, the heat is used more efficiently over a smaller surface area at the cost of additional transmission losses due to the bends [20]. The repeated temperature modulation is not only power-consuming but also induces thermal stress, thereby decreasing the reliability of such structures. The footprint of such devices is also relatively elevated since it is required to have a waveguide hundreds of times longer than the wavelength for thermo-optic modulation [16] ($300\mu m$ long phase shifters for $\lambda = 488\ nm$). Manufacturing inaccuracies are also a concern as each waveguide is different from its neighbours, therefore inducing phase offsets that require calibration for each device, a costly process for mass production [21]. They can however achieve continuous phase tuning over a 2π range with little intrinsic losses, the most significant losses being due to coupling in and out of the phased array but not to the phase shifters themselves.

- Resonant phased arrays rely on light-matter coupling in a resonant structure to take advantage of the phase shift happening at resonance. They are more ambitious than external phase shifters and promise lower footprint, higher yield for CMOS fabrication, lower power consumption and greater durability. However, their implementation is usually far from ideal as it relies on a resonant phenomenon, several undesirable effects are observed. Namely, non 2π phase shift range, high non-linearity between input signal and output phase and most importantly a high amplitude-phase correlation. Furthermore, a 2π phase shift is never reached over the full tuning range and the tuning techniques can induce another level of

complexity. The structure is usually tuned by changing the property of an element, using several methods :

- Carrier doping, by applying a gate voltage between sandwiched layers, the electronic structure of a material (for example ITO) is modified, which modifies the resonant behavior of the structure [3].
- Electro-optic effect, the Kerr or Pockels effects can be used to tune the refractive index of a material using an electric field [22, 23]
- Phase change material : under specific stimuli, some materials undergo a structural change that largely modifies their optical properties, like VO_2 or GST alloys [1, 24].

Of all these methods, PCMs are the ones that achieve the largest change in index. So far two main types have been investigated for optical metasurfaces applications, VO_2 and GST alloys. The phase of GST (crystallised or amorphous) determines its optical properties, by applying carefully controlled heat pulses, it is possible to tune the proportion of crystallised and amorphous GST. By using a short pulse (order of femtoseconds) to quickly raise a GST element above its melting point followed by a rapid quenching through conduction with the surroundings, we obtain the amorphous phase (RESET pulse). If however we use a longer but weaker stimuli to raise the GST elements above its crystallisation temperature (but below the melting point) for a longer time and control the cooling rate, we can re-crystallise the material (SET pulse). This control scheme can be achieved using femtosecond pulsed lasers [25] or more recently electrically [24] and has also applications in memory storage devices [26]. The later control scheme is a very recent breakthrough and has strong limitations, for example the size of the device and the elevated current density / temperatures it has to endure. Without reset-pulses, it is not possible to obtain amorphous GST and the transition can only go one way, limiting potential applications [27]. GST can also be partially re-crystallised by controlling the quenching rate, it then behaves as an intermediate material which properties are somewhere between the of the fully crystallised or fully amorphous material. The full control of such intermediate amorphisation or crystallisation is very complex and thus limits the use of GST in LIDARs or fully reconfigurable applications. For example, [25] used a femtosecond laser focused on a very small area by a microscope objective controlled by a piezo-electric stage to selectively switch GST elements to obtain a 0.56π phase shift at best which yielded a limited beam steering capability. This is far from constituting a viable

technology for on-chip large-scale applications and a lot of work is left to make GST a suitable material for optical phased arrays. Other devices using GST are switchable : they only have one degree of freedom by using a single GST element for the whole device. For example, Galaretta et al. [28] created a phase gradient metasurface that behaves like a normal reflector when the phase-change layer is in the crystalline state, but reflects anomalously at a predesigned angle when the phase-change layer is switched into its amorphous state. The same author investigated another switchable structure [29] also using GST for beam steering or lensing applications in 2D.

Like GST, Vanadium dioxide (VO_2) also exhibits a large index change when it transitions between its rutile metallic phase and its monoclinic dielectric phase. This change is much easier to trigger than GST as it responds to almost any appropriate external stimulus. The easiest to implement and most commonly used is temperature through localised Joule heating : by applying a current in a nearby conductor, it heats up and triggers VO_2's transition around 68°. The low temperature threshold limits the power consumption and the negative effects associated with repeated heating/cooling cycles. Several metasurfaces devices utilising its promising properties have been designed and experimented on in the past few years after the pioneering work of Kaplan [30] that first had the idea of a tunable metasurface using Vanadium dioxide and that led to limited beam steering capabilities. The most notable progress towards a fully reconfigurable beam-steering metasurface was made by Kim et al. [1] who demonstrated phase shift using nano-antennas experimentally. They were however not thermally isolated from one another so that they could only be tuned altogether by heating the entire device externally. This design however was promising as it displayed a phase shift larger than π (up to 250°), the phase shifting device had sub-wavelength dimensions and could be turned on individually using Joule heating. Solving the thermal cross-talk problem would enable individual element control and the creation of a fully reconfigurable optical metasurface using VO_2. Although this was a significant improvement, major issues relating to the resonant nature of the metasurface were still present, the metasurface reflectance changed significantly through resonance (from 20% down to 5%), the voltage (or more directly temperature) to phase shift relation is highly non-linear and the maximum phase shift was limited to 250° and not 2π. Those problems are all correlated to each other by the proximity to the resonance, if one tries limit the non-linearity or the reflectance modulation, the maximum phase shift

would be reduced. Inversely, obtaining the maximum phase shift yields extremely non-linear voltage-phase relations and a vanishing reflected amplitude at resonance.

2.1.4 Enhancing phased arrays

Steering away from the classical periodic phased array that we described shortly before, it is possible to enhance the overall device performance by modifying some design principles. Two idea can be used :

- Aperiodic phased arrays : the period of the phased array induces side lobes through constructive interference like a grating. By switching to non-periodic arrays constructed using a variety of spacing methods (polynomial, sinusoidal, exponential, random...), we get rid of these side lobes.
- Amplitude tapering : the phased array boundary lead to additional lobes, by reducing the amplitude of the field radiated by the antennas on the side and concentrating the array power in the central antenna, we can reduce side lobe power [31]. This is directly implemented in reflectarrays illuminated by lasers beams as they usually have a Gaussian power density when not spatially filtered by an aperture [32].

These ideas usually enhance the performance of phased arrays but we will ignore them in this project as they introduce another level of complexity in the design. To keep the findings in this thesis more reproducible and to keep the distinction between the performance difference due to the findings we describe and those due to aperiodicity or amplitude tapering clear, we will not implement the later two techniques. A more advanced device implementing these ideas can however be imagined in future investigations.

2.2 Vanadium dioxide

2.2.1 Vanadium dioxide properties

Vanadium dioxide is a material that attracted a lot of attention since the beginning of the century due to its phase transition very close to room temperature ($\simeq 68°C$) : its electrical resistivity and optical properties are widely modified. It has therefore been used in surface coating for smart windows [33], sensors [34], memory devices [26], phase-change switches [35] and neuromorphic computing [36]. In this section, we will mainly focus on the optical properties of VO_2 in the optical and NIR domain as we then develop a device working at 1550 nm.

Vanadium dioxide is rarely found in pure monocrystals. When deposited in thin films, it forms a complex granular structure with various compounds of different stoichiometry. For thin films, the boundary effects are important and can change the structure behavior by inducing compressive or tensile stress in the lattice structure depending on the lattice matching effects with the adjacent layers. Stoichiometry is also rarely perfectly uniform and Vanadium can form various oxides, often found in varying proportions in the same film. It is possible to determine the proportion of each compound (VO,VO_2, V_2O_3, V_2O_5, V_3O_7...) by using XPS and deconvoluting the V-O bounds peaks. If one only wants to verify the presence of Vanadium oxides, x-ray diffraction can identify them with a sharp peak at $2\theta = 39.9\circ$ [37] but cannot distinguish the different phases easily. An easier method to determine if a Vanadium oxide film contains enough VO_2 is to measure changes in conductivity, usually using a 3 or 4 points probe when heated above VO_2's transition temperature (68°). Other Vanadium oxides may showcase a structural transition like VO_2 but at different temperatures, for example 160 K for V_2O_3 [38]. As thin films are never perfect VO_2 monocrystals, their properties would differ depending on the manufacturing process, thickness, substrate, eventual doping and quality of the sample. This explains why VO_2 properties reported in the literature vary from one paper to another, the same effects are however consistent throughout the literature.
Some studies report Vanadium dioxide raw data, others use analytical models to describe its properties, usually using Lorentzian or Drude model fits. In Figure 2.2 - 2.5, we show the optical properties of VO_2 thin films as reported in several studies, which we briefly describe below :

- Verleur et al. [39]: Transmittance and reflectance measurements were conducted between 0.25 and 5 eV for VO_2 bulk crystals and thin films below and above T_c. This was the first study to properly describe the band structure of VO_2, the author used an analytical model to calculate the complex dielectric constant which was fitted using experimental data.

- Kim et al. [1]: The VO_2 optical constants presented in this study were measured from VO_2 thin film on a sapphire substrate with spectroscopic ellipsometry.

- Koussi et al. [40]: 25 nm thick Vanadium oxide films were deposited on silicium and annealed at 450°C. The n and k values were calculated from ellipsometric spectra measured between 300 and 2000 nm at 25 and 85 °C for cold and hot VO_2, respectively.

These experimental results were then fitted with a Tauc-Lorentz formula using 3 oscillators

- Cunningham et al. [41]: The VO_2 optical constants presented in this study were measured from a 30 nm thick VO_2 thin film on a silica substrate by ellipsometry.
- Currie et al. [42] : Reflectance and transmittance measurements were performed on VO_2 thin films grown by ALD with post-annealing in an O_2 rich atmosphere. An analytical model using a sum of oscillators (2 or 3) was then fitted to the experimental data.

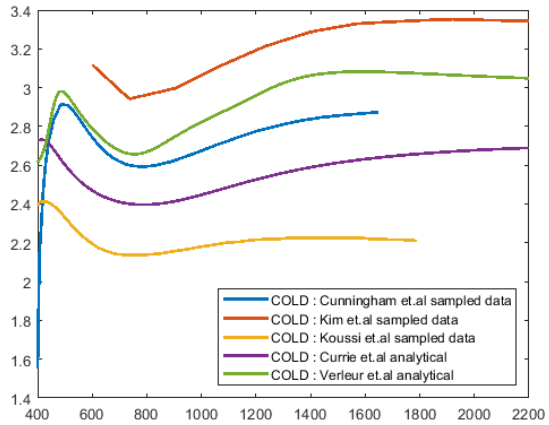

Figure 2.2: n-values for cold VO_2.

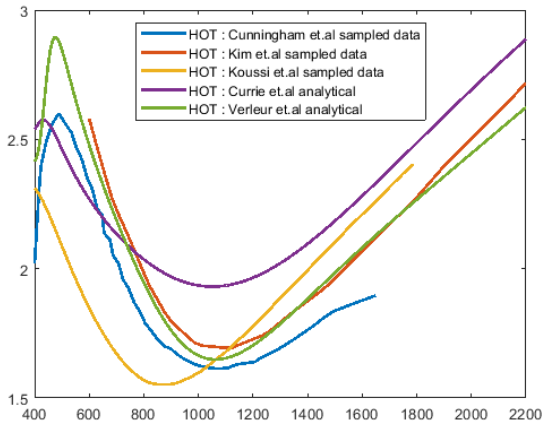

Figure 2.3: n-values for hot VO_2.

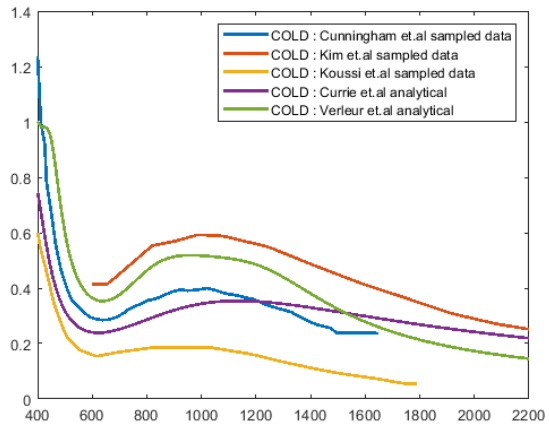

Figure 2.4: k-values for cold VO_2.

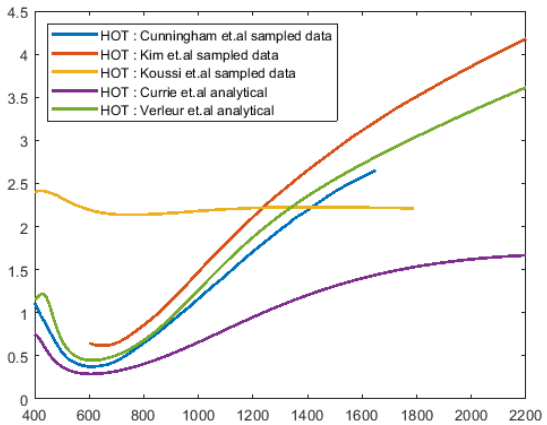

Figure 2.5: k-values for hot VO_2.

The main difference between the cold and hot states is the large increase in the extinction coefficient k and the decrease in optical index n, this is consistent with a transition from a

dielectric to a metal. The large n-contrast at 1550 nm (2.86 to 1.86 for Cunningham et al.) decreases at lower optical wavelengths (2.74 to 2.33 at λ=600 nm for the same author). The interest of VO_2 at these wavelengths is therefore reduced even though this remains by all standards a very high contrast. As a comparison, an index contrast of 0.3 would correspond to an increase in temperature of 2100° for silicon if we extend the linear range of validity of the thermo-optic coefficient (at $1,4.10^{-4}$, which is a rather high value for a dielectric). Of course, that is not practically achievable (Si melting temperature is 1414°), for such high index modulation, only phase change materials are an option even though they come with some drawbacks.

To put it briefly, Vanadium dioxide is a bad dielectric and a bad metal in the sense that it has high losses in its dielectric state and is far from being a perfect conductor in its metallic state. However, its ability to switch from one state to another with a simple stimuli like a small temperature raise makes it an extraordinary material, very promising for many applications that can take advantage of its special properties.

2.2.2 Vanadium dioxide transition

The phenomena driving Vanadium dioxide's structural transition have long been debated as two models could explain the change in properties and both phenomenon seem to appear simultaneously despite having different natures [43]. The first phenomenon is a Peirls distortion due to the lattice structure deformation, this physical modification results in different electron-electron interactions as orbital distances are modified. The second phenomenon is a Mott-Hubard correlated material behavior, electron-electron interactions force them in localised states, resulting in a dielectric material. As the temperature increases, the electron energy ($k_bT/2$) is high enough to escape the potential well it was previously trapped into and conduct electricity : the material becomes conductive. It is now generally agreed that both phenomenon occur and play a role in VO_2 transition, assisting each other so they happen simultaneously (or at least very closely) [43, 44].

The IMT happens almost instantly (switching times in the order of *ps* have been measured [45]) grain by grain [46], and is triggered around defects, hence the importance of grain size and crystallinity [47]. Considering VO_2 volumes larger than a single grain, the transition happens progressively over a range of temperature and showcases a hysteresis (heating and cooling cycles have different paths)[40, 46, 48–51]. Thermal annealing results in two

competing effects. On one hand, it increases the average grain size and crystallinity which decreases the transition and hysteresis temperature width as there is a larger probability to find a nucleating defect in each crystallite. On the other hand, it simultaneously improves crystal perfection and therefore decreases the number of potential nucleation sites, thereby contributing to increase the hysteresis width. With these two competing opposite effects, the shape and width of the hysteresis cycle are determined by crystallinity and grain size [47]. These variables are highly process-dependant, as some applications require a large transition width (i.e for continuous tunability) and some a sharp transition (i.e switches), it is possible to engineer VO_2 thin films properties to suit the application. We can count on a hysteresis width of roughly 5° which is a common value [30] but we keep in mind that this can be modulated by a precise tuning of the manufacturing conditions.

Vanadium dioxide transition can be triggered by a number of physical phenomenons [43], namely :

- Ionic liquid gating induced carrier delocalization [52].
- Electrolyte gating modulation [53].
- Dielectric gating modulation [44].
- Optical excitation, this is probably the way of choice to obtain ultrafast transitions using fs lasers : sub-picosecond structural transition have been observed with a high enough fluence. The authors argued the transition could't be thermally triggered due to the insufficient heat flow triggering the transition [45].
- Compressive or tensile stress [54].
- Electric current modulation on VO2, this method tends to lead to filamentation, a percolative phenomenon where only a filament of material is switched to its metallic state. Current flow in this filament can later trigger transition in its vicinity by Joule heating [55, 56].
- Thermal modulation : the most common transition method although the time scale is not the fastest (of the order of the thermal inertia of the device), the transition is very easy to trigger. [1, 57]

The transition can also be modulated by intrinsic (W doping lowers the transition temperature, depending on its concentration, it can be set below room temperature [58]) and external factors such as lattice matching with the substrate.
The simplest method remains thermal switching, by increasing the temperature above a critical temperature T_c, VO_2 undergoes a progressive IMT with a hysteresis and transition width that can vary based on the manufacturing technique. The characteristic time for thermal switching is governed by thermal inertia as the IMT time is negligible (ps) even when thermal inertia is minimised.

2.2.3 Manufacturing Vanadium dioxide thin films

As stated in the previous sections, the properties of Vanadium dioxides thin films are highly process dependant, thus a good understanding of manufacturing techniques is necessary to obtain high-quality films with the desired properties. Given the number of stable Vanadium oxides that can be obtained, getting just the right stoichiometry and the growth conditions for VO_2 is crucial. Several growth methods are available like electron beam evaporation [59], RF sputtering [59], atomic layer deposition (ALD) [42] or pulsed laser deposition (PLD), we will mostly focus on the use of PLD that has become a widely used thin film deposition method for various materials thanks to its relatively low cost and versatility.
Pulsed laser deposition happens in a controlled atmosphere, usually at low base pressure (typically 10^{-5} to 10^{-6} torr) to enhance the deposition rate. Two main methods exist to obtain Vanadium oxides, reactive sputtering or reactive annealing [60, 61]. In the first method, a Vanadium target is ablated in an O_2 rich atmosphere (O_2 partial pressure usually between 0.01 to 1 torr) where they combine before being deposited on the target. The ablation rate, plume characteristics and O_2 pressure control the stoichiometry of the deposited material. The other method uses a Vanadium thin film that is oxidised post deposition during an annealing phase in an O_2 rich atmosphere, this time, the annealing conditions like temperature, O_2 pressure and time are the main factors that control the stoichiometry of the film. This method has been reported to produce films with smoother morphology and better switching contrast [61] but requires an additional manufacturing step. Even if the monoclinic and rutile phases of VO_2 are the most common ones, others exist and it is possible to obtain them by changing the deposition conditions [62]. These metastable phases are not interesting for us (although they are of interest for other applications) as they do not show the same transition characteristics so we will try to avoid them.

Pulsed laser deposition is not the most repeatable process and the optimal growth settings may vary from one setup to another given the large number of parameters that influence the sputtering conditions. The main parameters that are recorded in most studies and may influence the process are :

- The laser characteristics : wavelength (nm), pulse energy (mJ), fluence (J/cm^2) and pulse rate (Hz)

- The growth conditions : substrate temperature ($°C$), base pressure, O_2 pressure, 0_2 flow rate

- Other setup conditions : substrate material (eventually growth plane if the substrate is crystalline) and target distance

We show in a table in the appendix some growth conditions found in the literature for VO_2 and discuss some of them. McGee et al. [63] used the Taguchi optimisation method to find optimal growth conditions and assess the relative importance of the parameters. It was found that the 0_2 pressure was a very significant parameter (accounting for 73% of the changes of the figure of merit) and the laser fluence the least important (<5%), the substrate temperature (10.75%) and target-substrate distance (10.51%) had intermediate roles in the formation of M_1 VO_2. The optimal conditions were a substrate temperature of $600°C$, target-substrate distance of 31mm, laser fluence of 2.6 J/cm^2 and oxygen pressure of 50 mTorr. The laser pulse rate was fixed at 10 Hz, sputtering time was 15mn and the substrate was thermally grown silicon dioxide (Si/SiO_2), an amorphous material. The definition of "optimality" used for the Taguchi method is rather complex and prone to critique as it takes many factor into account on a subjective scale. Furthermore, the Taguchi method only allows for pre-defined discretised parameter levels and cannot determine precise quantities if they fall between two of the pre-defined steps. However, given the large number of quantities measured to assess film quality, one can be confident in the accuracy of the results of this study, furthermore detailed experimental results were given which may help one to better understand the influence of each parameter in VO_2 growth. Finally, the assessment of the importance of each parameter on film quality reveals an important fact : the 0_2 base pressure is extremely important and outweighs all other settings.

Bukhari et al. investigated the role of 0_2 flow rate using otherwise similar settings ($p_{O2} = 50\ mTorr$, $T = 600°C$, $f_{laser} = 10\ Hz$, fluence of 2.6 J/cm^2, target-substrate distance of 31 mm and Si/SiO_2 substrate) [49]. A range of flow rates between 0.5 to 90 sccm (standard cubic centimeters per minute) was investigated, the proportions of VO_2, V_2O_3 and V_2O_5 measured for each of the 7 samples along with conductivity measurements across transition and a number of characterisation tests. Despite being deposited at the same base pressure, the difference across the samples were major, those being deposited at the lowest flow rates (0.5 and 1 sccm) not even showing a transition in the conductivity measurements. The sample deposited at 50 sccm showcased the best conductivity ratio (almost 10^3) and the one deposited at 30 sccm a stoichiometry very close to the ideal 1/2 V/0 ratio), even though it is not clear which sample can precisely be considered "best", the wide difference in the VO_2 thin film behavior highlights the importance of 0_2 flow rate in PLD.

Room temperature deposition was also investigated, noticeably by Marvel et al. that used post-deposition annealing to manufacture VO_2 thin films. An annealing time of 10mn at $450°C$ with O_2 pressure of 250 mTorr was found to be optimal for three substrates ([100] Si, [0001] Al_2O_3 and SiO_2 glass) [59]. The growth settings were 11 mTorr 0_2 pressure, laser fluence of 4 J/cm^2 at 25 Hz, O_2 flow rate of 2 sccm and target-substrate distance of 80 mm. The post-deposition annealing was necessary to observe a phase transition in all cases (this study also investigates samples produced by RF sputtering and electron beam evaporation) and produced films with RMS roughness values less than 4 nm, the optimal annealing time was assessed by optical switching contrast.

The presence of VO_2 is usually tested by a conductivity measurement over a range of temperature across T_c ($\sim 68°C$), if a significant change is measured, then one can be sure that VO_2 has been obtained, it is however hard to know in which proportion it is present in the film [64]. Other studies use transmittance contrast [59] to show the presence of VO_2 and/or charaterise the hysteretic behavior of the film. In order to know the relative proportion of each stable Vanadium oxide is present, one can use Raman spectroscopy, Rutherford backscattering (RBS) [47] or deconvolute XPS peak data as the binding energy of the $V2_{p_{3/2}}$ peak varies slightly from one oxide to another [42]. Pure Vanadium oxide films are hard to obtain and most studies that used Raman spectroscopy or XPS to test for the presence of other Vanadium oxides found them to some extent. This is however not necessarily a problem

as long as a high index modulation is measured at $T_c = 68°$, which does not necessitate pure VO_2 films.

Manufacturing high quality VO_2 films is crucial in nanophotonics and especially in the structures we present in the following chapters as their performance depends on the n-index contrast. The high process-dependance of VO_2 thin film properties implies that a deep understanding of their manufacturing can improve the quality of the devices. Furthermore manufacturing and engineering constraints have been taken into account to propose a realistic structure, understanding how VO_2 films are formed is necessary to develop a manufacturable structure. For example, polymer coatings for lithography cannot be left during PLD given the necessary heating of the sample either during deposition or in the annealing phase that would damage the coating. Similarly, good lattice matching is required to grow a smooth film, especially for thin layers, thereby encouraging the use of (0001) sapphire, (100) Si, TiO_2, Al_2O_3 as substrate for VO_2 deposition. Lattice matching is optimal with c-plane sapphire (0001), it should also be noted that some amorphous materials like SiO_2 can support VO_2 growth.

2.3 Metasurfaces

In this section, we present studies that use resonant nanoantennas for beam steering applications. We will see several examples, simulation based or experimental, using various phase modulation techniques and operating at different wavelengths. Some of these articles have been mentioned previously but in this section we will present them in greater depth, analyse the advantages and drawbacks and how they have pushed the boundaries of science further. We will begin with the first articles that have set the pace for future, more elaborate work, then focus on papers that investigated the behavior of single resonant antennas. We will continue with simulation based array-scale studies and finish with experimental demonstrations of resonant phased arrays with various degrees of complexity. We otherwise refer the reader to this extensive review article [65] about "optical beam steering with nanophotonics". A more general review of "optical metasurfaces for wavefront control" can be found there [66] and "gradient metasurfaces" there [67].

2.3.1 First studies

One of the first studies that demonstrated beam steering experimentally using resonant elements used a periodic array of resonant elements to achieve phase control [68]. An array comprising 6*6 cylindrical TiO_2 elements of varying diameter (between 60 and 250 nm) was repeated 126*126 times over a 40*40 μm span. This resulted in an anomalous reflection angle of 19.9° at $\lambda = 633$ nm. This structure was not tunable, not even switchable but demonstrated that resonant elements could be used to achieve sub-wavelength control at optical frequencies.

Kaplan et al. [30] imagined the first tunable phased array using VO_2 to achieve beam steering in the NIR (1064 nm). The main idea behind the proposed device was to use a thermal gradient to induce a progressive spatial transition in a VO_2 thin film as shown in figure 2.6a-b. The design used 10 nano-slots antennas with a constant spacing of 100 nm ($\sim \lambda/10$), a maximum phase range of 2.2 rad was obtained which enables beam steering at ±22°. This device had good broadband properties (1000 to 1200 nm) but had a very large FWHM, the two extreme operating states (+22° and −22°) could just be distinguished at FWHM. Furthermore, given the device operating mode that required a temperature gradient, it couldn't be extended to larger phased arrays that span over a total phase amplitude larger than 2π. Nevertheless, it demonstrated the use of phase change materials like VO_2 as realistic options for sub-wavelength phase control in resonant nano-phased arrays.

Further research in the field turned later towards switchable arrays that possess two operating states or even fully reconfigurable phased arrays where each antenna can be controlled individually.

2.3.2 Single antenna study

Several papers focused on single nano-antennas for phase modulation using various modulation techniques.

Kim et al. in 2016 [57] proposed a MIM antenna shown in figure 2.6g using VO_2 as a tunable element and used simulations to assess its behavior around 1550 nm. This study purposefully did not use VO_2 intermediate states to provide continuous phase control but already proposed a sort of binary control. The problems associated with continuous phase control are clearly underlined, noticeably the extreme temperature sensitivity which justifies the use of only two operating states per antenna. However, the authors only proposed pe-

riodic array arrangements which are very limited for beam steering applications given the very small number of possible angles of anomalous reflection. The authors proposed to use their design for beam splitting, the $\pm\theta$ problem is therefore mentioned and partially solved using non-normal incidence. However, the fixed angle of incidence of 20 ° is not sufficient for all angles of anomalous reflection as their pattern #3 still produces a secondary beam. We will see in the next sections how we improve on this paper by using an appropriate angle of incidence and justify the value of this angle mathematically from phased array first principles.

Park et al. in 2017 proposed yet another MIM nanoresonator using ITO as a modulating material and demonstrated this concept experimentally [3]. Carrier concentration in the ITO layer was modulated using an externally applied electric field. At a wavelength of 5.94 μm, a continuous phase shift of 180° was obtained by applying a gate voltage between -40 and +40V. This design shown in figure 2.6e demonstrated phase modulation at the array-scale in an interferometric setup but suffered from high voltage requirements, low reflectance ($\sim 2\%$), high amplitude modulation (72 %) and narrow band functionality. More recently, a more complex structure was proposed and achieved in simulations a phase variation of ∼210° and relatively high reflection amplitude in the 0.45–0.6 range [22]. The amplitude drop at resonance is relatively shallow and the phase shift versus input voltage is not as sharp as can be observed elsewhere.

In 2015, Miao et al. [4] proposed graphene as a resonance modulator in the terahertz regime. A large phase modulation of up to 2π was obtained in a near-perfect oscillator and modulated with a small gate voltage (max 2V). However, the reflected amplitude suffered from a high modulation at resonance (perfect absorption could be reached at resonance), once again showing that phase-amplitude correlation is intrinsically due to the resonant nature of these designs.

Sherrott et al. [5] also proposed a similar device using patch antennas as resonators on top of a graphene layer, they achieved a phase shift of 230° at $\lambda = 8.5\mu m$ but due to its sharpness, it was not practical for continuous phase modulation purposes. A softer change with regard to the applied bias voltage was achieved at $\lambda = 8.7\mu m$ but the phase range was only 200°. This illustrates very well the non-linearity problem for resonant antennas, the

maximum phase shift is obtained near the resonant frequency of the oscillator, where it is most sensitive to the input variable.

2.3.3 Theoretical array investigation

Several tunable nanoresonators arrays have been proposed and investigated, in this subsection we present 4 interesting papers, all using GST as modulation material.

Cao et al. in 2015 used a MIM structure nano-resonator to achieve sub-wavelength phase control, the dielectric element was GST, its partial crystallisation states were used to obtain beam steering in both transmission and reflection modes. The thermal model predicted that different exposition times to the heat source would result in varying crystalline GST thickness which would modifies the resonator response. Beam steering over a 22° span in reflection and 11° in transmission was achieved in simulations.

Galaretta et al. also used GST to create a family of nano-resonators based on the same silicon-GST square geometry on top of an SiO_2-Au backplane shown in figure 2.6h [29]. By tuning the dimensions of the Si-GST resonator, one can tune the phase of the reflected field when the GST is its amorphous state but with little effect when it is in its crystalline state. By carefully arranging these resonators as building blocks, one can create a broadband switchable metasurface that showcases user-defined functionalities when GST is in its amorphous state and acts as a simple reflector otherwise. No intermediate control is possible and the functionality of the surface is fixed at fabrication since the size of the resonator cannot be changed post-manufacturing. Furthermore, the individual building blocks of this metasurface cannot be switched individually (due to their sub-wavelength size, it would require excessive efforts) and the metasurface is not intended for such use. Beam focusing and beam steering are proposed as potential applications and could be achieved since a 2π phase shift range was achieved. Again, in the case of beam steering, the authors only mentioned a periodic pattern (an exact 2π phase shift was achieved over a length $\alpha.p$, with $\alpha \in \mathbb{N}$, p being the array period) even though the design flexibility allowed by this geometry would allow aperiodic patterns ($\alpha \in \mathbb{R}^+$) to be considered.

Chu et al. in 2016 used an ingenious idea to potentially achieve three angles of anomalous reflection instead of two as was previously achieved [69]. The resonant metasurface they developed used two types of switchable antenna that achieve different phase shifts, antenna A can achieve 120° (OFF) or 0°(ON) while antenna B can be switched between 240°(OFF) and 360°=0° (ON). By using a supercell [AAAABBBBAABB], the length over which a 360° phase shift is completed can be varied from ∞ (no phase shift) 4800 nm (12 cells, 6 pairs) or 2400 nm (6 cells / 3 pairs) leading to angles of anomalous reflection of respectively 0, 20° and 40° using the following patterns :

- 0° : $A_{ON}A_{ON}A_{ON}A_{ON}B_{ON}B_{ON}B_{ON}B_{ON}A_{ON}A_{ON}B_{ON}B_{ON}...$
- 20° : $A_{OFF}A_{OFF}A_{OFF}A_{OFF}B_{OFF}B_{OFF}B_{OFF}B_{OFF}A_{ON}A_{ON}B_{ON}B_{ON}...$
- 40° : $A_{ON}A_{ON}A_{OFF}A_{OFF}B_{OFF}B_{OFF}B_{ON}B_{ON}A_{OFF}A_{OFF}B_{OFF}B_{OFF}...$

A reflectivity of 26% was achieved at 20° and 17% at 40° in this theoretical investigation. The main problem however for a real- life implementation is the switching of GST elements that can prove very hard at the individual antenna level using electric pulses that has not been achieved at that size yet. Again, we see that this study only uses periodic arrangements, this drastically limits the number of possible anomalous reflection angles.

In 2018, Forouzmand et al. [2] investigated the response of GSST nanobars and used two resonances (electric and magnetic dipole resonance) to achieve an unprecedented phase coverage of 270°. The geometry is as simple as a MgF_2-Au backplane on top of which a GSST nanobar of carefully chosen dimensions is placed at a given period. GSST allows for relatively low losses compared to GST and offers a large index modulation (n $\sim$ 3.3 to 5.1), allowing for better device performance than GST or VO_2 based metasurfaces. The reflectivity of a single antenna fluctuates between 0.6 and 0.8 over a phase control range of 270°, allowing the array-level reflectance to reach values above 0.45. The difficulty arising from the switching of GSST is taken into account is mentioned in the study and various effects are investigated, like the beam width of the laser used to trigger GSST transition that could be well above the metasurface period (up to 3*p in the article). Unfortunately, this design remained a theoretical investigation and no experiment was reported using the ideas developed in this article, the manufacturing and experimental challenges it proposed were probably too high.

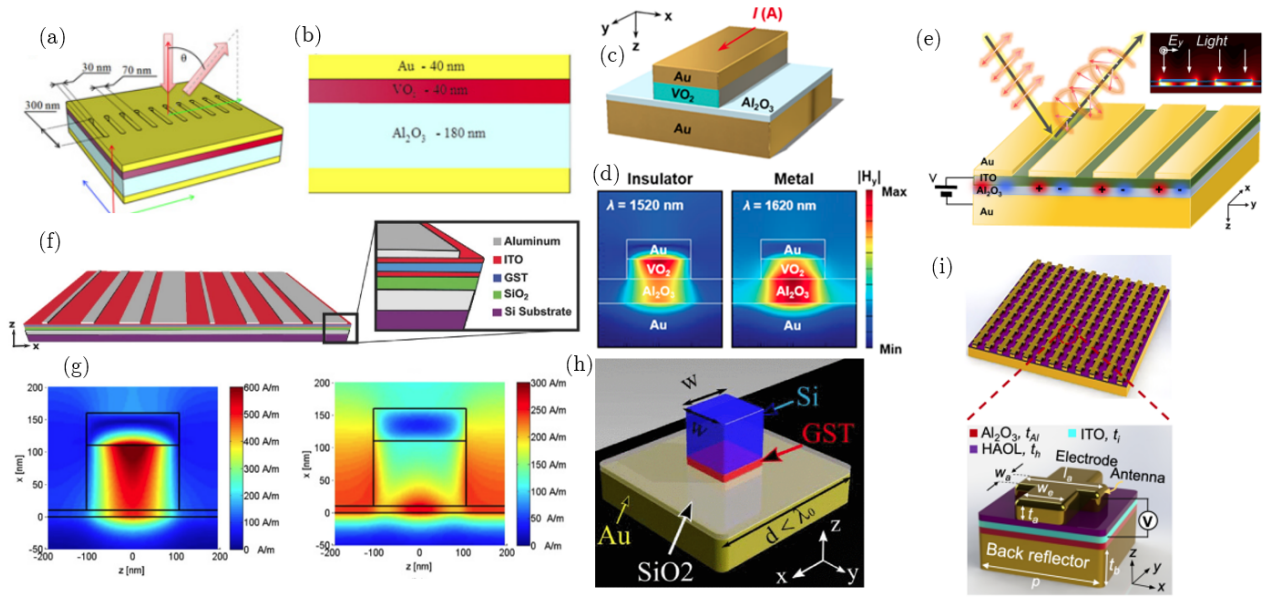

Figure 2.6: a) Design proposal with 10 nano-slits b) MIM structure for Kaplan et al. c) [1] antenna with MIM wire geometry proposal d) [1] Magnetic field resonance in the structure at 1520 and 1620 nm e) [3] Array geometry using ITO at $\lambda = 5.94\ \mu m$ f)[28] Switchable device proposal using GST using a geometric gradient g) [57] Magnetic field resonance in the MIM structure with cold (left) VO_2 compared to the structure out of resonance (hot VO_2, right) h) [29] design proposal using GST in a 3D geometry i) [23] 3D design proposal using ITO as tunable element in a MIM structure.

2.3.4 Experimental array investigations

In this section, we will review several tunable resonant metasurfaces that have been experimentally investigated, these are the most important results as they have been proven feasible. As some theoretical investigations may face unexpected experimental challenges, especially around the tuning mechanisms for GST, these articles report technologies that have been proven to work and represent the current boundary of the experimental domain.

As mentioned earlier, the mechanisms used to tune the GST crystallisation are complex and require heavy experimental setups. The main problem is to reach extreme heat fluxes to raise the GST elements temperature locally above its melting point but fast enough so that the element cools down by conduction with the surrounding matter (that has to remain cold). In 2015, Chen et al. achieved this using a femtosecond laser focused on a metasurface operating at 1550 nm, a maximum phase shift of 0.56π was achieved which allowed for beam steering and focusing to a limited extent [25]. The structure did not display excellent performance and it is especially true if we compare that to the efforts put to focus down the

extreme heat flux at the antenna scale using a piezoelectric stage. The real performance was not in the array functionality but rather in the fact that a functioning nanostructure using GST was built and tested, intermediate crystallisation states were reached which paves the way for more advanced future work. However it serves as a reminder that dynamic control of the phase of GST at a sub-micro level is a major challenge. Given the experimental setup currently required to work with this material, it is expected that commercial applications are a long way from now.

A more realistic way to use GST was proposed by Galaretta et al. [28] in 2018 where the entire device can be switched, GST being deposited as a single layer continuous film. This device shown in figure 2.6f has only one degree of freedom and performs beam steering at a fixed angle (33.6°) with a predicted efficiency of 32% and measured at 22%. The main advantage of this structure compared to Chen's device is that there is no need to focus and position the femtosecond laser beam down to a nanometric precision as the entire device can be illuminated simultaneously. However, its functionality is intrinsically limited to a single degree of freedom, allowing specific applications and proposing a novel metasurface but still being far from LIDAR applications.

ITO seems to be a very promising material for tunable resonant metasurfaces that has already been investigated with simulations before [3]. Huang et al. in 2016 [70] experimentally tested a tunable device using a rough form of binary control (compared to what we propose in this thesis) by only using periodic arrangements. The antennas were not individually controlled but a specific arrangement was hard-wired so the structure was technically only switchable, individual control was technically not demonstrated but this is only due to experimental limitations. A phase shift of up to 225° was achieved with an amplitude modulation of only 30% and dynamic switching frequencies of up to 10MHz were reached. As only periodic configurations were tested, the number of anomalous reflection angles was intrinsically limited to (the device had 34 wire antennas, 3 angles were simulated, 5 could be reached at most) and the structure suffered from the symmetric beam issue as it worked under normal incidence (see chapter 3, binary control section). However, a metasurface with individual antenna tuning capability was proposed and beam steering was demonstrated at high rates controlled with a simple voltage. If such a structure was controlled using an efficient control algorithm like the proposition in chapter 3, it could achieve electrically controlled continuous

beam steering over a wide angular range.

A different structure (shown in figure 2.6i), yet again using ITO as the tunable element was proposed by Shirmanesh et al. in 2017 and demonstrated beam steering at several angles thanks to individually controlled antennas. The device was comprised of 96 antennas each wired to an external connector and controlled digitally. A phase shift of up to 270° was achieved which enables a rather high antenna directivity and avoids a symmetric $-\theta$ lobe in the far-field. The array suffered from the same non-linearity in the phase shift and phase-amplitude correlation issues as all resonant antennas that have been reported in the literature with an reflectance comprised between 19% and 7%. The fact that a 2π phase shift was not achieved created a small lobe at $\theta = 0°$ at all steering angles. Again, the control algorithm was far from ideal as only periodic arrangements were tested, allowing a small number of possible anomalous reflection angles. This device, provided that it is controlled by an efficient algorithm, which would not require much work, could achieve continuous beam steering easily and seems very promising.

Regarding Vanadium dioxide, Hashemi et al. created a tunable resonant phased array operating at 100GHz ($\lambda = 3$ mm) that achieved a phase shift of 57° and allowed for continuous 2D beam steering at ± 22° [6]. The device only comprised 4*4 elements and is better described by the generalised law of refraction than phased arrays first principles as the device did not span over a phase range larger than 2π. Working in a similar wavelength range, a single reflectarray cell capable of 181° phase shift while maintaining a maximum loss of 0.44 dB at 35 GHz was later developed [71]. Despite noticeable differences with the scope of this thesis, Hashemi et al. demonstrated continuous beam steering using VO_2 was possible and the tuning of this material was rather simple compared to other phase change materials.

The most advanced experimental paper to date using VO_2 and that represents the state of the art on the objective of this thesis is Dr Yongwhi's thesis [7]. As shown in figure 2.6c, their MIM structure also uses Joule heating to trigger an IMT in the VO_2 element and displace the resonance from the VO_2 to the Al_2O_3 layer as shown in figure 2.6d. This resonance shift is accompanied by a resonance peak redshift (1520 to 1620 nm) and a phase shift as large as 250° but with a very high sensitivity to the VO_2 composition and a large decrease

in amplitude (near 0 at resonance). Dynamic modulation was demonstrated experimentally with an asymmetric transition(ON and OFF switching times of approximately 10 and 100 ms). The thesis conclusion describes a phased array simulation that demonstrates limited beam steering capabilities, only periodic arrangements were considered and the structure was not thermally realistic as we show later in section 5.3. This work however paves the way for the research in this thesis in which we employ a similar structure but adjust the thermal design and apply binary control.

Chapter 3

Theory and models

As we saw in chapter 2, resonant antennas suffer from three main flaws :

- Non 2π phase shift range : an incomplete phase range limits the implementation of a phased array [31].
- Non linear relation between the input signal and the phase shift, making control more challenging. sometimes this also translates in extreme sensitivity and therefore potentially to greater errors.
- Phase-Amplitude correlation : the amplitude varies along with the phase shift, meaning all antennas do not emit at the same power. This imperfect implementation creates side lobes as the contribution of antennas with different amplitudes cannot fully interfere destructively in the far-field.

In order to solve these problems, we introduce a novel control method for beam steering : binary control. The output phase of each antenna is controlled by a single bit of information : the antenna is either ON or OFF. This extreme discretisation enables us to design resonant nano-antennas that ideally implement binary control in the optical/NIR range. In the first section of this chapter, we study binary control theoretically and predict the properties of phased arrays using this control scheme from first principles. Although 1-bit phase control has already been used [72, 73] for reprogrammable hologram applications, binary control for beam steering is a novel contribution that has not been addressed in the literature before. Most derivations presented in this chapter are not drawn from an external source but are original results. One will note that binary controlled phased arrays have already been proposed [74] in a 4*4 array but again only for a very limited number of angles as the theory we develop in this chapter was not implemented.

As the following chapters will use FDTD simulations to emulate resonant nanostructures, a section on the background FDTD theory is necessary. We will also present the setup we used in the simulations presented in later chapters and several checks showing the robustness of the FDTD simulations.

3.1 Binary control theory

3.1.1 Beam steering theory for binary control

Beam steering theory for binary control follows directly continuous control to which we add a discretisation step, in this section we show how to implement binary control for beam steering and then derive the properties of such phased arrays.
We recall the generalised law of refraction from equation 2.1 that will be used for beam steering using phased arrays. Note the sign convention for the angles (increasing clockwise) is as shown in figure 2.1.

$$sin(\theta_r) = \frac{\Delta\Phi_s}{\Delta x}\frac{\lambda}{2\pi} - sin(\theta_i) \tag{3.1}$$

We can integrate this equation to get the ideal phase profile required for beam steering :

$$\Phi_s(x) = \Phi_0 + \frac{2\pi.x}{\lambda}.(sin(\theta_i) + sin(\theta_r)) \tag{3.2}$$

The direct implementation of equation 3.2 requires 2π phase shifting capability. The binary control algorithm to convert this "ideal phase profile" to a "binary profile" is simple: we minimize the phase discrepancy between the binary phase shift profile and the ideal one. For $\Phi(x) \in [-\pi/2, \pi/2[$, we use a phase shift of 0 ("OFF" state) and symmetrically, for $\Phi(x) \in [\pi/2, 3\pi/2[$, we have a π phase shift, the antenna is in "ON" state. This selection algorithm is simple and maximizes by construction the power at angle θ_r but has a major drawback that can be seen in figure 3.1 : it simultaneously maximizes the power sent at $-\theta_r$ (for normal incidence, θ_i=0). We will see in the next section how this problem can be solved by breaking this $\theta_r/-\theta_r$ symmetry .

3.1.2 Angle of incidence

We can break the symmetry in the far-field pattern by introducing a non-zero angle of incidence : it pushes the $-\theta_r$ peak out of a region of interest or suppresses it ($|sin(\theta_r)| > 1$). This region is defined by a single angle θ_{max} so as to keep it symmetric around the array

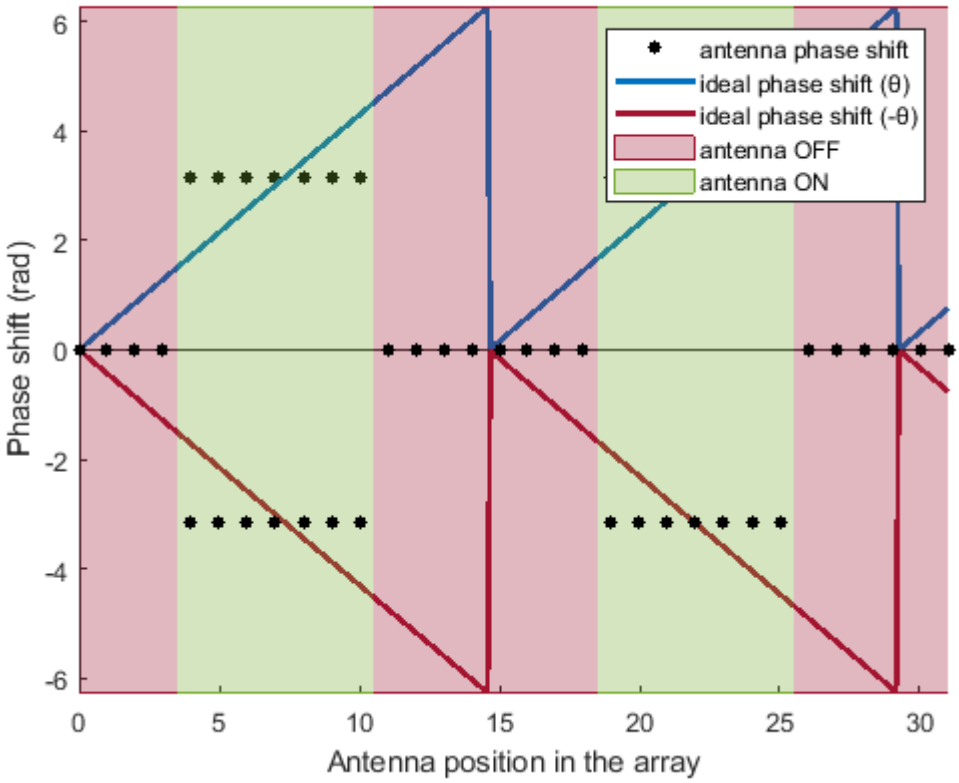

Figure 3.1: Binary control issue visualisation. Pushing discretisation to the extreme (two possible states) removes the distinction between a phase gradient and its opposite : they correspond to the same array state as $-\pi = \pi mod(2\pi)$.

normal vector as $[-\theta_{max}; \theta_{max}]$. In the following derivation, we assume a negative angle of incidence (in the second quadrant) as a sign convention to maintain $\theta_{max} > 0$.

From equation 2.1, we define α the steering parameter that can be tuned between $\pm\lambda/2p$ where p is the system's periodicity. This maximum value is achieved when we are in a "grating" configuration : the switching pattern is ON-OFF-ON-OFF-ON...

$$\alpha = \frac{\Delta\Phi\lambda}{2\pi\Delta x} = sin(\theta_i) - sin(\theta) \tag{3.3}$$

In the case of binary control, the array state is going to be in the same state with $\alpha = \pm\alpha_0$ as can be seen in Figure 3.1. We therefore restrict ourselves to using positive values of α. We note that with $\alpha = 0$, the metasurface is a simple mirror so get $\theta = -\theta_i$. This corresponds to one of our boundaries and we get our first result :

$$\theta_{max} = -\theta_i \tag{3.4}$$

Similarly, we want to reach θ_{max} with a maximum phase gradient, which corresponds to $\alpha = \lambda/2p$. We re-arrange equation 3.3 and obtain :

$$sin(\theta_{max}) = \frac{\lambda}{2p} + sin(\theta_i) \tag{3.5}$$

The upper bound on α is easily justified as we remark that any higher value would also correspond to another angle with $\alpha' = \alpha_0 \pm \lambda/2p$, the secondary beam simply re-appears at the other end of the field of view. Injecting equation 3.4 in equation 3.5 , we find the following :

$$\theta_{max} = -\theta_i = arcsin(\frac{\lambda}{4p}) \tag{3.6}$$

We show in equation 3.6 that decreasing periodicity to values lower than than $\lambda/4$ does not increase the angular range of the array, however it may decrease the discretisation effects near the boundary for extreme angles. Figure 3.2 shows θ_{max} versus the array period with the design proposal we will elaborate on in the next chapter. As we will avoid grazing incidence in practice, we can choose a spatial period longer than $\lambda/4$. For example, if we choose $\theta_{max} = 60°$, we have $p = \lambda/4.asin(\pi/3) = 0.289.\lambda$, which is $p = 447\ nm$ at $\lambda = 1550\ nm$. Similarly, by choosing a periodicity $p = \lambda/3$, we have $\theta_i = asin(3/4) = 48.6°$.

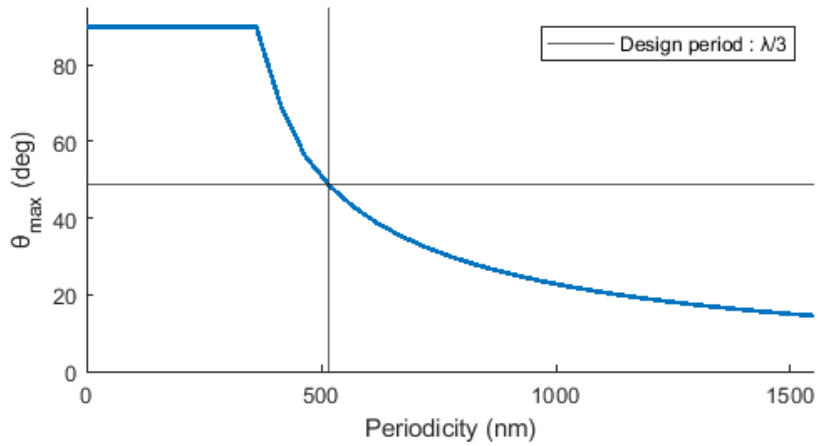

Figure 3.2: θ_{max} calculated from equation 3.6 for periodicity values ranging up to λ for $\lambda = 1550\ nm$.

The periodicity of the array is therefore a crucial factor in the design as it defines the angular spacing between adjacent lobes and therefore the optimum angle of incidence to obtain a large functional region of interest (with a unique lobe).

3.1.3 Peak amplitude with binary control

The far-field profile obtained with binary control cannot easily be described generally, phased arrays are complex systems for which direct calculations are usually the only way to derive their behavior. We can however mention some general considerations regarding binary-controlled phased arrays, noticeably their peak-power.
The far-field amplitude profile produced by a phased array in the Fraunhofer conditions is calculated from equation 3.7.

$$A(\theta)^{1/2} = E(\theta) = \sum_{m=1}^{N} E_m(\theta) e^{j.(\omega.t + \Phi_m + k_0 x_m \sin(\theta_i) + k_0 x \sin(\theta))} \tag{3.7}$$

Where $A(\theta)$ is the energy distribution with respect to angle θ, θ_i is the incident angle, Φ_m and x_m are the tunable phase shift applied at reflection by the antenna and the position of the mth antenna in the array. Regarding $E_m(\theta)$, we can apply the usual cosine distribution : $E_m(\theta) = E_m \cos(\theta)$. By integrating equation 2.1, we get the phase profile along the array length in equation 3.8:

$$\Phi(x)_{steering} = \Phi_m + \frac{2\pi(\sin(\theta_r) + \sin(\theta_i))}{\lambda} x \tag{3.8}$$

In this ideal case, we calculate the far-field amplitude at $\theta = \theta_r$ with equation 3.9.

$$A(\theta_r)^{1/2} = E(\theta_r) = \sum_{m=1}^{N} E_m(\theta_r) e^{j\omega t} = E_m(\theta_r) \sum_{m=1}^{N} e^{j\omega t} = N.E_m(\theta_r).e^{j\omega t} \tag{3.9}$$

However, in binary control, there is a discrepancy between the ideal phase profile and the actual reflected phase, $\Delta\Phi_m$ for each antenna given by equation 3.10.

$$\Delta\Phi_m = \Phi_{m-ideal} - \Phi_{m-real} = k_0 x_m \sin(\theta_i) + k_0 x \sin(\theta)) - \Phi_m \tag{3.10}$$

The antenna state selection algorithm minimises $\Delta\Phi_m$ but given the coarse 1-bit discretisation of this control mechanism, we are left with a phase error randomly distributed in $[-\pi/2; \pi/2]$ in the general case (when the reflection angle does not correspond to an exact periodic arrangement). The normalised peak power in this case is calculated in 3.11.

$$\sqrt{A_d(\theta_r)} = E_d(\theta_r) = \sum_{m=1}^{N} E_m(\theta_0) e^{j(\omega t + \Delta\Phi_m)} \simeq N.E_m(\theta_r) e^{j\omega t} \frac{1}{\pi} \int_{-\pi/2}^{\pi/2} e^{j\Delta\Phi} d\Delta\Phi = \frac{2.N.E_m(\theta_r) e^{j\omega t}}{\pi} \tag{3.11}$$

We can compare it to the ideal case in equation 3.12 and see that there is a power loss of about 60% due to destructive interference in the main beam compared to the ideal case. This destructive interference is solely due to the coarse discretisation in binary control and not to any inaccuracy in its implementation. This control mode is therefore not ideal in applications where high power efficiency is needed.

$$\frac{A_d(\theta_r)}{A(\theta_r)} = \frac{4.N.E_m(\theta_r)^2}{\pi^2.N.E_m(\theta_r)^2} = \frac{4}{\pi^2} \simeq 0.4053 \tag{3.12}$$

Note that this derivation is applicable to the 1D case as well as the 2D case as it does not assume anything about the arrangement of the antennas. In the 2D case, the summation from m=1 to N should be understood as N being the total number of antennas.

3.1.4 Inaccurate implementation of binary control

The two main parameters that describe an antenna between its ON and OFF states are the phase difference (ideally π rad) and the amplitude ratio (ideally 1). In order to better understand binary control and how its implementation results in terms of beam steering performance, we test the array behaviour when the phase difference and amplitude ratio are not set to their respective ideal values. We conduct a large number of direct calculations, this is much faster and more repeatable than FDTD simulations, thus enabling us to get fine sweeps and a good idea of how an imperfect phased array implementation impacts the device's performance. We will later show FDTD simulation results and compare them to the direct calculations, the good match between these two techniques allows us to use first principle calculations safely to predict the array behaviour.

The phase is defined relatively from one state to another (we can arbitrarily set the phase of the OFF state at 0) and the absolute reflectance of either state is also irrelevant as it would simply change the array's far-field by a multiplicative constant. We apply equation 3.7 with a fixed angle of incidence $\theta_i = 45°$ and anomalous reflection $\theta_r = 20°$ (arbitrary value) for an array of N=32 antennas. We record the following performance indicators :

- Figure 3.3 : Side Lobe Suppression Ratio (SLSR) : the ratio of amplitude between the main peak and the second next largest peak in amplitude (a side lobe).

- Figure 3.4 : The energy In/Out ratio : we integrate the far-field E^2 field in $[-45°, 45°]$ and in $[\theta_r - FWHM, \theta_r + FWHM]$. The first result, E_1 corresponds to the energy reflected by the array and the second, E_2 to the energy contained in the main beam (the integration width of 2.FWHM allows to take the whole peak into account). The ratio $E_2/(E_1 - E_2)$ is recorded.

- Figure 3.5 : The peak amplitude (normalised), we simply record the peak amplitude, we normalise by dividing the E-field amplitude by the sum of the individual antenna's amplitude $E_m(\theta)$. This normalisation factor corresponds to a scenario where all the antennas perfectly interfere constructively at θ_r.

The FWHM does not differ from the ideal case and is stated in equation 3.13, the 0.886 term is due to the $sinc^2$ amplitude distribution [75]. We use this FWHM value to calculate the In/Out energy ratio.

$$\Delta FWHM = \frac{0.886.\lambda}{N.p.cos(\theta)} \tag{3.13}$$

It is also possible to derive a formula for the peak amplitude using the same ideas as in equation 3.11. This time however, we introduce an asymmetry between the two states, the antenna in its ON state applies a phase shift of $\pi - 2\delta$ (the OFF state is still the phase reference with 0 phase shift).

- The antenna is OFF : $\Phi_m = 0$ if $\Phi(x) \in [-\pi/2 - \delta, \pi/2 - \delta[$
- The antenna is ON : $\Phi_m = \pi - 2\delta$ if $\Phi(x) \in [\pi/2 - \delta, 3\pi/2 - \delta[$

We now assume that the phase error is randomly distributed in each interval but this distribution is not symmetric around Φ_m. We note that as both intervals cover the same angular span, half the antennas should be in the OFF state, half in the ON state. In the OFF state, the error is therefore randomly distributed in $[-\pi/2 + \delta, \pi/2 + \delta[$, in the ON state, the error is randomly distributed in $[-\pi/2 - \delta, \pi/2 - \delta[$. We therefore derive separately two equations, similar to eq 3.11 but where the integration bounds are respectively shifted by δ and $-\delta$.

$$E_d(\theta_r) = \sum_{m=1}^{N} E_m(\theta_0) e^{j(\omega t + \Delta\Phi_m)} = E_{d-OFF}(\theta_r) + E_{d-ON}(\theta_r) \tag{3.14}$$

For the OFF state we have :

$$E_{d-OFF}(\theta_r) \simeq \frac{N}{2} E_m(\theta_r) e^{j\omega t} \frac{1}{\pi} \int_{-\pi/2-\delta}^{\pi/2-\delta} e^{j\Delta\Phi} d\Delta\Phi = \frac{N.E_m(\theta_r) e^{j\omega t}.e^{j\delta}}{\pi} \tag{3.15}$$

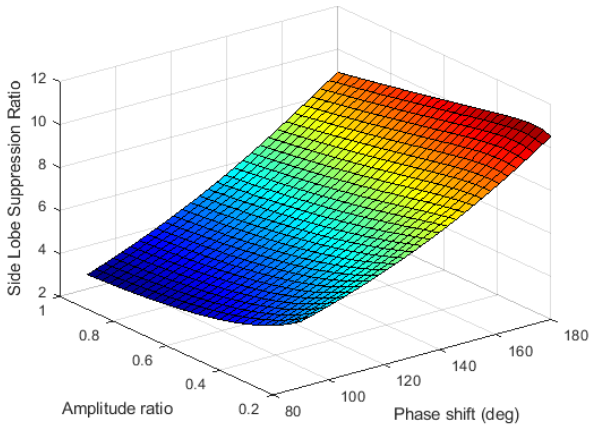

Figure 3.3: Side Lobe Suppression Ratio with inaccurate implementation of binary control.

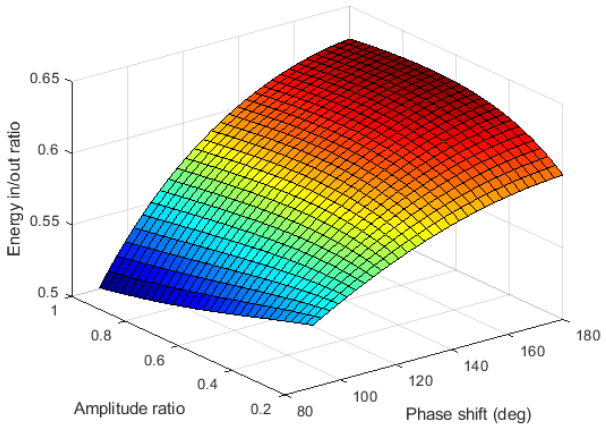

Figure 3.4: Energy In/Out ratio with inaccurate implementation of binary control.

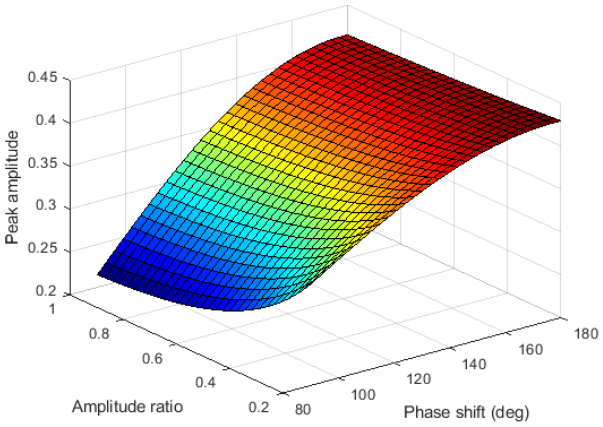

Figure 3.5: Peak amplitude with inaccurate implementation of binary control.

For the ON state we have :

$$E_{d-ON}(\theta_r) \simeq \frac{N}{2} E_m(\theta_r) e^{j\omega t} \frac{1}{\pi} \int_{-\pi/2-\delta}^{\pi/2-\delta} e^{j\Delta\Phi} d\Delta\Phi = \frac{N.E_m(\theta_r) e^{j\omega t}.e^{-j\delta}}{\pi} \tag{3.16}$$

We substitute equation 3.16 and 3.15 in equation 3.14 to find :

$$E_d(\theta_r) = \frac{N.E_m(\theta_r) e^{j\omega t}}{\pi}.(e^{j\delta} + e^{-j\delta}) = \frac{2.N.E_m(\theta_r) e^{j\omega t} cos(\delta)}{\pi} \tag{3.17}$$

And the energy ratio is calculated simply by multiplying by the conjugate (squaring in the case of real numbers) as in equation 3.12, this time taking into account a $cos(\delta)$ factor that

is caused by a non-π phase difference between the two operating states.

$$\frac{A_d(\theta_r)}{A(\theta_r)} = \frac{4.N.E_m(\theta_r)^2.cos(\delta)^2}{\pi^2.N.E_m(\theta_r)^2} = \frac{4.cos(\delta)^2}{\pi^2} \tag{3.18}$$

This derivation is useful for two main reasons :

- It allows us to quantify the impact of a non-π inaccuracy on the main lobe amplitude. Given the characteristics of the cos^2 function, a small difference is affordable but the reduction in peak amplitude goes up very rapidly with the phase error.

- It provides insight into the behavior of phased arrays, we realise that in order to obtain a high peak amplitude, we need to minimise the phase difference between the ideal phase profile and the actual phase. This principle can be seen in the definition of binary control but also works with its inaccurate implementation or even other discretisation schemes (3, 4 or more steps). We also note that side lobes are simply avoided in general if there is no specific reason that all the antennas should interfere constructively.

3.1.5 Side lobes with binary control

3.1.6 2D beam steering

The equations for 2D beam steering can be drawn easily from the 1D case, in this section we derive them and show how binary control can be applied to 2D beam steering.
In order to simplify the analysis, we do not directly use spherical coordinates but instead use θ and γ the angles between the chosen direction of anomalous reflection and the x-axis and the y-axis, respectively, as shown in Figure 3.6. It is possible to go from a spherical coordinate system [pol, az] to this θ,γ system using the following variable change :

$$sin(\theta) = sin(pol).cos(az) \quad sin(\gamma) = sin(pol).sin(az) \tag{3.19}$$

Using this variable choice, the Fraunhofer conditions allow us to completely separate both variables and consider the phase shift associated with θ and γ separately. For the m^{th} antenna located at a position $[x_m, y_m]$, we have two phase shifts associated with θ and γ defined as :

$$\Phi_x = x_m.k_0.(sin(\theta_i) + sin(\theta_r)) \tag{3.20}$$

$$\Phi_y = y_m.k_0.(sin(\gamma_i) + sin(\gamma_r) \tag{3.21}$$

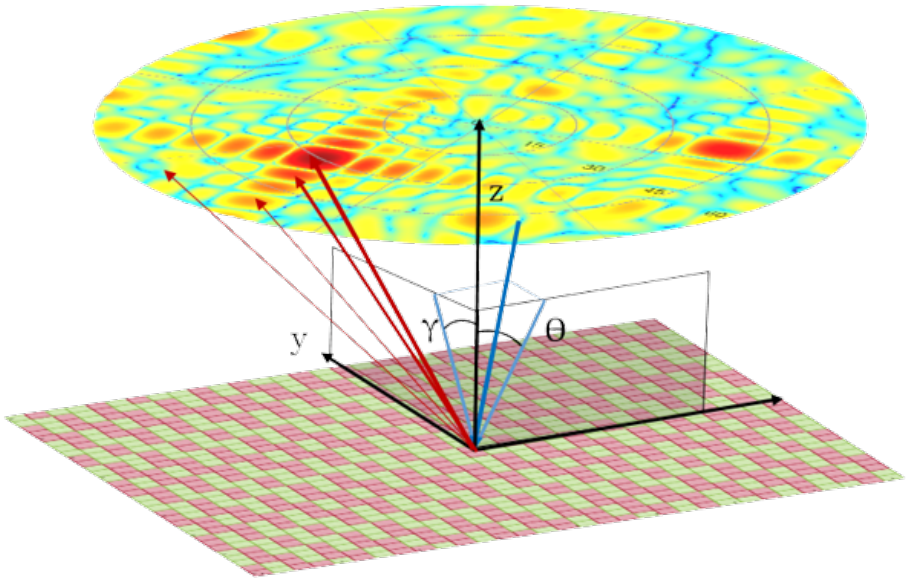

Figure 3.6: 2D Beam steering schematic - choice of angle system. The incident beam is in blue, the reflected field from the array in red (line width proportional to the intensity of the field in the arrow direction) and the coordinate system in black. We show the definition of γ and θ vis-à-vis with the incident beam.

Two antennas located at the same x (y) position in the array will have the same phase constraint Φ_x (Φ_y). For a rectangular array, this makes the calculations slightly easier.
The phase selection algorithm is the same as in 1D binary control but we have to consider the sum of the two constraints. If $\Phi = \Phi_x + \Phi_y$ $[2\pi]$ is in $[-\pi/2, \pi/2[$, then the antenna is left in its OFF state, similarly, if Φ is in $[\pi/2, 3\pi/2[$ we turn the antenna to its ON state.

The array state derived from this algorithm is more visual than its 1D counterpart as can be seen in Figure 3.7, the resulting far-field is very satisfactory demonstrating beam-steering in 2 dimensions as shown in Figure 3.8. These plots were obtained for an array with x-periodicity and y-periodicity of $\lambda/3$, angle of incidence θ_i and γ_i of 45° and 45° and desired angle of anomalous reflection θ_r and γ_r of $-10°$ and 30°.

Direct simulations are significantly more time consuming for 2D beam steering as we have to sum $N_\theta * N_\gamma$ antennas over a far-field discretised in N^2 points. Which means the complexity of the algorithm is increase to the power two, it is still a reasonable computational time even for commercial desktops, provided that the far-field is not discretised too finely.

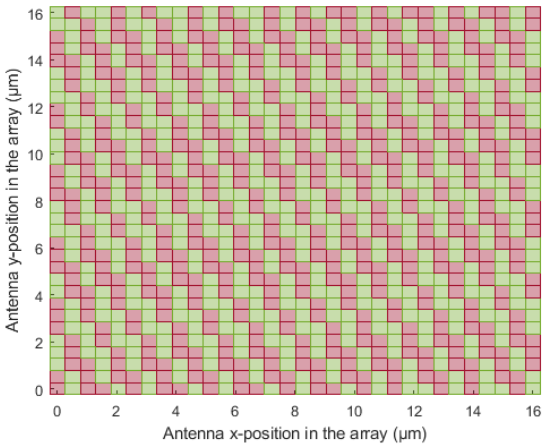

Figure 3.7: Array state in 2D.

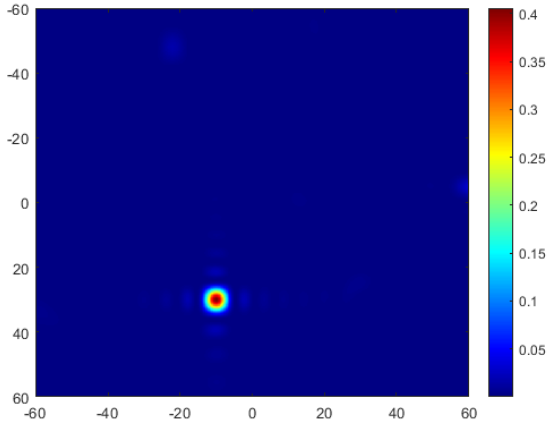

Figure 3.8: Far-field in 2D.

The difference with the ideal case (with perfect continuous 2π phase shift) is shown in Figure 3.9, we use a logarithmic scale to better visualise small amplitudes.

3.1.7 Binary control resolution

The discrete nature of binary control implies that only a finite number of angles can be reached in the far-field. We will see in this section how many of these points can be resolved and quantitatively justify the claim of "continuous beam steering".
The number of possible configuration for an array comprised of N antennas is 2^N but the vast majority of these arrangements do not correspond to beam steering and they would produce a random far-field interference pattern. The number of arrangements that correspond to a beam steering configuration scales with N^2, we calculated this number by brute-force simulations for low N ($N \inf 256$) to confirm that claim but finding an analytical formula for the exact number of arrangements versus the number of antenna remains an open mathematics problem.
In order to calculate the number of "legal configurations" that correspond to a constant phase gradient (with discretisation errors of course), we use the following brute-force algorithm :

- Choose a very small step-size, typically $0.01°$ and boundaries that correspond to the region of interest. Initialise a configuration list to null.

- Conduct a sweep of all angles in this region separated by the step-size, for each angle, calculate the array arrangement.

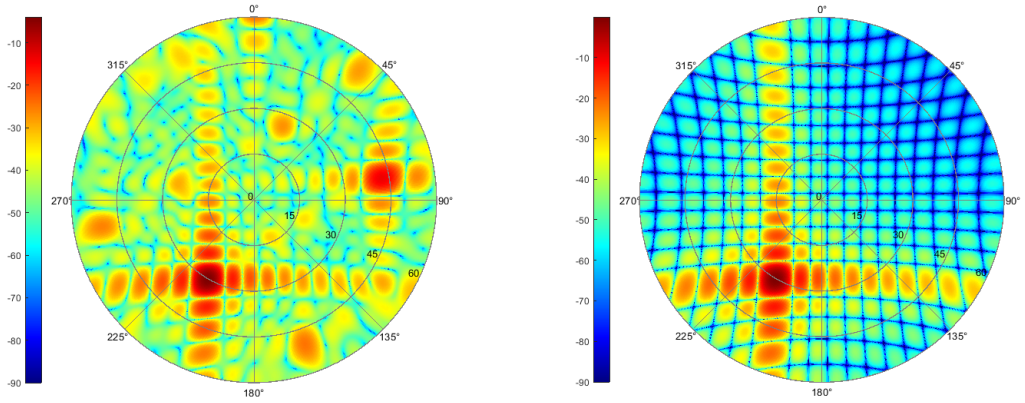

Figure 3.9: 2D Binary control compared to ideal control - far-field amplitude in logarithmic scale, azimuthal angle 210°, polar angle 30°.

- Compare the array configuration with latest addition in the configuration list : if the arrangement is not new, discard it and go to the next iteration. If it is, add it to a memory list for future comparison.
- If in doubt, double check if a smaller step-size leads to an increased number of beam steering configurations found

This algorithm is not optimised for efficiency but we can calculate the number of beam steering configurations in a few seconds/minutes for up to 256 antennas which is fine in practice. In our case, we use $\theta_i = 45°$ and therefore the region of interest is $[-\theta_i, \theta_i]$, we use $p = \lambda/3$. Table 3.1 and figure 3.10 summarise the results of this algorithm. An excellent fit with a 2nd degree polynomial $N_{config} = 0.38 * N^2$ is found, the derivation of the exact value of the polynomial constant is out of the scope of this paper.

One will note that with the FWHM being inversely proportional to the number of antennas, the number of resolvable points is directly proportional to N. The number of resolvable points scales slower (in N) than the number of "legal" array configurations (in N^2). Therefore, we will quickly have more beam-steering configurations than resolvable points, for reasonable

$N_{antenna}$	N_{config}
2	2
4	6
8	24
16	89
32	378
64	1536
128	6207
256	24897

Table 3.1: Number of array configurations corresponding to beam steering versus number of antennas.

values of N like $N = 32$, we already have 378 individual beam-steering arrangements, while the number of resolvable points is around 20. Hence the mention of "continuous beam steering" : even if only a discrete number of points are obtainable, the jumps between one angle to the next is imperceptible compared to the beam width, even for rather low N values.

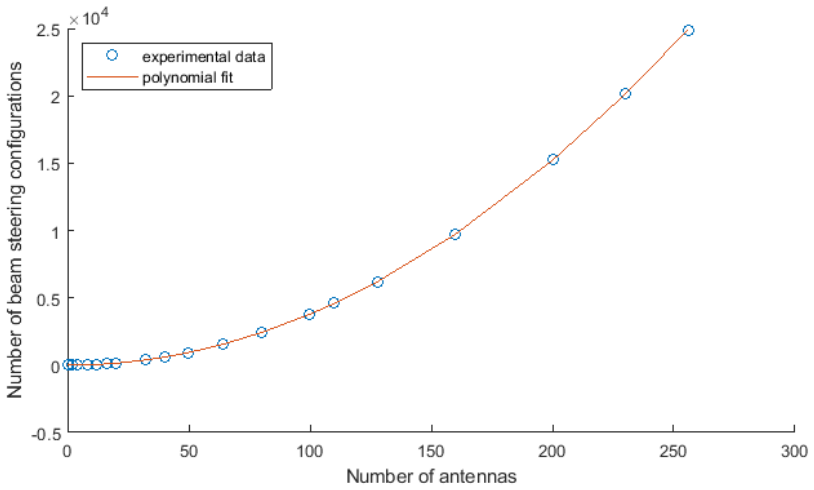

Figure 3.10: Number of beam-steering array arrangements versus number of antennas.

Even if this does not constitute a rigorous proof, we can justify intuitively why the number of beam steering configurations scales with N^2. The m^{th} antenna in the array will go through exactly m changes over a complete sweep of the region of interest as the phase shift for this antenna goes from 0 to $m\pi$. There is therefore a total of N(N+1)/2 switches over a full sweep, which is of the order of N^2, this exact value is not reached in practice as two antennas may be required to switch at the exact same angle (the switch being recorded at the same time, a single additional configuration will be counted). We consider the phase profile rounded to the nearest multiples of π, we have a consecutive list of multiples of π, some being listed multiple

times in a row. We call this vector the "pre-configuration vector", it will have its m^{th} bit flip (the m^{th} instance of an entry which is different from the previous one) in the position where $m\pi$ appears in the pre-configuration vector. So if m first appears in different positions in two pre-configuration vectors, they must correspond to different configuration vectors. Given the restrictions on the slope of the phase profile (no increase of more than π is allowed between two adjacent antennas), we prove not two widely different phase profiles can correspond to the same configuration vector.

We also present a slightly more rigorous proof that gives a lower bound on the number of configuration vectors with N. For simplicity in the following paragraphs, we divide the phase profile values by π so that we only deal with integers and not multiples of π. We thank James Murphy for this proof.

We choose $0 < k \leq N$ and restrict our view to phase profiles with slopes between $1/2(k-1)$ (or 1 if $k = 1$) and $1/2k$. These phase profiles have configuration vectors which are all 0 for the first $k-1$ entries, followed by a 1 in the k^{th}. Letting $m = 1$ in the argument above, we see that each configuration vector corresponding to one of these slopes is different from every configuration vector produced by a different choice of k. By varying the choice of slope within the range $[1/2(k-1)\ ;\ 1/2k]$, we can choose if 2 first appears in the pre-configuration vector in position $3k-2$, $3k-1$ or $3k$. Likewise for any m with $2m-1 < N/k$, we can choose if m first appears in the pre-configuration vector in position $mk-(m-1)$, $mk-(m-2)$,... or mk. This produces m distinct configuration vectors. Choosing m to be the floor of $N/2k+1/2$, we get approximately $N/2k$ distinct configuration vectors. Summing over all k in $[0 < k \leq N$, we get approximately $N.ln(N)/2$ distinct configuration vector counted by this method. The error from both approximations is linear so it can be disregarded. We hereby prove that the number of configuration vectors grows faster than N which is a key finding to ensure continuous beam steering.

3.2 FDTD simulations

3.2.1 FDTD method - theory

The Finite Difference Time Domain method, or FDTD, is a numerical approach to solve Maxwell equations in the time domain before converting the results back into the frequency domain. The 4 Maxwell equations are discretised in a grid (2 or 3D) and solved numerically one time step at a time until a steady state or a maximum time limit is reached.

A central feature in the FDTD method is the non-trivial grid that is used : the Yee grid separates the electric and magnetic field and evaluates them at different positions in space [76]. As can be seen in figure 3.11, the interpolation points for the E and H fields are distinct, they are also resolved separately in half steps : solving one field at time t_i then the other at time $t_{i+1/2}$ using the updated data from t_i.

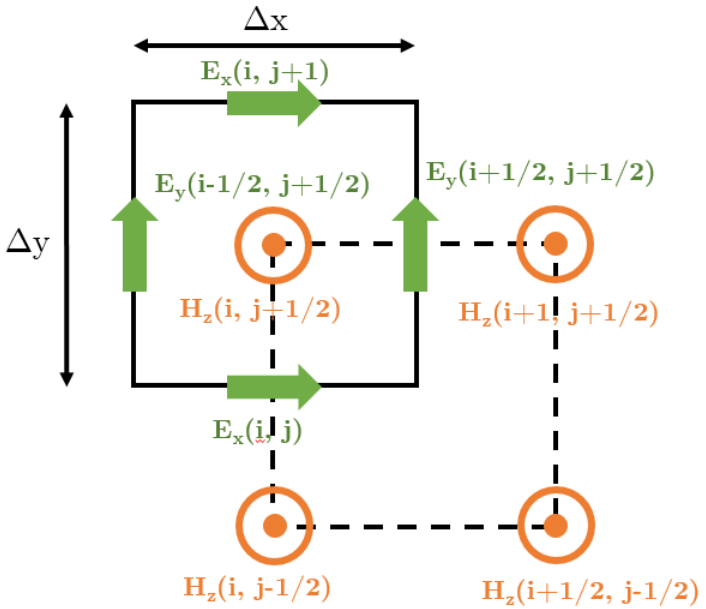

Figure 3.11: Schematic of the 2D Yee grid.

The sources used in our simulations use a time resolved pulse as shown in Figure 3.12, the FDTD solver then simulates the transient behavior of the structure illuminated by that specific source signal. The power monitors store the data measured at each point in time and can perform a Fourier transform, normalise the results by the input spectrum and output each field amplitude and phase at the end of the simulation in the frequency domain. The details of the numerical methods used to solve the Maxwell equations are not discussed in this thesis but the reader is referred to John Schneider's book for more details [77].

3.2.2 FDTD setup and assessment of its robustness

Two main setups were developed in Lumerical with a number of variations which we will describe in this subsection :

- Single antenna simulation
- Array simulation

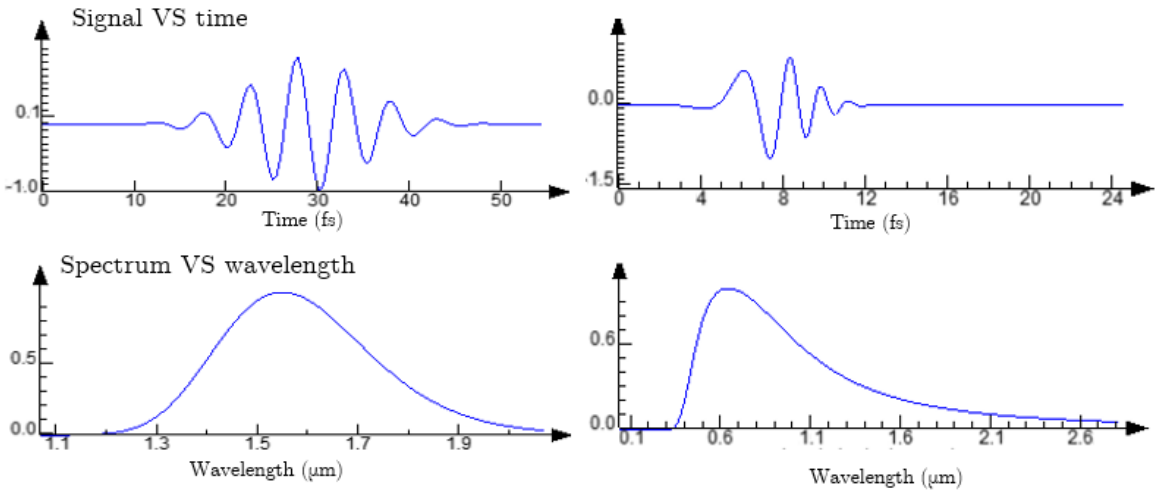

Figure 3.12: Narrowband and broadband pulse generated by the Lumerical FDTD solver for a simulation band of 1550 to 1550 nm and 400 to 1600 nm.

The single antenna simulation setup does not focus stricto-sensus on a single antenna but rather on an array of perfectly similar antennas using periodic boundary conditions. A schematic of this setup is shown in figure 3.13a, it can then be declined using two meshing options that gave satisfactory results but can be applied in different contexts.

A uniform mesh refinement is used for all the sweeps and manually "triggered" simulations, this method is simple, reproducible and a mesh convergence test can be done to verify its accuracy. However, this method suffers from the staircase effect : the material properties being interpolated at the node, if the boundary between two layers is continuously adjusted over the length of a mesh cell, the output will not vary until the boundary crosses the node. The smallest geometric step that a simulation can take into account is therefore as large as a mesh cell which can be problematic for gradient descent based approaches. We can however take advantage of the mesh generation methods by creating a "layered mesh" through the introduction of several mesh refinements. We begin by setting a target mesh size on the x and y-axis, they do not need to be similar. Each material layer has its own mesh refinement where the mesh size is adjusted so that an exact integer number of mesh cell exist within the material layer. We simply set the mesh size over a length L with a target mesh size l_m to $floor(L/l_m)+1$. The difference with the default mesh can be seen in figure 3.13b. The mesh refinements need to be refreshed along with the geometry at each simulations, this approach enables the use of gradient-descent based algorithms that use marginal changes in geometric features. The layered mesh results were checked against the uniform mesh simulation output

as can be seen in figure 3.13c, we verified that almost similar results were obtained, thus validating this approach. In both cases, we use the "conformal mesh variant 2" and a mesh size in the x and y axis of respectively 10 and 12 nm.

Lumerical prevents large mesh size gradients so this may be problematic to some extent if the layer thickness is too small : by forcing at least a full mesh cell to be found within a thin layer, the mesh size on adjacent layers is impacted. At the limit, with a 0-thickness, the mesh size is 0, thus creating a numerical error : this problem is solved by only creating a mesh refinement for a layer if it has a thickness greater than a threshold value.

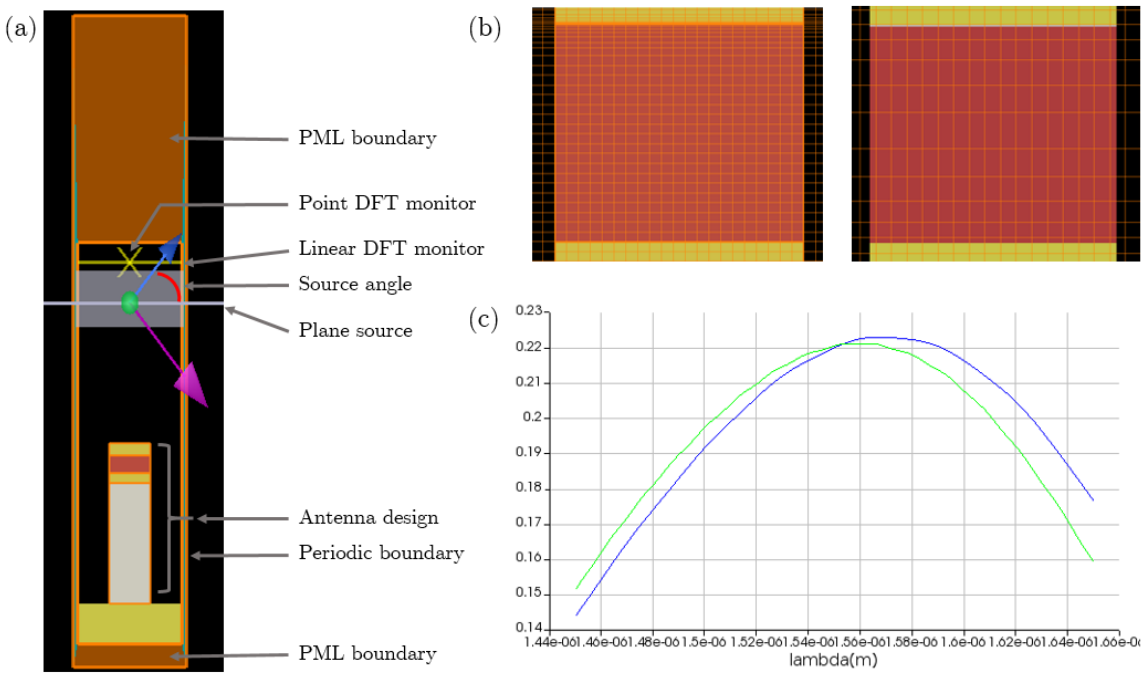

Figure 3.13: a - Structure schematic b - Mesh comparison between the layered mesh (left) and the default mesh (right), the high refinement on top of the VO_2 layer is due to the Ti layer of thickness 2 nm c - Sample antenna reflectance versus wavelength for the layered mesh (blue) and the default mesh (green).

The "PML" (Perfectly matched layer) mentioned in figure 3.13a is a fully absorbing layer that would correspond to free space where the waves propagate out of the simulation region. The PMLs are specifically engineered to not reflect the field [78], they can however bring numerical errors in the simulation if not used appropriately. In our simulations, we used 8 stretched coordinates PMLs with the default Lumerical parameters that provided good results and converging simulations. The "stretched coordinates" can be seen in 3.13a as the

y-min (bottom) PMLs extending from the gold backplane are spatially much closer than the y-top ones that extend from free space since the mesh size in free space is larger than in gold. The most prominent example is the use of a source extended through the PML, as this mesh type is anisotropic, and meant to absorb the field coming from a specific direction, substituting a wave inside it usually results in simulation divergence.
The "point DFT monitor" and "linear DFT monitor" record the field profile in the frequency domain [79], the point monitor is used to record the phase shift and the x-linear monitor the reflectance spectrum.
The x-boundary conditions are not strictly speaking periodic boundary conditions as this exact name corresponds to a different BC in Lumerical. Since periodic boundary conditions cannot handle properly a complex incident field at non-normal incidence where k_x of the plane wave is non-zero, "Bloch" BC are used. It is very similar to the periodic setup but uses double the memory and computation time as the recorded fields are complex numbers and not real.
It is worth noting that this setup is entirely generated by code which enables fast implementation of changes and the automation of the simulations. There are just a few variables necessary to describe the entire setup and reconfiguring it entirely only takes a few ms of computation time. This step was crucial in the research project as it saves a considerable amount of time, furthermore, the code can be re-used in other simulation setups like the array-simulations or other geometries that we will describe in later sections.

The array simulations were not simply a replication of N single antenna setups, some changes were brought to keep reasonable computational times and robust results. The simulation setup is similar to the single-antenna setup unless mentioned otherwise. We show in figure 3.14 a small array with N=4, the mesh is not layered to save on computation time and simulation complexity, we instead use a mesh refinement on each antenna. The mesh size in the refinement is 12 nm in the x-axis and 6 nm in the y-axis, both values are slightly modified by default to fit an integer number of mesh cells within the refinement. We can see in the insert that there is a perfect match between the x-mesh and the vertical antenna boundary, however the y-mesh does not perfectly fit the layers. The boundary conditions are different in the x-axis as the array is not meant to be repeated in this direction. We therefore use PML x-BC, we have to be careful with the proximity between the x-BC and the source edges

as it is better they don't overlap nor intersect. We also add an x-linear near-field monitor to verify that the phase profile corresponds to our expectations, a 2D monitor can be generated to capture the E and H fields but this adds a significant amount of computation time.

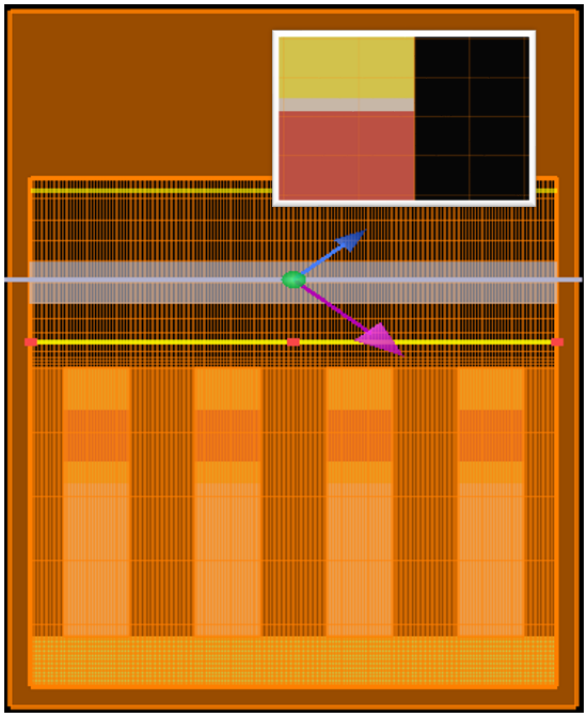

Figure 3.14: Array simulation setup with N=4, insert is a zoom on one of the antennas to show how the mesh fits with the boundaries of the structures.

The far-field projections are obtained from Lumerical built-in tool and either converted to .mat files or directly sent via a program-controlled command to MATLAB for post-processing.

Chapter 4

Inverse design

In this chapter, we introduce the reader to inverse design and show how optimisation algorithms can be used to find and fine-tune a nanophotonic device. After a brief overview of inverse design, we will see the main advantages and challenges associated to it. We will then describe the two algorithms we used in this project, show how they work and what task they operate. We will also discuss why these two algorithms were chosen out of a vast pool of optimisation algorithms.

4.1 Inverse design overview

Inverse design is a design technique that utilises an algorithm to systematically optimise a given objective function that describes the performance of a given device. There are some extreme examples where the machine has a lot of freedom to create a geometry but that could lead to manufacturing impossibilities hence the necessity of constraining the structure to a pre-set design. For example, in nanophotonics where layer-by-layer deposition and masks are used to pattern the layers, only certain types of structures can be engineered with given materials. We can let the algorithm decide on the thickness of the layers within given bounds and some geometrical features if we know we will be able to implement them.
The objective function is rarely defined explicitly but it doesn't need to be, some algorithms are designed to search for an optimal solution by locally evaluating a function without requiring global information about the objective function. We can use finite element analysis or experiments to feed the inverse design algorithm and let it find a local (hopefully global) extremum. We will also refer to this objective function as a "figure of merit" (FOM) and give it a minimum value at the optimal point, the inverse design algorithm has to minimise the FOM by convention.

A common idea in these class of algorithms is the exploration/exploitation algorithm. If a given set of parameters gives a good functional structure which is therefore well evaluated, one could wonder if it is a good idea to search around that point and fine-tune the solution or keep exploring for better solutions (it is possible that we only found a local minimum of the FOM). Keeping the exploration may lead to a better solution to be found but simultaneously increases the simulation time, maybe it is better to fine-tune the already-satisfactory result ? This trade-off between exploring the configuration space or focusing on points with good results is a common dilemma in machine learning and we will show here how we approached it.

4.2 Exploration - Exploitation

In general, an optimisation algorithm has to explore a vast n-dimensional space, at each point it tests, a FOM value is calculated. The goal is to find the lowest value over the entire authorised space without evaluating too many points. Algorithms that explore many configurations have better chances of finding a new FOM dip where the global minimum may be found but this approach requires more time, this has to be compensated by a less thorough search at each value of interest. Symmetrically, implementing a complete search around a point that is deemed interesting enables us to find a local minimum precisely but may miss other regions where other (possibly even lower) minima are. In order to solve this exploration-exploitation dilemma, we chose an hybrid Particle Swarm Optimisation (PSO) - interior point algorithm that works in two steps. First a Particle Swarm Optimisation Algorithm (PSOA) explores a vast configuration space and roughly optimises each minimum. The best value found by this algorithm is then fined-tuned by the interior point algorithm that is a gradient-descent based method implementing external constraints.
Finding a FOM that has nice properties like continuity, derivability or k-Lipschitz continuity helps us finding this global minimum. There are however a few "traps" one should avoid for an algorithmic search :

- Local minima
- Vanishing gradient

Most approaches are gradient descent-based, which means that the next point that is calculated is derived from the previous point and the "slope" of the FOM along each dimension.

This is often done by evaluating the function at x_k and for all i, $x_k + \delta_i$ where δ_i is a very small vector aligned with the i^{th} vector of a base of the configuration space. The next step is then calculated with :

$$x_{k+1} = x_k - \alpha.\nabla f(x_k) \tag{4.1}$$

Where α is a convergence parameter, high values create larger steps that can accelerate convergence but simultaneously increase instability of the solution (and vice-versa). Such approaches fail to escape local minima if necessary precautions are not taken, it is possible to add "inertia" to escape such minima if they are low enough, this approach is implemented in PSO algorithms. One can also run several searches, starting from different point in the configuration space so that they can converge towards possibly different minima. Vanishing gradient regions can also be problematic for gradient-based searches as the search may stay stuck in these regions for many iterations. Convergence tests allow the termination of the optimisation if the solution is not updated significantly at every step.

4.3 Particle Swarm Optimisation

The particle swarm optimisation is a bio-mimetic algorithm that was inspired by swarm of animals accomplishing a task in group, like searching for food. It uses a number of "particles" that each travel individually step-by-step in the configuration space following a number of "forces" that direct their trajectory :

- Inertia : each particle has a velocity in the search-space and keeps a certain amount of this velocity from one step to the next
- Attraction to its own optimum : each particle through its journey has evaluated a number of positions, it remembers them all and is always attracted to some extent towards the position it remembers as being the best (minimal FOM)
- Attraction towards the global optimum : all the particles "communicate" and know where the best evaluation has been found by all members of the swarm. This global optimum is subject to change at each step and acts as an attractor for all particles.

The weight of each component leads to different swarm behavior, each particle starts with a random position and velocity in the configuration space and can only move in this space. This makes the implementation of constraints very simple, enabling the user to prevent man-

ufacturing impossibilities and shortening the simulation time by indicating where a solution should be found (by forbidding extreme values that shouldn't lead to an optimum).

4.4 Interior point algorithm

The interior point algorithm is a modified gradient descent algorithm that takes into account boundaries or constraints. It is included in the optimisation toolbox in MATLAB and enables a fast implementation for our inverse design application. We only use a very small part of the versatility of this algorithm as we simply use constant boundaries on each parameter's value.

The idea to implement constraints is to add a barrier function that takes very high values when the constraint is not respected. Instead of minimising the figure of merit, we solve the adjacent problem "minimise the figure of merit + the barrier function". This barrier posses an easily calculable gradient that incentivises the gradient descent method to respect the constraint by pushing the solution towards a region where the constraint violation is lower.

More formally, we have the following initial problem : minimise f(x) subject to $c_i(x)$ for i=1,...,m $x \in \mathbb{R}^n$, where $f : \mathbb{R}^n \to \mathbb{R}$, $c_i : \mathbb{R}^n \to \mathbb{R}$.We define the barrier function associated with this problem :

$$B(x, \mu) = f(x) - \mu \sum_{i=1}^{m} log(c_i(x)) \tag{4.2}$$

μ is a small parameter used to scale the barrier, it eventually converges to 0 and the minimum of $B(x, \mu)$ would tend towards a minimum of f. Interior points algorithms are a class of algorithms and an active field of research in computer science and mathematics, presenting the details of a precise algorithm would be out of the scope of this thesis. We will not detail the precise implementation of the algorithm used on Matlab but we show the settings used in our script in the appendix for reproducibility purposes.

Other algorithms exist that could also have solved a multi-parameter optimisation problem without global knowledge about the FOM. More information can be found for inverse design in this paper [80], given the characteristics of the problem we face (non-discrete problem, no good initial guess, fast computation time), this article advises the PSO algorithm, the "Covariance matrix adaptation evolution strategy" (CMA-ES) algorithm and the wind driven optimisation (WDO) algorithm.

Chapter 5

Beam steering structure

In this chapter, we explain the design choices made to implement a fully tunable binary controlled metasurface using Vanadium dioxide, we engineer and optimise a single antenna using inverse design before using it in an array configuration. We first explain the challenges and how the antenna's structure is meant to answer them. We then show how the inverse design algorithm is implemented to reach the specifications, especially focussing on the figure of merit that we try to optimise. Finally, we characterise the antenna's behavior over a full VO_2 transition, its broadband characteristics and its robustness to manufacturing imperfections.

5.1 Structure

As we saw in chapter 3, binary control is ideally implemented with an antenna that exhibits a π phase shift between both states and a similar reflection amplitude.

The antennas also have to be controlled individually : as we plan to use Joule heating to trigger the VO_2 element's transition, it is necessary to maintain a good thermal insulation between two adjacent antennas. We remember that antennas are sub-wavelength features so their dimensions are of the order of 100 nm, keeping a thermal contrast at least larger than the transition and hysteresis width combined on such small dimensions is a challenge. This will require high heat-fluxes, a thick thermally insulating layer and excellent thermal dissipation in the substrate. The material chosen to insulate antennas thermally from each other is silicon dioxide : it is easily manufactured and has a very low thermal conductivity of 1 to 1.4W/mK [81].

As reported previously, the MIM (Metal-Insulator-Metal) structure has a resonant behavior than can be used to apply a phase shift at reflection [1, 3, 23, 28, 30, 57, 70, 82]. In order to tune this MIM resonator, the "insulator" layer will be composed of Vanadium dioxide

sandwiched between two gold layers. To facilitate the deposition of VO_2 on top of a gold layer, a 2 nm Ti layer will be added for adhesion purposes, due to the small thickness, the impact on the resonant behaviour should be minimal. Since no issue to deposit gold on a VO_2 layer has been reported in the literature nor in our research group, no Ti adhesion layer is applied on top of the VO_2 element. The top metallic layer will be used to trigger VO_2 transition by Joule heating by letting a current flow in it so its dimensions will not depend only on the antenna performance but also on thermal engineering constraints.
The antenna is build upon an optically thick metallic backplane that both maximises reflectivity and dissipates the heat efficiently with its high thermal conductivity. We used a gold backplane in the main design but we later show a less expensive version using copper with minimal performance degradation.
The overall structure we described is shown in figure 5.1 with the following stack order summary from bottom to top :

- Optically thick metallic backplane, gold
- Thermally insulating SIO_2 layer
- Metallic layer (**M**IM layer), gold
- Thin 2 nm Ti adhesion layer
- Tunable VO_2 layer (M**I**M layer),
- Metallic layer (MI**M** layer), gold, used for Joule heating

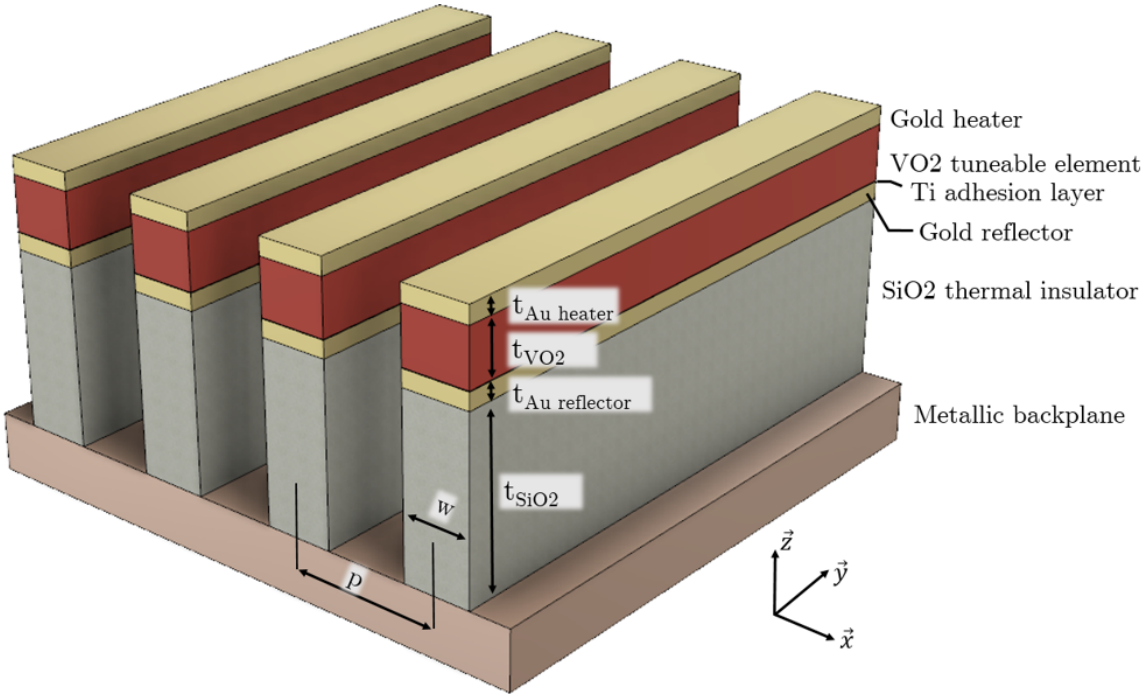

Figure 5.1: Proposed structure design.

5.2 Figure of merit

In order to implement a π phase contrast and equal reflectivity between both states whilst maximising the amplitude of the reflected field, we tried several figures of merit (FOM). For all attempts, we used a two-components FOM that is the product of a phased-based and a reflectance-based FOM.

The first one was simply implemented by calculating the value of a Gaussian curve centered around π with an arbitrary $\pi/9$ (20°) standard deviation at the phase shift difference between the two extreme VO_2 states. The FOM is maximum for a π phase shift, exhibits vanishing values at phase contrast far from π and a "tolerance zone" around π with a significant gradient to help the algorithm optimisation converge. Another interesting property of this figure of merit is that it is locally equivalent to a cos^2 function. As we saw in section 3.1.4, the impact of a phase shift inaccuracy δ on the main lobe amplitude is equivalent to a multiplication by $cos(\delta)^2$. The 2^{nd} order Taylor expansion of e^{-x^2} and $cos(x)^2$ is the same : $1-x^2+x^4/4+\circ(x^6)$. Several reflectivity-based FOM were tested until a satisfying one was found. A number of combinations of the two reflectivity was tried : arithmetic mean, geometric mean, log and exponents-based adaptations of these mean values. They all had the same kind of behavior but to different extents, in all cases, it was favorable for the algorithm to maximise a state's

reflectivity at the expense of the other. This would lead to side lobes as was shown in chapter 3, even if one state's reflectivity can be highly increased at the cost of a small reflectivity drop in the other state, it is not worth implementing. The FOM component we finally chose and tested with success was the minimum of both state's reflectivity. This FOM only incentivises the algorithm to increase the reflectivity of the state that has the smallest reflection amplitude, thus decreasing the contrast between them. It is also directly proportional to the reflectivity values, therefore encouraging the algorithm to find designs that have a high overall reflectivity. The final FOM we used is therefore the following :

$$FOM = Gauss(\Delta\Phi, \pi, \pi/9) * min(R_0, R_1) \tag{5.1}$$

With $\Delta\Phi$ the phase shift difference between both states, $Gauss(x, y, z)$ being the evaluation at x of a Gaussian function with mean y and standard deviation z and R_0, R_1, respectively the reflectivity of the OFF and ON states.

5.3 Thermal design

Two thermal challenges have to be addressed at different scales. At the antenna-scale, we need to prevent thermal cross-talk, this is not a trivial task as we have to maintain a significant temperature difference over a few hundreds of nanometers. At the array scale, we need to dissipate the heat generated by all the antennas, if the absolute power is relatively low (a few W), the heat flux is however very high ($\sim 2000\ W/cm^2$).

A few points have to be clarified before we move on to the thermal models and design :

- The thermal capacity of VO_2 was drastically simplified, we used a specific heat $C_p = 730 J/kg.K$ and thermal conductivity $k_{VO_2} = 4\ W/m.K$ which would correspond to average values over the transition. A more complicated model can be used but the additional complexity wouldn't bring more insight into the thermal behavior of the antenna. More information about thermal properties of VO_2 thin films around their transition can be found in the following study [83].

- The thermal resistance of layer-layer interfaces is neglected, in practice, it can only increase the thermal resistance between two adjacent antennas which would help increase thermal contrast. This is a positive effect we did not take into account.

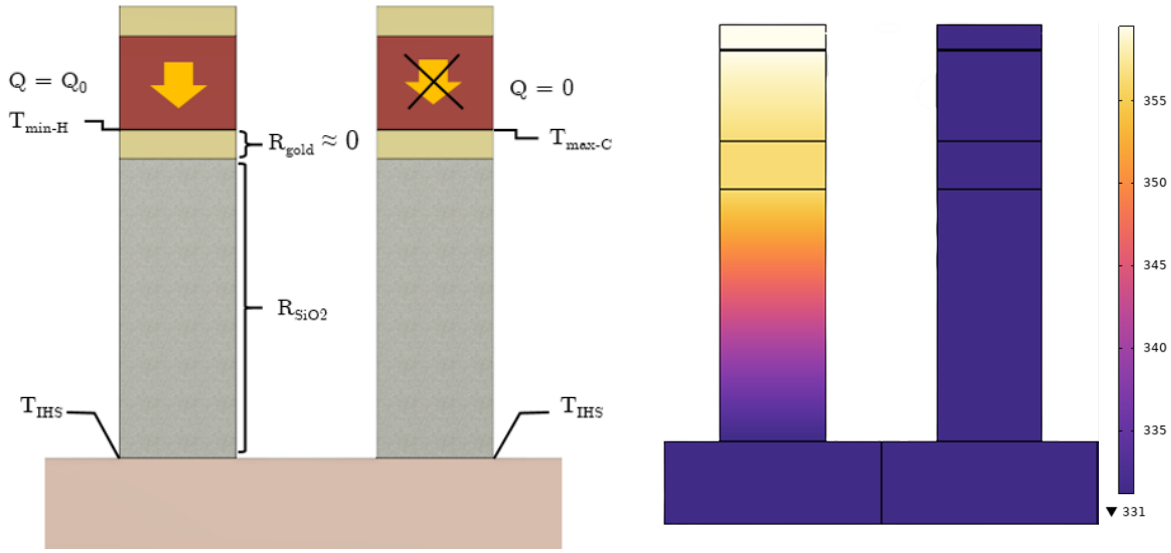

Figure 5.2: a. Heat transfer diagram for the antenna-scale problem b. Steady state temperature distribution calculated using finite element, only the antenna on the left is turned ON.

The antenna-scale heat problem is summarized in Figure 5.2a in a heat transfer diagram, the minimum thermal insulator thickness $t_{insulator}$ necessary to ensure a thermal contrast ΔT is calculated in equation 5.2.

$$t_{insulator} = \frac{\Delta T.k}{t_{Au} Q_{vol}} \tag{5.2}$$

where k is the thermal conductivity of the insulator and Q_{vol} is the volumetric heat generation in W/m^3, we set this value to $9,67.10^{14}$ which corresponds to a current density of $2.10^{11} A/m^2$, 10 times less than the experimental limit reported by Durkan et al. [84]. We arbitrarily set $\Delta T = 25°C$ to obtain a wide temperature contrast and ensure a full VO_2 transition in both the cold and hot states with a significant margin on both sides. The SiO_2 thickness can be brought down by increasing the heat generation, the value of $t_{Au} = 60\ nm$ was found to be a good compromise between optical properties (which favors lower Au thickness as we will see later) and thermal performance (more heat generation with higher heater volume). With the aforementioned parameters, a SiO_2 insulating layer of 600 nm is required to obtain $\Delta T = 25°$.

The steady-state temperature distribution in the array has been calculated using the commercially available finite element code COMSOL, the results are shown in Figure 5.2b. The IHS temperature was set to $T_{IHS} = 58°C = Tc - 10°C$, we note that the convective heat transfer with ambient air is negligible at the antenna scale. The thermal contrast in the sim-

ulations agrees well with the calculations, the small discrepancy is due to the gold thickness whose thermal resistance and conduction in the substrate are neglected in our calculation. The transient behavior has similarly been modelled in Figure 5.3 and we find a very fast settling time, in the order of $1 - 2\mu s$ which could be expected given the high energy density in the device.

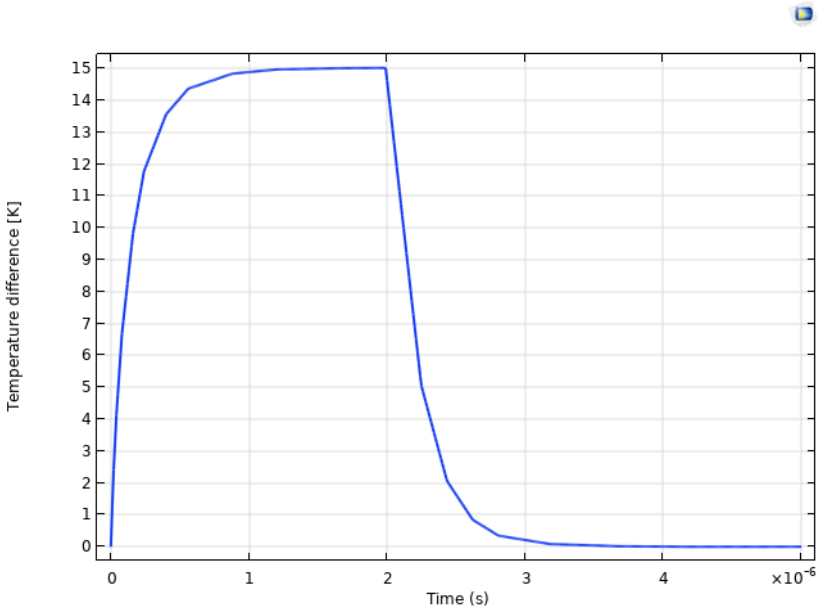

Figure 5.3: Transient thermal response of the antenna to $5\mu s$ Q_{vol} pulse (rising and settling behavior).

Regarding the heat dissipation problem, we begin with the calculation of the heat flux value (q in figure 5.4). We average out the heat generation at the array scale per unit surface, this value is then used in an analytical model in a later time. We consider the energy consumed in a square of dimensions $S = p * p$ where p is the array period, this corresponds to a length of p over a single antenna.

$$E_d = \frac{V * Q_{vol}}{S} = \frac{t_{Au-thermal} * p * w * Q_{vol}}{p^2} = \frac{t_{Au-thermal} * p * w * \Delta T * k}{t_{SiO_2} * t_{Au-thermal} * p^2} = \frac{w * \Delta T * k}{p * t_{SiO_2}} \tag{5.3}$$

If we use $p = 517\ nm$, $w = 245\ nm$, $\Delta T = 25°$, $k = 1.4\ W/mK$ and $t_{SiO_2} = 600\ nm$, we calculate with equation 5.3 : $E_d = 2770\ W/cm^2$.

The array scale heat dissipation problem has already been studied intensively by microprocessor manufacturers [85, 86], the use of Internal Heat Spreaders (IHS) is generalized in the industry to cool down small components like our array. The idea is to spread the heat

in a conductive plate to dissipate it over a larger surface area. An efficient IHS is necessary to cool down the array without resorting to more complex cooling methods, like the use of cryogenics, liquids or enhanced forced convection. This means we need a thermally conductive substrate hence the use of a metallic backplane in our structure, SiO_2 or other insulating materials are not suitable.

We shortly present the IHS model calculations without going in the details of the analytical derivation as this has already been covered extensively in the literature [85]. We also remind the reader that most if not all of the parameters result from engineering choices that depend on many external factors and are not the outcome of a direct optimisation. We have to keep in mind that they can be adjusted if necessary to accommodate specific design requirements but this will also impact other parameters. For example, we can link the temperature contrast between adjacent antennas, the insulating layer thickness, its thermal conductivity, the heating layer conductivity and the current density during heating. If we decide to modify one of these parameters (which is completely possible), it will affect one or more of the others.

We took a relatively conservative approach in the antenna thermal design with large tolerances, for example the current density is a full order of magnitude below the experimental limit and the temperature contrast is $\Delta T = 25K$, a very large value that leaves plenty of space for error on either side of the transition width (in order to make sure the OFF state is well below T_c and the hot state well above). We will take similarly conservative specifications for the IHS design to show that our proposition is realistic. However, it is very likely that the limitations we calculate here can be pushed further by reducing the margins or using more advanced experimental conditions.

The IHS model calculates the thermal resistance of a heat spreader, it is then put in parallel with the thermal resistance of the convection phenomenon. We therefore have to calculate both thermal resistances separately and add them to calculate the temperature increase in the array. We make the following assumptions :

- On average, half of the array's antennas will be in the ON state, the array is continuously working so that the incident heat flux is half of E_d calculated in equation 5.3.

- The cooling is done with air at $T_{air} = 20°C$, we assume $h = 10W/m^2K$ which would correspond to a very light forced convection case.

- The IHS model assumes heating and cooling on different sides of the heat spreader, which is not the case in our proposition. We assume the difference in thermal resistance is negligible when we have a thickness close to the optimum.
- The surface of the substrate is $A_1 = 1cm^2$, this is the surface of the IHS.
- The array is a square, meaning the length of the antennas increases with their number ($w_{array} = l_{array} = N.p$).
- We use gold as a substrate, it has a thermal conductivity $k_{Au} = 310W/mK$, copper would actually give a lower IHS thermal resistance as $k_{Cu} = 400W/mK$ but we conducted all the FDTD simulations using an optically thick Au backplane.

The IHS model calculations comprises the following steps :

- calculate dimensionless dimensions (length scales)
- calculate dimensionless thermal resistances
- scale up the problem with the actual dimensions
- calculate the heat transfer equilibrium temperatures

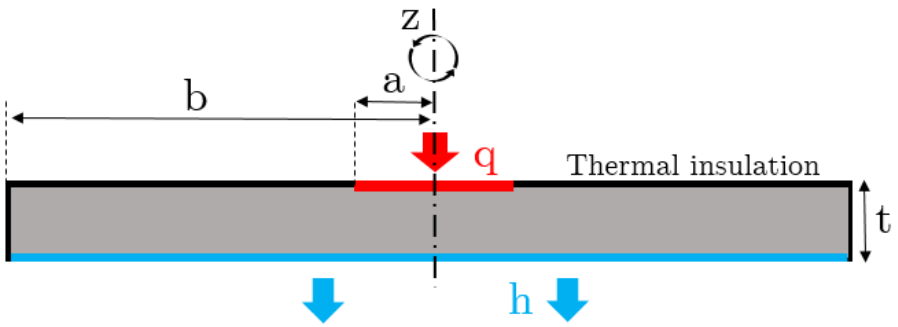

Figure 5.4: IHS model schematic.

The parameters of this model are shown in figure 5.4. First for a non-circular source and spreader, the effective dimensions are calculated as :

$$a = \sqrt{\frac{A_1}{\pi}} \quad b = \sqrt{\frac{p_1^2}{\pi}}$$

The dimensionless heat source radius and plate thickness are respectively

$$\epsilon = \frac{a}{b} \quad \tau = \frac{d}{b}$$

The effective Biot number is defined as

$$Bi = \frac{h.b}{k}$$

From these parameters, we derive Θ and λ : two numbers used as intermediate variables that simplify down the next equations.

$$\lambda = \pi + \frac{1}{\sqrt{\pi}.\epsilon}$$

$$\Theta = \frac{tanh(\lambda\tau) + \frac{\lambda}{Bi}}{1 + \frac{\lambda}{Bi}.tanh(\lambda\tau)}$$

From these, we derive the dimensionless thermal resistances Ψ_{max} and Ψ_{avg} that are respectively used to calculate the maximum and average temperature raise over the IHS.

$$\Psi_{max} = \frac{\epsilon.\tau}{\sqrt{\pi}} + \frac{1-\epsilon}{\sqrt{\pi}}\Theta$$

$$\Psi_{max} = \frac{\epsilon.\tau}{\sqrt{\pi}} + \frac{(1-\epsilon)^{3/2}}{2}\Theta$$

We now calculate the actual thermal resistances

$$R_{max} = \frac{\Psi_{max}}{\sqrt{\pi}.x.a} \quad R_{avg} = \frac{\Psi_{avg}}{\sqrt{\pi}.x.a}$$

The convective heat resistance is simply

$$R_{conv} = \frac{1}{h.A_1} \tag{5.4}$$

Finally, we derive the thermal equilibrium temperatures :

$$T_{max} = T_{air} + q.(R_{max} + R_{conv}) \quad T_{avg} = T_{air} + q.(R_{avg} + R_{conv})$$

Applying the IHS model with the parameters mentioned above, we get the following temperature increases for different array sizes shown in table 5.1.

This data confirms the presence of a critical array size where even the cold state is above T_c. However, we can note that the temperature increase is governed by convection, with our values, $R_{conv} = 1000K/W$ and R_{IHS} goes from $\simeq 200K/W$ with N=16 to $\simeq 20K/W$ with N=256. The limiting phenomenon to further cool the sample would be convection and not the IHS thermal resistance. This means it is easy to push for a higher number of antenna by decreasing the convection resistance, for example with higher air velocity, a larger substrate

N	ΔT_{max}	ΔT_{avg}
16	2.3	2.3
32	8.4	8.3
64	32.1	31.9
128	125.2	124.8
256	496.0	494.9

Table 5.1: Maximum and average temperature increase for a range of array sizes calculated with the IHS model

size or using liquid cooling (see equation 5.4). In figure 5.5, a careful look at the y-axis shows that the spread is minimal and even the edge of the IHS is at a temperature close to its center. Note that we calculated the temperature increase, which is equivalent to setting the ambient temperature (with which there is a convective heat exchange) to $0°C$.

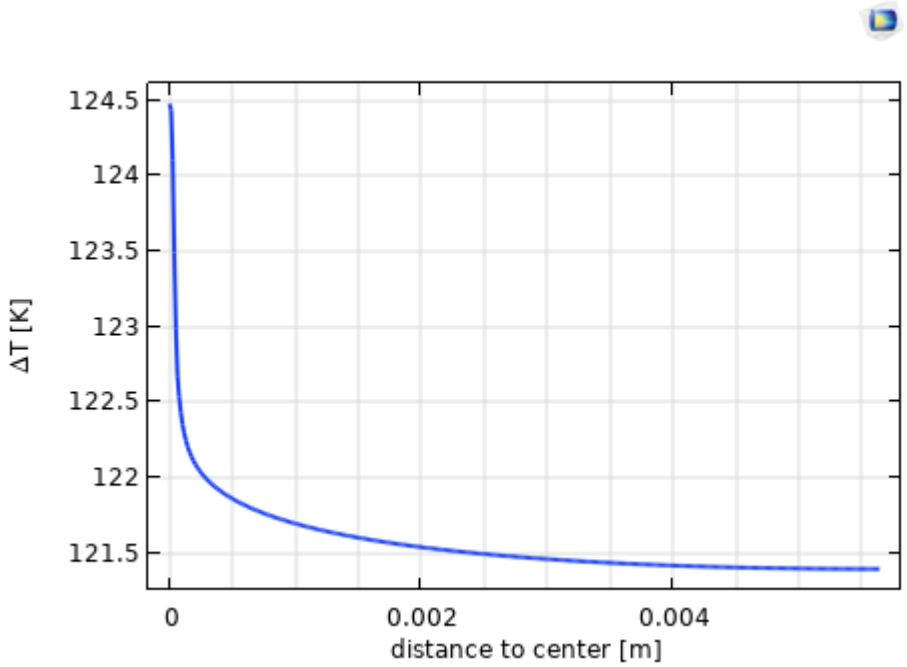

Figure 5.5: Temperature distribution along the IHS arc length (distance to center) for N=128.

The results of IHS model calculations are shown in Table 5.2 and compared to the finite element results, they validate the fact our array can be cooled down efficiently without resorting to advanced methods. ΔT_{avg} corresponds to the average temperature increase in the array and ΔT_{max} to the maximum temperature increase (usually at the center of the array where heat dissipation is the most difficult). Note that as can be seen in Table 5.1, the heat generated by the array scales up with the number of antennas (especially if we want to maintain the length of the antennas proportional to the array width). With given cooling

Method	ΔT_{avg}	ΔT_{max}
IHS model	31.87	32.06
Finite element	31.54	31.77

Table 5.2: Temperature increase: IHS model comparison to finite element simulation for the array-scale cooling problem for N=64.

conditions there will be a critical array size where the cold operating point will be located above the VO_2 transition temperature, rendering it ineffective.

5.4 Design characteristics

In this section, we will often refer to the VO_2 phase denoted as φ which describes the material composition such that $\varphi = 0$ for cold VO_2 and $\varphi = 1$ for hot VO_2 and to the reflected phase noted Φ that is the phase angle of the reflected field.

The algorithm described in chapter 4 outputs the dimensions shown in table 5.3. The value of periodicity was manually set to $\lambda/3$ and the Au thermal layer thickness was also set manually, we chose the value $t_{Au-thermal} = 60\ nm$ which offers a good compromise between heat generation and optical performance as mentioned in the previous section.

We calculate the reflection phase and amplitude over a full gradual VO_2 transition, the intermediate material properties were calculated using the Maxwell Garnett effective medium approximation (EMA)[41]. Equation 5.5 is applied to calculate the dielectric constant $\epsilon_{eff}(\omega)$ of a VO_2 mix with φ_r proportion of rutile (metallic) VO_2, $\epsilon_r(\omega)$ and $\epsilon_m(\omega)$ are respectively the dielectric constant for rutile (metallic) and monoclinic (dielectric) VO_2.

$$\epsilon_{eff}(\omega) = \epsilon_m(\omega)\frac{2\varphi_r(\epsilon_r(\omega) - \epsilon_m(\omega)) + \epsilon_r(\omega) + 2\epsilon_m(\omega)}{2\epsilon_m(\omega) + \epsilon_r(\omega) + \varphi_r(\epsilon_r(\omega) - \epsilon_m(\omega))} \tag{5.5}$$

Parameter	Value (nm)
p	516.7
w	245.2
t_{SiO2}	600
t_{VO2}	216.3
$t_{Authermal}$	60
$t_{Aureflector}$	99.4
t_{Ti}	2

Table 5.3: Parameter values for our design proposal.

The exact processes through which VO_2 thin films undergo a progressive IMT are very complex and non-uniform over the surface [46]. It is however common to approximate the proportion of VO_2 in the film that underwent the IMT by a linear relation [30]. The exact parameters of this linear fit have to be measured in-situ with a given sample as we showed earlier how VO_2 thin films properties depend were highly manufacturing-process dependant. In figure 5.6 we show the phase shift and amplitude of the reflected E_x field for an infinite array of antenna at 1550 nm (a single array with periodic x-boundary conditions was simulated in FDTD), the phase reference was set at 0 for fully cold VO_2 ($\varphi = 0$). Although this antenna is not meant to be controlled with standard phased array continuous control algorithms, it perfectly illustrates the issues we mentioned in the introduction.

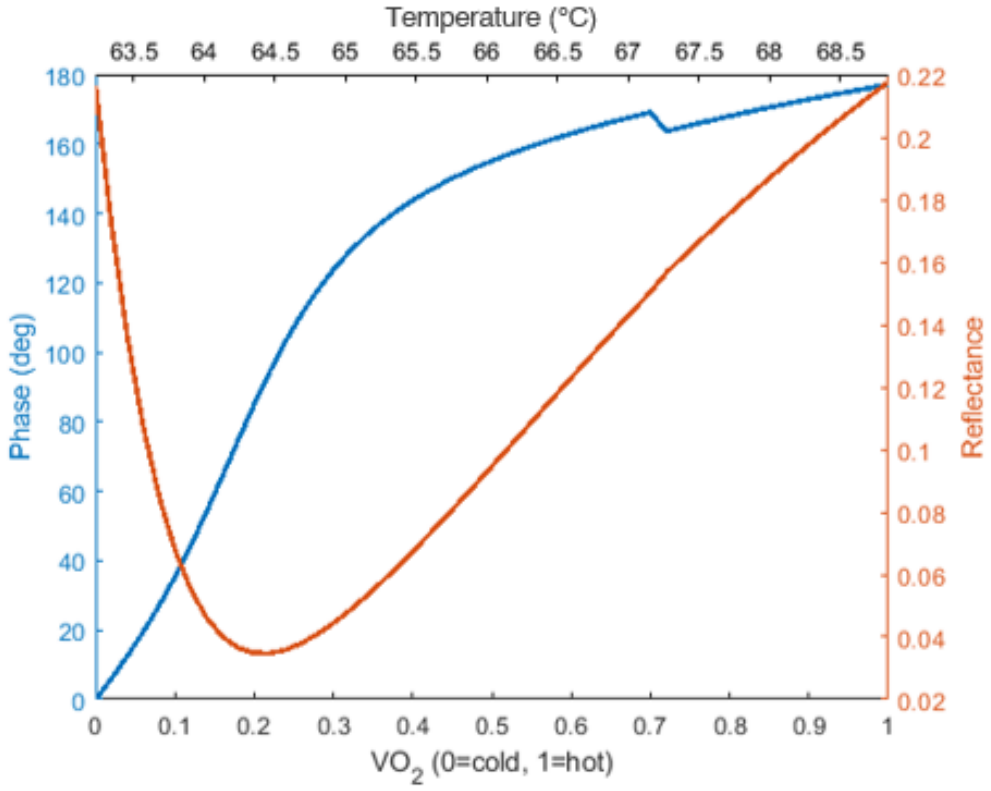

Figure 5.6: Phase and amplitude of the E_x field versus VO_2 composition (proportional to temperature).

- The amplitude is not constant for all phase angles, we have a large phase-amplitude correlation.
- The temperature-phase relation is highly non-linear, making effective phase control challenging in practice.

- The maximum phase shift is 180°, the control range is incomplete as 2π tuning capability is required for ideal control.

This antenna was optimised for a π phase shift but it is impossible to reach a full 2π phase shift using a single resonance. A similar geometry optimised to reach a maximum phase shift can achieve a maximum phase shift of 240° but with an extremely abrupt phase shift and 0 amplitude at resonance. As remarked by Kim et al. [1], trying to obtain a larger phase shift usually results in an even larger phase gradient at resonance, making the antenna simply impossible to control. If we test a number of antennas with varying width, we can see that some of them are very close to the resonance state, some of them further away. The antennas that have an operating state close to resonance will showcase a larger phase shift over a full transition but it will be sharper and the minimum amplitude obtained at φ closest to resonance will be vanishingly low. As the antenna width is further away from the resonant width, the overall phase shift decreases but is also smoother, furthermore, the amplitude dip is not as strong. The maximum obtainable phase shift reported by Kim et al. was 250°, we reached similar values with a specific geometry but such an antenna would not be a reasonable choice for a phased array. It is preferable to decrease the maximum phase shift to have a smoother $\Phi(\varphi)$ characteristic curve and a lower resonance dip if one wants to implement a classical phased array.

The broadband behaviour of the antenna was also assessed through FDTD simulations. We can see in figure 5.7 the phase shift between the two antenna states and the reflectance for each of them in the wavelength range [1400 nm-1700 nm]. It seems that the antenna is optimised at 1525 or 1660 nm and not 1550 nm as the phase shit at 1550 nm isn't perfectly 180° and the reflectance of the hot and cold state is dissimilar. It must be noted that a slight change in behavior is observed in broadband simulations due to the numerical methods used by FDTD to calculate the phase and reflectance spectra. The material properties are imported in Lumerical as sampled data files but are not used as such. In order to be processed in FDTD simulations, they have to belong to a given class of functions. The dielectric function as used Lumerical is therefore a sum of functions tuned and weighed by a fitting algorithm that minimises the error between the fit and the sampled data. However this fit is never perfect and significant errors may arise if one is not careful enough, checking the fit is always important before doing a broadband simulation. The antennas were optimised in narrowband simulations so the errors were minimal, however for the following simulations, we will observe

a slightly non-ideal behavior at 1550 nm for our design. These errors disappear progressively when we consider shorter band simulations. It can be noted that the reflection coefficients and the phase shift remain very close to what could be expected from an ideal antenna, if we allow a $\pm 5°$ phase shift discrepancy and ± 0.05 reflectance gap, the antenna works between 1510 and 1700 nm. The lack of material property data for wavelengths above 1700 nm prevented us from doing accurate simulations over a larger bandwidth, furthermore, wider band simulations would have higher numerical errors associated to the material properties and the results may not be as reliable. The overall reflectance of the array is $\sim 8\%$, determined by the reflectance ($\sim 21\%$) times the peak power ratio for binary control (~ 0.4).

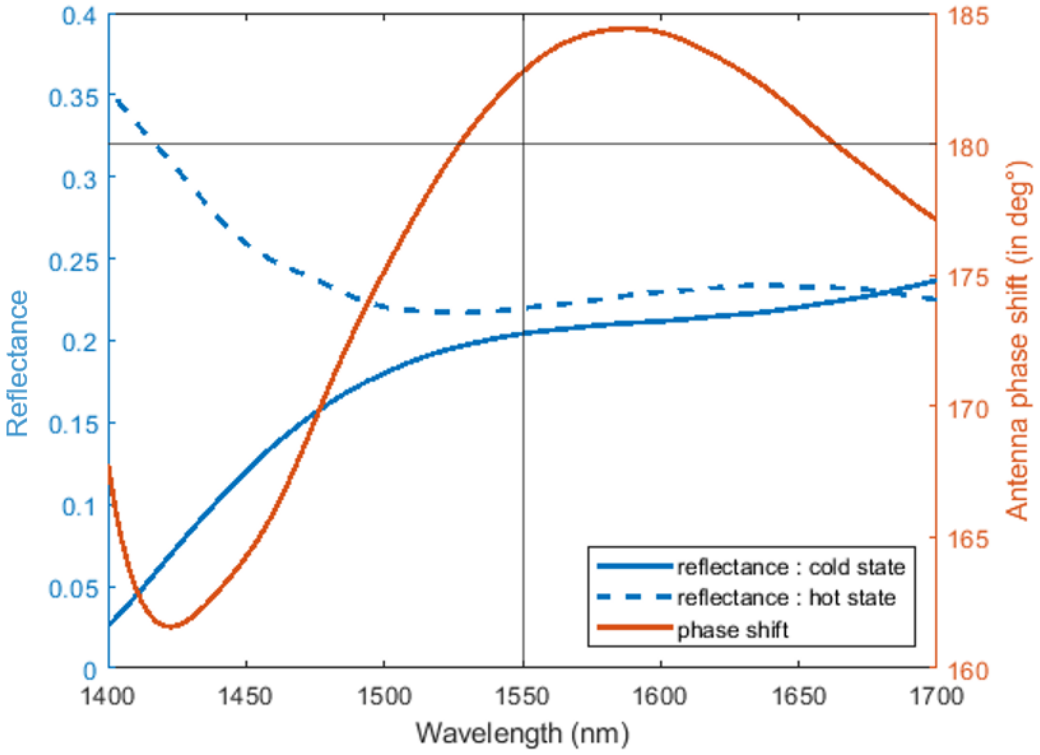

Figure 5.7: Phase contrast and reflectance of the cold and hot state versus wavelength.

The FDTD simulations calculate the E and H fields in the antenna and enable us to visualise the resonance phenomenon dependence on the VO_2 phase. In Figure 5.8, we see the Hz field for hot and cold VO_2, a magnetic dipole resonance is clearly visible as reported in other similar structures [1].

Unlike other resonant structures [87], the broadband capabilities of our design enables new possibilities. It is possible to imagine wavelength multiplexing to scan several angles at once. This device behaves closely to a perfect binary antenna with π phase shift and unity

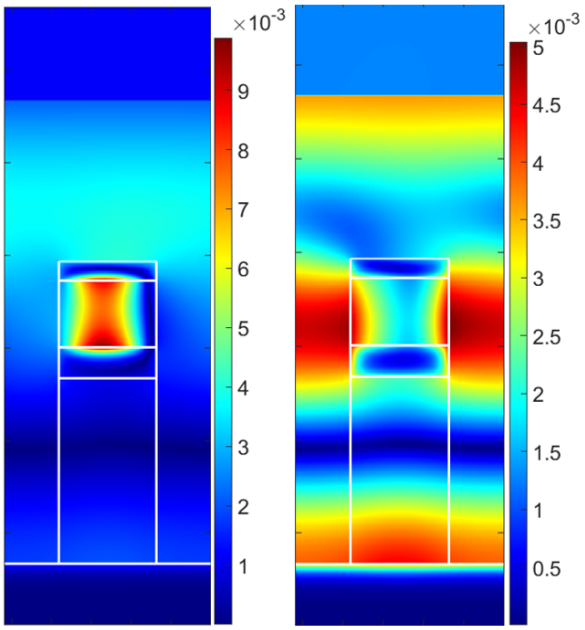

Figure 5.8: FDTD simulation at 1550 nm of the magnetic field H_y field in the antenna in its dielectric cold state and metallic hot state, respectively. The small asymmetry in the fields is due to the non-normal incidence angle ($\theta_i = 45\circ$).

amplitude ratio between both states over a broad wavelength band. If the incident beam is the superposition of two (or more) coherent beams operating at different wavelengths, the anomalous reflection will separate them. Using different detectors for each wavelength, we can discriminate the reflection from two different angles, thus doubling (or more) the scanning speed of the array in LIDAR applications.

Say we have a target angle θ_r for the beam component at λ, the phase gradient will be calculated using equation 5.6 that is a rearrangement of equation 2.1.

$$\frac{\Delta\Phi}{\Delta x} = \frac{2\pi}{\lambda}.[sin(\theta_i) - sin(\theta_r)] \tag{5.6}$$

This phase gradient will be the same for the beam component at λ' but the angle of anomalous reflection θ'_r will differ by a factor shown in equation 5.7. We note that it is also entirely possible to have $\theta'_i \neq \theta_i$ if the two beams are indeed angularly separated, this solution may even be easier to implement as it does not require to align two beams from different sources. Furthermore, it would enable a more significant angular difference between the two scanning beams without necessitating a large wavelength difference between the sources.

$$\frac{sin(\theta'_i) - sin(\theta'_r)}{sin(\theta_i) - sin(\theta_r)} = \frac{\lambda'}{\lambda} \tag{5.7}$$

Of course, using multiple wavelengths can have direct applications in 2D scanning, with N_y beams being focused on the array at different γ angles (as defined in figure 3.6), we can measure a 2D far-field. The γ scan would be simultaneously done with N_y beams reflected "normally" by a 1D phased array. A grating-structured top layer could also be imagined to implement γ scan with a single tunable laser input but that would be out of the scope of this paper as the geometric changes would be significant.

5.5 Beam steering demonstration

We apply the binary control algorithm to an array of the antenna described in the previous section and perform an FDTD simulation of the entire device in a given configuration. We choose an incidence angle $\theta_i = 45°$ and two angles of anomalous reflection, $\theta_r = 20°$ and $\theta_r = 0°$. For N=32, the ON-OFF pattern are given in binary (0=OFF, 1=ON) below for both angles of anomalous reflection :

- $\theta_r = 20°$: 0-1-1-0-1-1-0-1-0-0-1-0-0-1-0-0-1-0-1-1-0-1-1-0-1-1-0-1-0-0-1-0.
- $\theta_r = 0°$: 0-0-1-1-0-0-1-1-0-0-1-1-0-0-1-1-0-0-0-1-1-0-0-1-1-0-0-1-1-0-0-1.

Thanks to the FDTD simulations, we can visualise the E_x and H_y fields, the antenna pattern is easily recognisable in the H_y field map as shown in Figure 5.9. We can recognise beam steering at $\theta_r = 20°$ and $\theta_r = 0°$ in Figure 5.10 above the FDTD source.

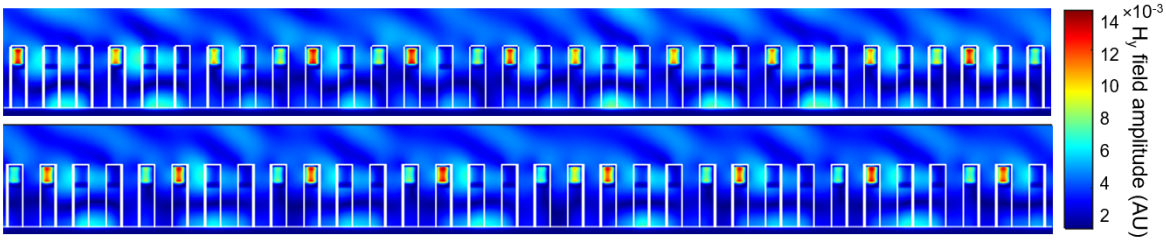

Figure 5.9: H_y field amplitude for $\theta_i = 45°$, $\theta_r = 20°$ (top) and $\theta_r = 0°$ (bot) respectively, we can compare this figure to Figure 5.8 and easily see the antennas in the cold state exhibit a magnetic dipole resonance in the VO2 element.

The E_x field for $\theta_r = 20°$ is then projected in the far-field using Lumerical "farfield" tool and compared to the analytical calculations from first principles (equation 3.7), the results are shown in figure 5.11. An excellent match is achieved despite a slightly higher side lobe level, the electromagnetic crosstalk effects that could be feared do not have major consequences on the phased array behaviour.

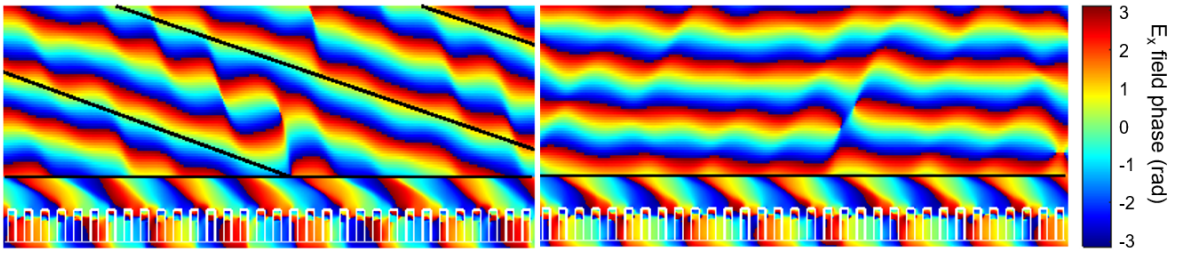

Figure 5.10: E_x field amplitude for $\theta_i = 45°$, $\theta_r = 20°$ (left) and $\theta_r = 0°$ (right) respectively, we can clearly see beam steering even in the near field. The horizontal black line materializes the source position, we see the incident wave below the source and the reflected field above.

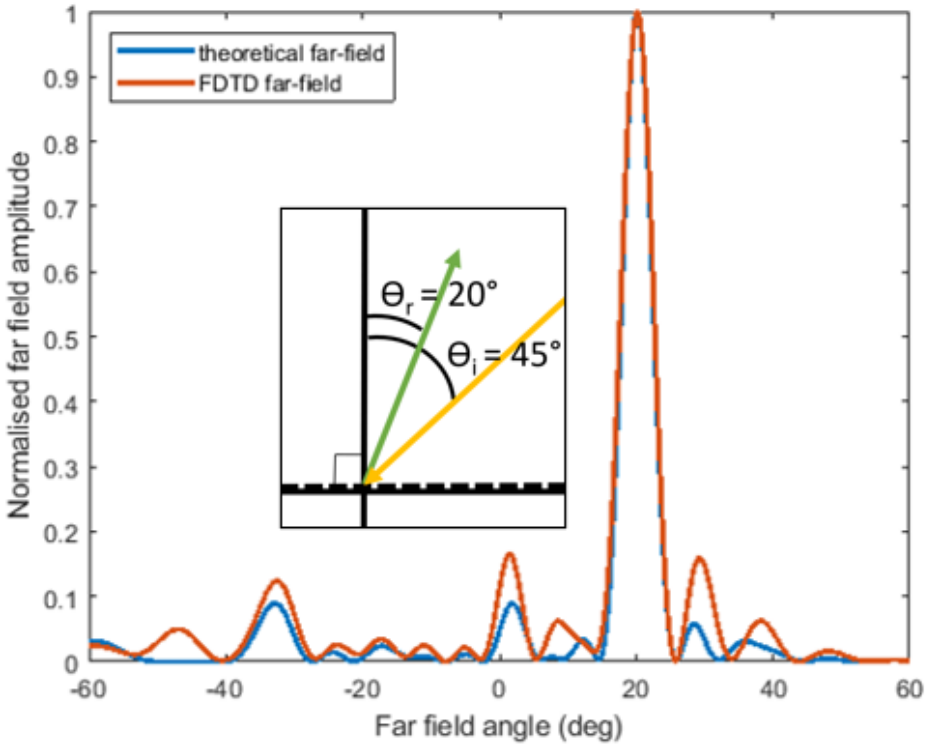

Figure 5.11: Far field projection of the E-field obtained through FDTD simulations (red) compared to the direct theoretical E-field distribution from equation 3.7, incident angle $\theta_i = 45°$, desired reflection angle $\theta_r = 20°$. Inset, schematic showing the angles of incidence and reflection on the array.

5.6 Design stability

To verify our design is robust to manufacturing inaccuracies, we assessed the performance of a large number of antennas built with random perturbations. This method enables us to see the cross-effects of several inaccuracies on the antenna behavior, which individual parameter sweeps cannot do. As the number of parameters is large, we could also not systematically explore nor represent this large n-dimensional space. We used a constant probability distribution for each parameter between $\pm\Delta_i$ (see Table 5.4) to create each individual inaccurate antenna design, the effect on the amplitude ratio and phase discrepancy are shown in Figure 5.12. We note that choosing a constant probability density for the manufacturing inaccuracies is a conservative approach as in reality, extreme errors are less likely to occur than smaller ones. It is however less complex and therefore more reproducible to use this method even if it overestimates the occurrence of large manufacturing inaccuracies.

In order to further analyse this data, we can quantify the spread in phase discrepancy and reflection ratio as shown in Figure 5.13. A Gaussian fit applied to the phase shift discrepancy gives an average of 1.60° and a standard deviation of 10.5°. Similarly for the transmission ratio we obtain an average of 0.986 and a standard deviation of 0.122. The average values are very close to the ideal (0° and 1) and the standard deviations are reasonably low despite the conservative Δi chosen and the constant probability distribution that does not penalize extreme inaccuracies. From these simulations, one can be confident our design is robust to all types of fabrication inaccuracies.

This stability is intrinsically linked to the broadband properties of our design. Manufacturing inaccuracies displace the resonant wavelength, as our design's performance is relatively insensitive to wavelength over a large band, it is similarly insensitive to manufacturing errors. The high losses in VO_2 that lower the Q-factor of the resonance are therefore an asset to

Parameter	Value (nm)	Δ_i (nm)
p	516.7	20
w	245.2	20
t_{SiO2}	600	5
t_{VO2}	216.3	5
$t_{Authermal}$	60	5
$t_{Aureflector}$	99.4	5
t_{Ti}	2	1

Table 5.4: Parameter values and manufacturing uncertainty used in the stability analysis.

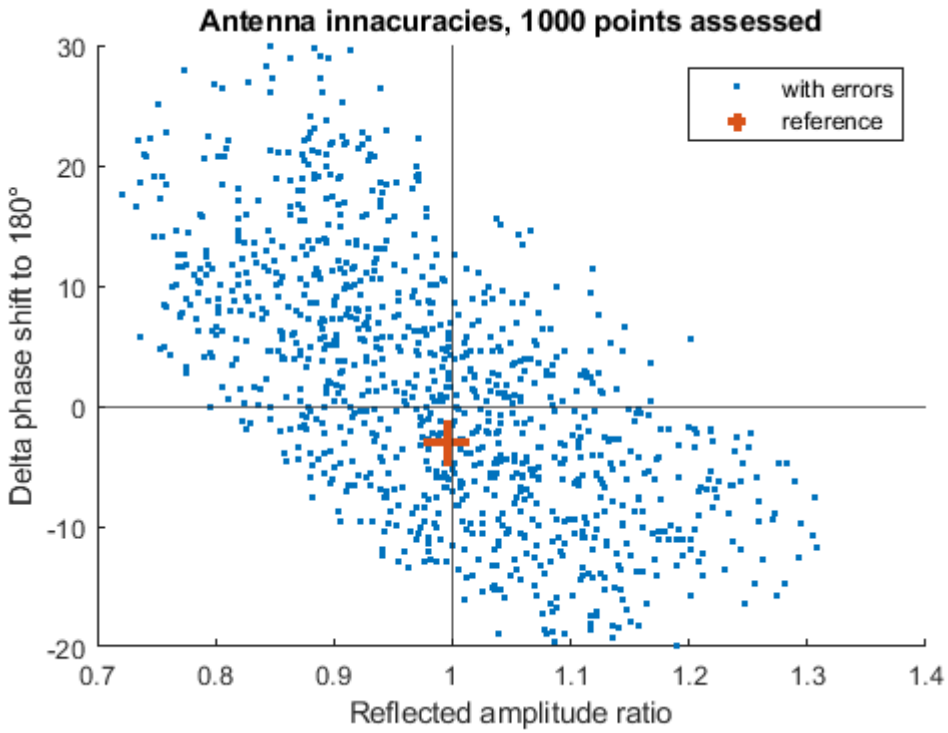

Figure 5.12: Stability analysis results for 1000 inaccurate antennas.

some extent since they enable our structure to operate despite small variations with regard to theory.

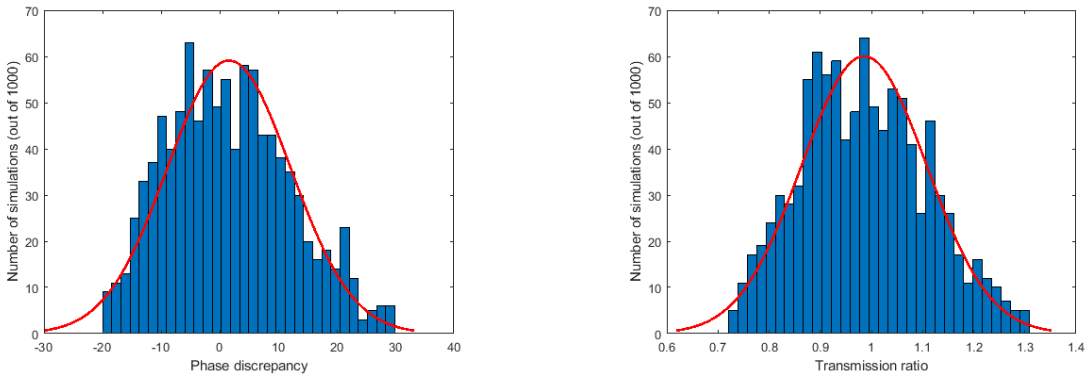

Figure 5.13: Phase discrepancy (left) and reflectance ratio (right) spread (with Gaussian fit).

5.7 Influence of the array periodicity

In order to better understand the behavior of the antenna, we conducted a number of simulation-based experiments. Technically, the antenna is a resonator and it produces a phase shift on its own, should the free space between adjacent antennas therefore be ig-

nored ? By pushing this idea to the limit, we find two situations were the device cannot work.

- If two adjacent antennas were touching, we would simply have a planar MIM structure, as we know that the width of the element is a parameter of great importance, this surface would not work. If the spacing is too small, we can also expect coupling between adjacent antennas and therefore a change in their behavior.

- If two adjacent antennas were spaced far apart, the array would mostly reflect the incident wave with its backplane, not the antenna. One can therefore not expect anything to happen if we increase the period value indefinitely.

The spacing value has therefore a great importance as it is expected to change the resonant behavior with small p values and to extinguish it with large spacing. An other reason why the antenna spacing could be of importance is the design of aperiodic phased arrays : ideally the antenna's response should remain unchanged if the period changes. Decoupling the antenna's resonance would make the entire array design more practical, reliable and performant.
We conduct a periodicity sweep for fixed widths and thicknesses, the simulation bandwidth is large from 1200 to 1600 nm to visualise resonant frequency sweeps. The maximum obtainable phase shift from over a complete VO_2 transition is shown in figure 5.14, if we restrict ourselves to a single wavelength, we can visualise the phase shift versus φ in figure 5.15 at $\lambda = 1550$ nm.

Figure 5.14 contains a lot of interesting information and allows us to verify some claims we made earlier. First of all, the resonance disappears for large period values (around 600 nm here, for an antenna width of 200 nm) as the incident field is mostly reflected by the metallic backplane and not the resonant antenna. Then, we see than the resonant wavelength shifts drastically with lower array periods, this illustrates the higher antenna-antenna interaction as they come closer from each other. We

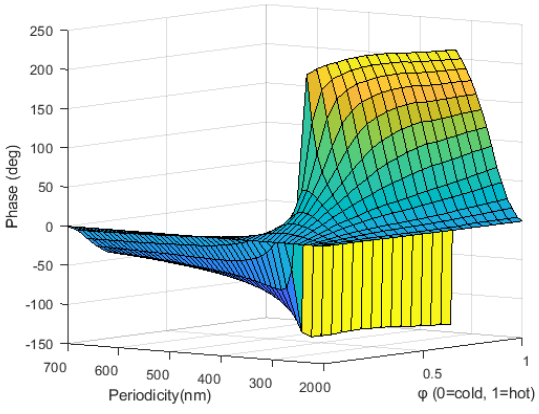

Figure 5.15: Phase shift versus wavelength and VO_2 composition at $\lambda = 1550$ nm.

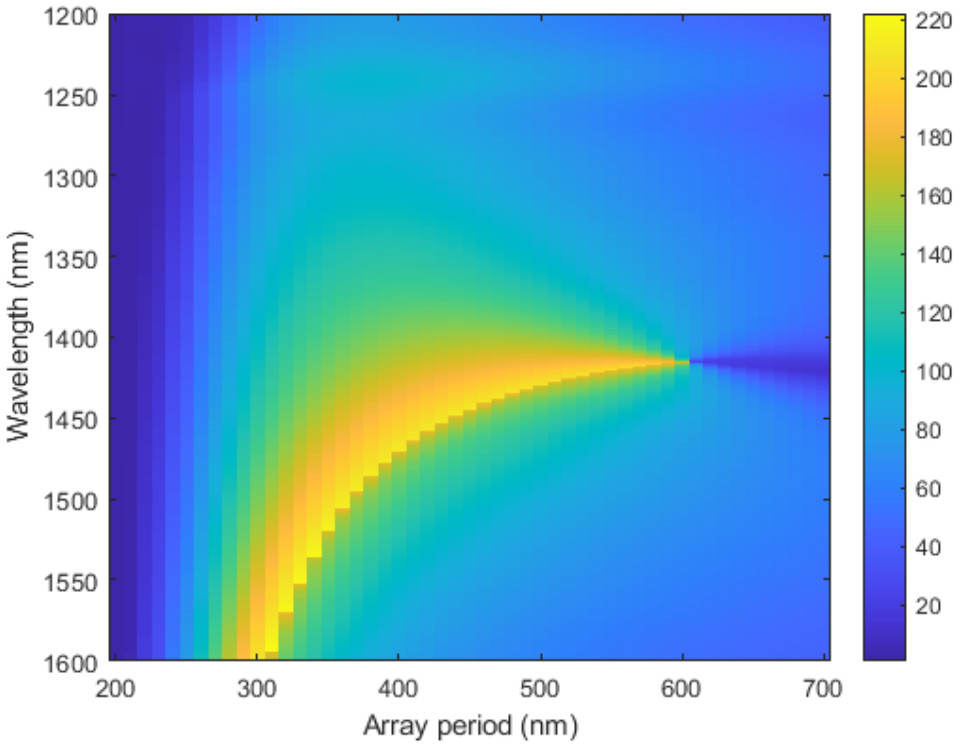

Figure 5.14: Maximum obtainable phase shift from over a complete VO_2 transition versus array period.

can distinguish two zones from these asymp-

totes :

- For large array periods, we have a stable narrowband behavior : the maximum phase shift can only be obtained over a band of 10 to 20 nm but this behavior is maintained over a large range of period values. The design is more stable but its broadband performance is limited.

- For smaller array periods, the array showcases a large phase shift over a wide wavelength band, however a slight change in spacing can change the resonant behavior drastically. This sensitivity to antenna coupling could pose problems in a real array where, if the array period is fixed, the antennas state can change. If the individual resonances in the antennas are strongly coupled to each other, we can expect a modification in the reflected field if the adjacent antennas are switched which is not a desirable behavior.

We can also visualise the resonance condition clearly in figure 5.16 where the reflectance (in dB to visualise the vanishing amplitude at resonance) is plotted versus wavelength and array

period for four different φ values. We see the "motion" in the p-λ plane of the resonant point : it traces an arc very similar to figure 5.14. If the resonant wavelength of a structure coincides with the operating wavelength (1550 nm) for one of the φ values (say φ_c), then the antenna displays a large phase shift at the operating wavelength. It would mean that the antenna can switch from having its resonant frequency below to above the operating frequency over a full VO_2 transition which naturally creates a phase shift between the cold and hot operating states.

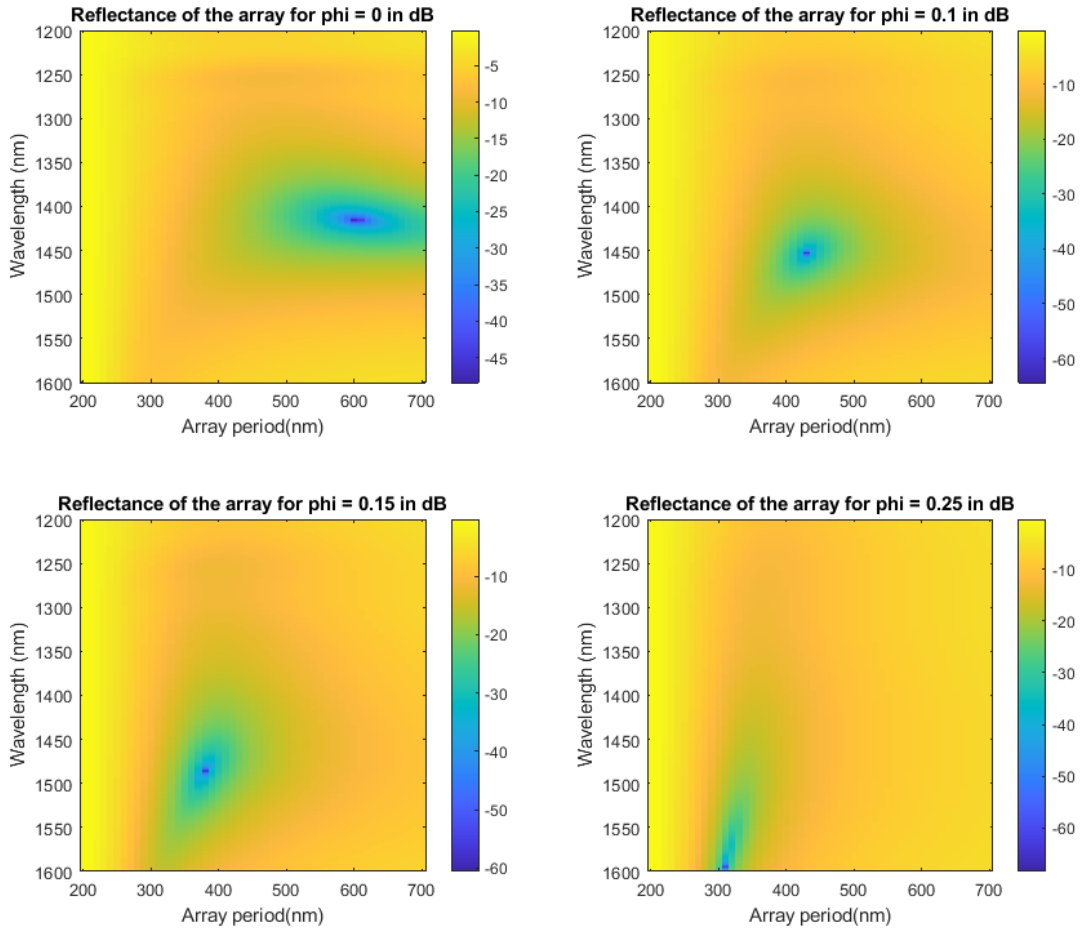

Figure 5.16: Reflectance versus wavelength and array period for four φ values.

5.8 Variations on the design

As mentioned in chapter 4, the algorithm we implemented is very versatile and will adapt to a change in engineering constraints. It is therefore quick to look for other design solutions, that could correspond to other engineering constraints. We can notably change :

- The operating wavelength, the main design was optimised at 1550 nm but some LIDAR manufacturers consider that 905 nm lasers could also be a suitable alternative. We could also develop a metasurface working at visible wavelengths, coincidentally, VO_2 has an extinction coefficient local minima around 600 nm (see figures, 2.4, 2.5) that could prove useful.

- The angle of incidence, this will impact the angular range of the beam steering device where a single anomalous reflection is observed as shown in section 3.1.2.

- The array period, this will impact the beam steering performance as seen in section 3.1.2.

- The SiO_2 thickness, linked to the gold heater thickness by Equation 5.2.

- The VO_2 properties, by conducting simulations with another data set.

- The metallic material, either the backplane, the reflector or the heater material can be modified, using Copper, Aluminium or possibly any other metal that can easily be deposited in thin films

In this section, we still focus on beam steering applications so we leave the figure of merit untouched as defined in equation 5.1 for binary controlled phased arrays. We varied the input parameters in the optimisation process to explore other geometries that would correspond to other engineering choices, results are shown in table 5.5.

- Design [2] is optimised for an incidence angle $\theta_i = 20°$, and a lower periodicity of 400 nm (like Kim et al. [1]) we observe a higher reflectance of 0.277 compared to the original design.

- Design [3] is similar to the main design but at $\lambda = 905$ nm, the overall reflectance is much lower at 0.0537. Manufacturing is expected to be more difficult as the aspect

Design	Original	2	3	4	5	6	7 - copper	8
θ_i	45	20	45	45	0	45	45	0
λ	1550	1550	905	1550	905	1550	1550	1550
p	$\lambda/3$	400	$\lambda/3$	$\lambda/4$	$\lambda/3$	$\lambda/3$	$\lambda/3$	$\lambda/3$
w	245.2	213.2	130.9	233.8	132.0	248.2	247.7	237.4
$t_{Au\ reflector}$	99.4	58	173.4	164.6	138.7	305.9	100.7	59.7
t_{SiO2}	600	600	600	600	600	300	600	600
t_{VO2}	216.3	124.4	133.4	124.6	85.5	195.0	217.1	170.5
$t_{Au\ heater}$	60	60	60	60	60	120	60	60
reflectance	0.216	0.277	0.0537	0.2390	0.1273	0.211	0.214	0.297

Table 5.5: Alternative designs optimisation results.

ratio of the groove between adjacent antennas is much higher and the sensitivity to manufacturing imprecision is expected to scale with the design wavelength.

- Design [4] is similar to the main design but the array period is now $\lambda/4$ which is 387.5 nm since the operating wavelength is 1550 nm. A higher reflectance of up to 23.9% is obtained with this shorter array period.

- Design [5] is optimised for normal incidence at $\lambda = 905$ nm, the reflectance compared to design [3] is much higher up to 12.7%.

- Design [6] has a top Au layer twice as thick as in the main design, which divides the SiO_2 thickness by 2, making it more easily manufacturable in certain cases. The reflectance drops only to 21.1%

- Design [7] is extremely similar to the original design but the material for the backplane is Copper, the change is reflectance is almost imperceptible at 0.214 instead of 0.216

- Design [8] is optimised for normal incidence at $\lambda = 1550\ nm$, the reflectance is much higher at 29.7%.

It can be inferred from these simulation results (and from other less representative attempts we did not show here for conciseness) that a higher reflectance can be obtained with lower array period and/or incidence angles. However, a lower array period means finer features and a higher groove aspect ratio between adjacent antennas, which is harder to manufacture. Similarly, we saw in section 3.1.2 that lower angles of incidence reduce the angular span of the region of interest for beam steering applications. The choices of the array periodicity and angle of incidence are beyond the optical performance indicators as the desired

functionality along with manufacturing and engineering factors must be taken into account. We demonstrate here the power of inverse design in nanophotonics as these results could have taken months of work to obtain with traditional methods while they required no more than a night of simulation on a 2011 medium range desktop.

Chapter 6

Structures for amplitude control

Thanks to the versatility of inverse design algorithms, other geometries can be tested for various applications. In this section, we present other designs optimised for :

- Tunable reflectance : we attempt to maximise the reflectance contrast at a given wavelength between two operating states.
- Colour generation : we are looking for a change in colour with temperature by switching VO_2 based nanoresonators.

6.1 Tunable reflector

Switchable reflectors are very desirable for many applications, they ideally behave like ON-OFF switches for light either at a given wavelength or over a broader wavelength band. The thermal switching of VO_2 could also be used for passive security systems [27]. Several effects can be used to obtain near-perfect absorption and it is possible to engineer a structure so that it behaves like a near-perfect absorber in one state and like a good reflector in the other. The simplest approach to reach perfect absorbance is to use the thin film effect but as we will see, its applications are limited, resonant effects such as those seen (as a side effect) in plasmonics antennas could be optimised to reach high-efficiency tunable absorbance.

6.1.1 Resonant antennas for broadband absorption

We saw in chapter 5 that resonant nanoantennas could have a broadband response for phase control, we also noticed a sharp drop in amplitude at resonance for an intermediate value of φ. If we tune the antenna so that the resonance happens precisely at either $\varphi = 0$ or $\varphi = 1$, then we obtain a resonant structure with high broadband absorbance in one of its states. Using inverse design, we can maximise the absorbance of a given structure over a wavelength

range whilst maximising the reflectance in the other state.

Defining broadband absorption is a problem in itself, what metric are we trying to optimise precisely with the inverse design algorithm? An idea would be to integrate the reflectance spectrum over a given wavelength band, possibly correcting with an illumination factor to calculate the energy reflected by a metasurface in a given state as shown in equation 6.1. The first factor normalises the integral, with $I_{tot} = \int_{\lambda_{min}}^{\lambda_{max}} I(\lambda)d\lambda$, since $R(\lambda) \in [0, 1]$, we have $E_i = 0$ if and only if $R_i(\lambda) = 0 \ \forall\lambda \in [\lambda_{min}, \lambda_{max}]$ and $E_i = 1$ if and only if $R_i(\lambda) = 1 \ \forall\lambda \in [\lambda_{min}, \lambda_{max}]$.

$$E_i = \frac{1}{I_{tot}} \int_{\lambda_{min}}^{\lambda_{max}} R_i(\lambda) I(\lambda) d\lambda \tag{6.1}$$

The broadband reflection contrast can be defined as the difference in energy between two states ($FOM = E_{max} - E_{min}$), the ratio ($FOM = E_{max}/E_{min}$) or with a more complex FOM like in equation 6.2 that combines maximising the absolute difference and the energy ratio between both states. A typical value for α is 0.05, the FOM in that case varies between -1 (no contrast) and -21 (maximum contrast). Using the absolute energy difference may lead to smaller energy ratios : $E_{min} = 0.5$ to $E_{max} = 1$ leads to a better FOM than $E_{min} = 0.0001$ to $E_{max} = 0.5$ even though it is quite clear than the second solution is a far superior absorber. On the other hand, using the amplitude ratio would incentivize the algorithm to look for vanishingly small values of E, that are prone to numerical errors. For example $E_{min} = 10^{-3}$ to $E_{max} = 1$ would lead to a worse FOM than $E_{min} = 10^{-7}$ to $E_{max} = 0.01$ even though the value of $E_{min} = 10^{-7}$ is very sensitive to numerical inaccuracies in the FDTD solver or to manufacturing imprecision. The FOM proposed in equation 6.2 offers an in-between solution that gives satisfactory results.

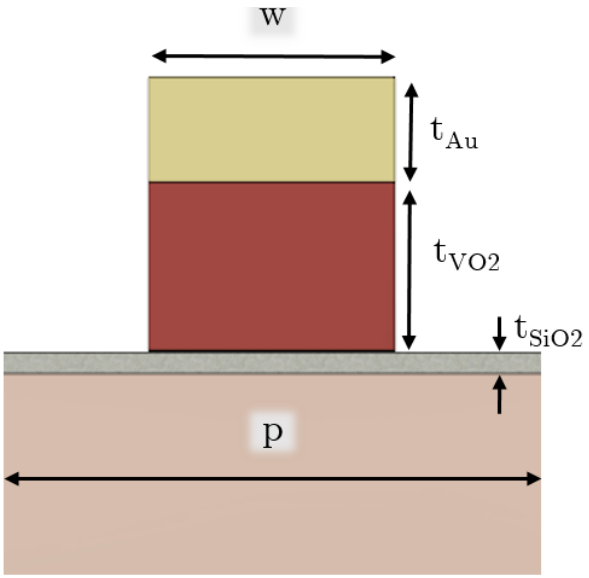

Figure 6.1: Resonant structure for broadband absorption schematic.

$$FOM = -\frac{E_{max} + \alpha}{E_{min} + \alpha} \tag{6.2}$$

We saw in chapter 5 that the resonant MIM structure had broadband phase control capabilities and suffered from a strong decrease in amplitude at resonance. We can use this to our advantage for a tunable reflector application with broadband performance. As such a tunable absorbing metasurface wouldn't require antenna-level control, we can imagine a global array-level thermal control. The thermal insulation layer is not required and the top Au layer does not serve a Joule heating purpose (removing the minimum thickness restriction), we can therefore use the structure shown in figure 6.1. This structure has already been intensively studied, in particular by Kim et al. [1] and showcases the same phase control properties as the structure we proposed in the previous chapter.

We run an optimisation with the top Au layer thickness, the SiO_2 thickness, the VO_2 thickness, the periodicity and the antenna width as parameters. In order to avoid a width greater than the periodicity, we use the width ratio that is in $[\epsilon; 1 - \epsilon]$. The width is then found by multiplying the width ratio by the periodicity, this way we ensure the manufacturability of the array.

A remarkable property of the algorithm is it does not necessarily finds a solution as we expect it, in some cases this leads to a non-physical solution (if the code has a flaw) or sometimes to a new unexpected idea. In this case, the top Au layer was simply removed by the algorithm ($t_{Au} = 0$) and an optimal performance was found with a simple VO_2 stripe on top of a metallic (Au) backplane and a SiO_2 thin film. We ran several optimisations for various wavelength bands with this flexible VO_2 stripe geometry, the results are shown in table 6.1. We analyse them in a later section after we explore alternative structures for tunable reflectance applications.

6.1.2 Thin film effect

Thin film effects arises when a wave is incident a film of thickness $t \sim \lambda_{mat}/4$, with λ_{mat} the wavelength in the film material. Some of the incident wave will be reflected and some will penetrate the film and be reflected at its other end, this secondary reflection will interfere with the initially reflected wave as shown in figure 6.2. This interference can be constructive or destructive, depending on the material index, the film thickness, the angle of incidence and the wavelength. A well-known example of this effect is the iridescence of oil films on a wet

	[1]	[2]	[3]	[4]
λ min [nm]	700	900	1100	1450
λ max [nm]	900	1100	1300	1650
p [nm]	357.2	249.6	364.1	489.5
w [nm]	285.8	173.7	212.0	267.4
t_{SiO_2} [nm]	34.0	42.2	92.3	144.6
t_{VO_2} [nm]	99.3	120.6	94.4	70.2
E_{min}	0.0513	0.00620	0.00123	0.00139
E_{max}	0.418	0.504	0.60539	0.757
FOM	4.616	9.865	12.792	15.507

Table 6.1: Optimisation results for broadband reflectance modulation using a VO_2 patch geometry.

road, the oil being hydrophobic will naturally spread over the water surface, forming a film of dimensions comparable to visible wavelengths. This film being non-uniform in thickness, the destructive and constructive interference will generate variable colours, that also vary with the angle of observation. Several orders of thin film interference can be observed as adding $\lambda_{mat}/2$ to the film thickness will apply a 2π phase shift and thus be imperceptible. Based on the parameters shown in figure 6.2, we derive an analytical model for the thin film effect. First, the optical path difference (red path minus blue path) is :

$$\Delta = n_2(\overline{AB} + \overline{BC}) - n_1(\overline{AD})$$

The paths are then explicitly calculated :

$$\overline{AB} = \overline{BC} = \frac{t}{cos(\theta_r)}$$

$$\overline{AD} = 2t.tan(\theta_r).sin(\theta_1)$$

Using Snell's law, $n_1.sin(\theta_i) = n_2.sin(\theta_r)$, we find :

$$\Delta = 2.n_2.t.cos(\theta_2)$$

This yields constructive interference if $\Delta = m.\lambda$ where $m \in \mathbb{N}$ and destructive interference if $\Delta = (m+0.5).\lambda$. Since we can tune the index n_2 of a VO_2 thin film, we can obtain a tunable absorber, however since VO_2 is a lossy dielectric, there will be absorption even in the ideal case of perfectly constructive interference. We can then calculate the wavelengths for which perfect absorption is achieved in one VO_2 state and perfect reflection in the other by solving

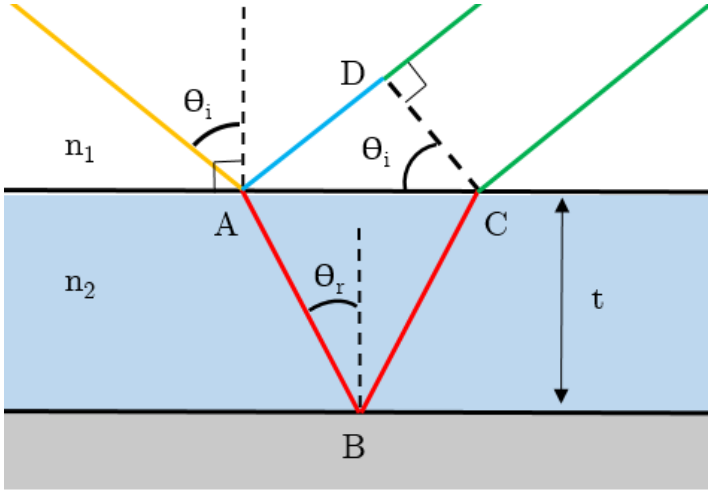

Figure 6.2: Thin film phenomenon schematic with variables.

this system of equations graphically (for normal incidence):

$$\begin{cases} \Delta_0 = 2.n_0.t = m.\lambda \\ \Delta_1 = 2.n_1.t = (m + 0.5).\lambda \end{cases}$$

This system corresponds to constructive interference in the cold state ($\varphi = 0$) and destructive thin film interference in the hot state, we could similarly choose the opposite configuration without any loss of generality. We plot the index difference $\Delta n = n_0 - n_1$ versus wavelength along with the ideal interference lines defined by $y = n_1(\lambda)/2m$, $m \in \mathbb{N}$: the points where the index difference curve intersects one of the ideal interference line corresponds to one such configuration. The results are shown for $\lambda \in [400 - 1600]$ nm in Figure 6.3, we can calculate the VO_2 thickness that would yield such a configuration with $t = \dfrac{m.\lambda}{2.n_1}$. For our VO_2 material properties, we calculate $t_1 = 243$ nm at $\lambda = 845$ nm, $t_2 = 319$ nm at $\lambda = 675$ nm, $t_3 = 370$ nm at $\lambda = 586$ nm and $t_4 = 383$ nm at $\lambda = 497$ nm these high thickness values are problematic as such VO_2 thicknesses would simply absorb the incident field.

We see in Figure 6.4 the perfect thin film interference points and the penetration depth in VO_2 in both hot and cold state. The penetration depth δ_p is defined as the depth where the field has decreased to 1/e of its value ($1/e^2$ of its intensity) and is calculated as :

$$\delta_p(\lambda) = \frac{\lambda}{2\pi.k_{mat}(\lambda)} \tag{6.3}$$

where $k_{mat}(\lambda)$ is the extinction coefficient of the material at a given wavelength. We see that each perfect interference point up to order 4 are above the penetration depth in hot

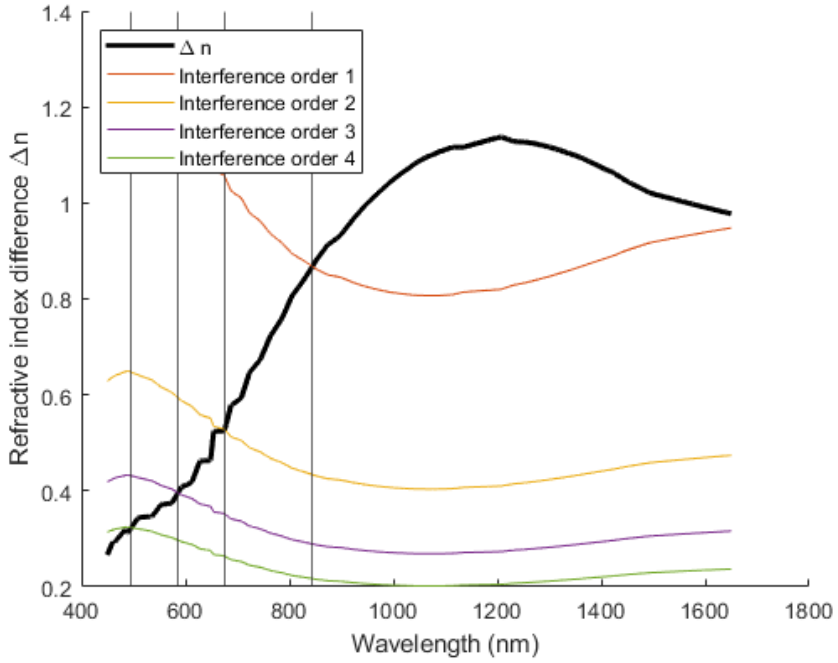

Figure 6.3: Perfect thin film interference conditions for VO_2.

VO_2 and not far from the penetration depth in cold VO_2, which means the reflected field at the gold interface has a very low amplitude. Since this reflection has to go through the VO_2 layer again before interfering with the directly reflected field, we can expect a very weak interference phenomenon.

6.1.3 Thin film structure for tunable reflectance

Since perfect thin-film interference is not achievable realistically using VO_2, we modify the structure and add a thin insulating SiO_2 layer, the resultant structure is a thin VO_2 film on top of a thin SiO_2 layer deposited on an optically thick metallic (Au) backplane. Since only the VO_2 and SiO_2 thickness can be tuned, we decide to use a double parameter sweep to find a thin film configuration that yields a high reflectance contrast. The major advantage to simulate such 1D structures is that the FDTD method is not required : it can be solved extremely quickly using the analytic transfer matrix method. This algorithm is implemented by default on Lumerical FDTD with the method $stackrt(n, d, f)$ [88]. This reduces simulation time drastically and thus allows to obtain high precision parameter maps that are useful to understand the phenomenons at stake. We first evaluate the performance of

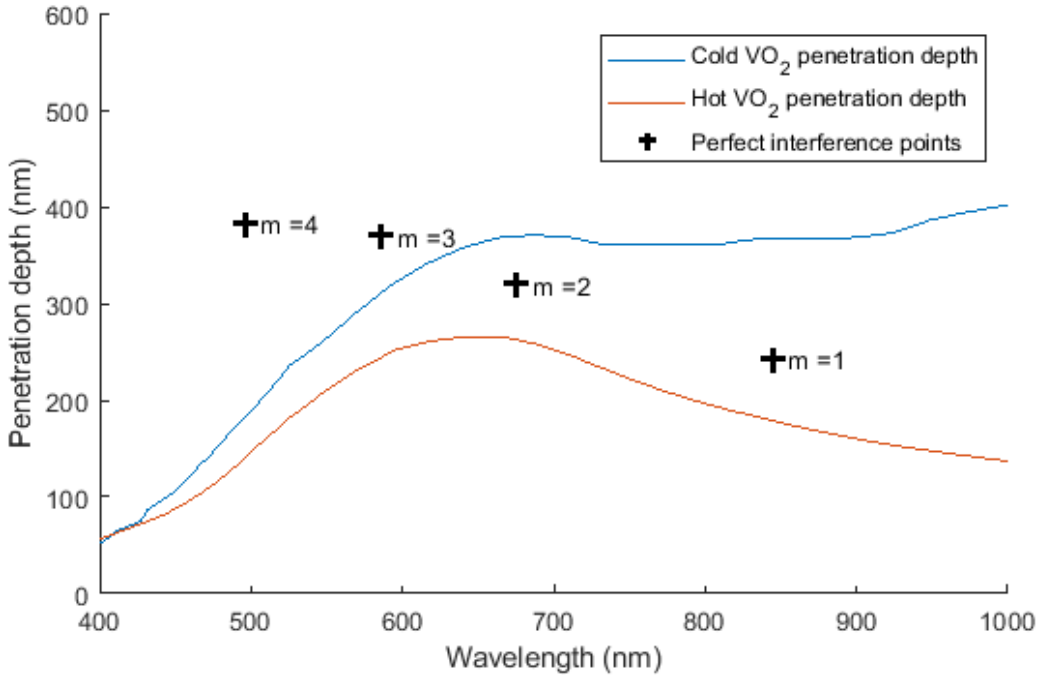

Figure 6.4: Penetration depth versus wavelength with perfect thin film interference conditions for VO_2.

the reflectance modulation using the FOM defined in equation 6.2 (in the case of a single wavelength optimisation, the E_i values simplify down to the reflectance in state i).

We perform narrowband simulations over several bands, we vary the VO_2 between 10 and 100 nm and SiO_2 between 10 and 400 nm. The figure of merit is shown for 9 simulation bands in figure 6.5, the bands are defined by their central wavelength (see titles of figure 6.5) and have a 2 nm width ($\lambda \in [\lambda_0 - 1\ nm; \lambda_0 + 1\ nm]$). We find very high figures of merit of up to 16.4 at 1500 nm, this is close to the maximum value of 21 (perfect ON/OFF contrast). We see in figure 6.5 that the set of film thickness that corresponds to a high FOM is non-trivial at short wavelengths, it becomes more "predictable" in the NIR.

We notice that the absorption modulation properties in this stack geometry are already rather broadband, we therefore try to characterise this reflectance modulation and even optimise this structure for broadband reflectance tuning. This time using a band with 200 nm width ($\lambda \in [\lambda_0 - 100\ nm; \lambda_0 + 100\ nm]$), we obtain a similar FOM map than with the narrowband optimisation. We plot in figure 6.6 the optimum parameters for narrowband and broadband tunable reflectance. The optimal parameters are sensibly the same for broadband

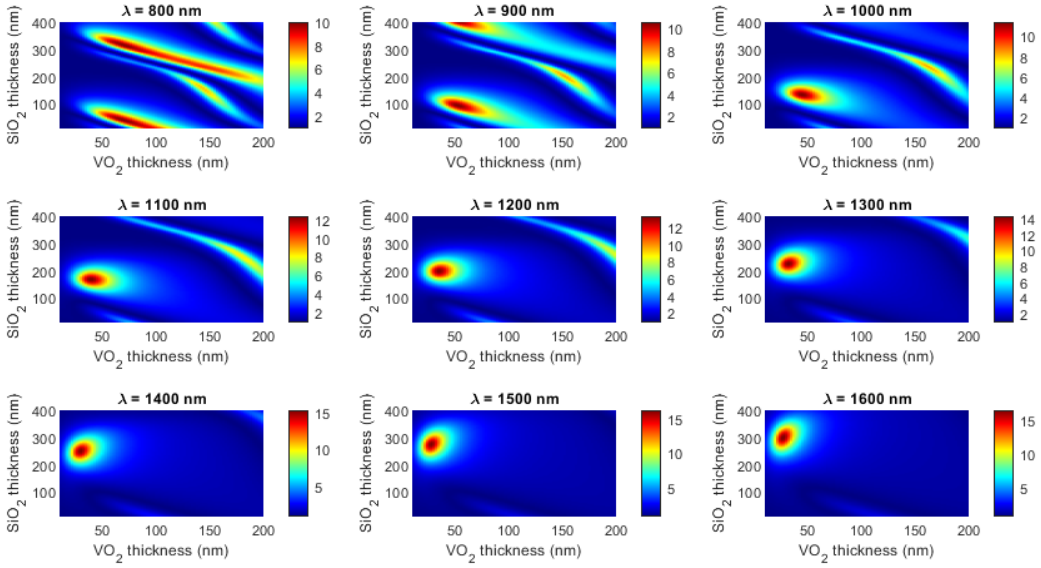

Figure 6.5: Figure of merit over a VO_2 and SiO_2 sweep for several simulation bands.

and narrowband tunable reflectance, the structure is not specifically optimised for broadband performance but is by nature well suited for this purpose.

We remark that the maximum achievable FOM increases with the simulation central wavelength, this is clearly seen in figure 6.7. We conjecture that this phenomenon is due to the higher the n-index contrast with higher wavelengths : the k-value itself matters less as a resonant structure is lossy by nature. A high n-contrast (achieved at longer wavelengths, typically in the infrared) allows the structure to work just right at the resonance frequency in one state and further away from the resonance condition in the other state. As the resonance is broadband, a high n-index modulation is required to displace the operating state far from resonance and avoid high losses in the highly reflective state.

Since we obtain a reasonably high figure of merit using such a simple structure as a two-layers thin film stack, we have to compare it to the more complex resonant structure designed previously in this section. The results shown in figure 6.7 indicate that higher performance can be reached by structuring the VO_2 film for broadband applications, although this increase is not as substantial as one may expect given the extra manufacturing complexity to obtain a grating structured VO_2 film. We also verify that, as expected, the narrowband performance for tunable contrast is significantly better than the broadband performance.
The behaviour of a given structure is shown in figure 6.8, the thin film structure used is optimal for $\lambda = 1550\ nm$, has a VO_2 thickness of 26 nm and a SiO_2 thickness of 286 nm.

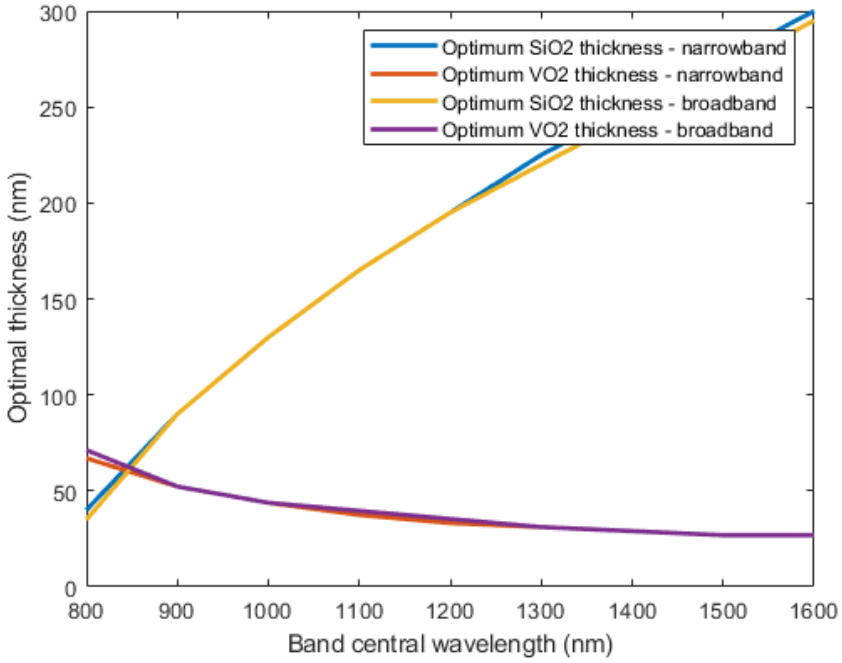

Figure 6.6: Ideal VO_2 and SiO_2 thickness for the stack structure for narrowband and broadband tunable reflectance optimisation.

Narrowband simulations were used to obtain this figure in order to reduce material properties interpolation errors with Lumerical. We can see that if the reflectance of the structure changes with the wavelength, it only changes with the VO_2 phase in the near-infrared. Near-perfect absorption is achieved with the metallic VO_2 phase with excellent reflectivity above 80% with fully dielectric VO_2 as shown in figure 6.9.

Although these results are purely simulation-based, they are promising as they improve on previously reported performance. Ko et al. [89] found a change in absorption of around 30% between 800–1600 nm with a similar structure. Using two degrees of freedom (SiO_2 and VO_2 thickness) instead of one (only the SiO_2 thickness) allows the structure to exhibit enhanced performance. Furthermore, the proposed thin film structure is rather simple and even though it can be outperformed by other structures [90] over a narrow bandwidth (98% reflectance modulation using Sb_2S_3), it has broadband properties that cannot be ignored. Vanadium dioxide is also a safer alternative and its IMT is easily triggered by a range of phenomenons as seen in section 2.2.2 making this solution very practical. Other types of resonators can be investigated in future work to provide higher performance or a better control of the resonant wavelength. Similar resonant metasurfaces could also be developed for other wavelength, inverse design may help improving on previous work in the terahertz regime [91].

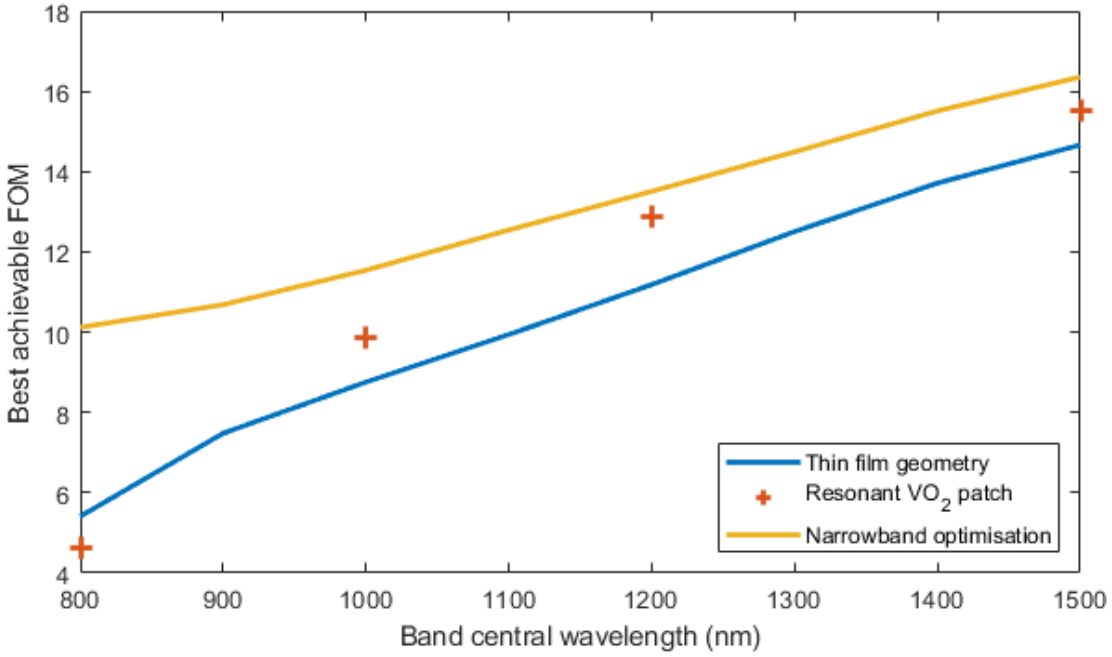

Figure 6.7: Highest achievable FOM versus wavelength for a thin film structure and the VO_2 patch structure for broadband tunable reflection ($\Delta\lambda = 200\ nm$) compared to the thin film structure maximum achievable narrowband performance.

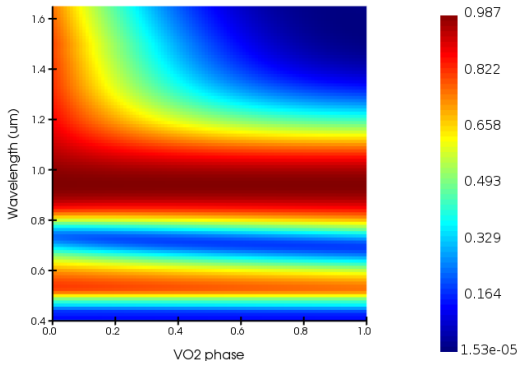

Figure 6.8: Thin film structure reflectance versus wavelength and VO_2 composition, the x-axis is the metallic fraction of VO_2 for partial transitions.

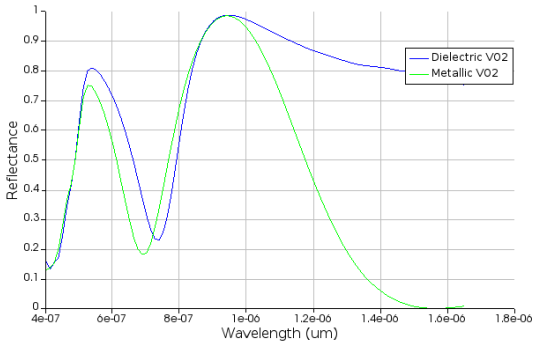

Figure 6.9: Reflectance of a thin film structure with $t_{VO2} = 26\ nm$ and $t_{SiO2} = 286\ nm$ in the hot and cold state.

6.2 Color generation

6.2.1 Color generation theory

The characterisation of colours as perceived by the human eye has been investigated along with the popularisation of RGB displays in colour screens. The eye gamut (set of all colours perceived by the human eye) has been characterised extensively and normalised with the CIE standards ("Commission internationale de l'éclairage" or "international commission on illumination"). The human eye perceives colour through a set of three cone cells that are sensitive to different wavelengths as shown in figure 6.11. A given illumination will stimulate the three cones at a given intensity, each colour can therefore be described as a linear combination of the stimulation of those three cones. The CIE 1931 standard describes a colour using a 3-d vector in a "color space" called XYZ for convenience, the X, Y and Z value are called the "tristimulus values". Their interpretation is the following : Y is the luminance, Z is quasi-equal to blue (of CIE RGB), and X is a mix of the three CIE RGB curves chosen to be nonnegative. Setting Y as luminance has the useful result that for any given Y value, the XZ plane will contain all possible chromaticities at that luminance. The XYZ values are calculated using equation 6.4 where $L(\lambda)$ is the spectral radiance of the object.

$$\begin{aligned} X &= \int_{lambda} L(\lambda).\tilde{x}(\lambda).d\lambda \\ Y &= \int_{lambda} L(\lambda).\tilde{y}(\lambda).d\lambda \\ Z &= \int_{lambda} L(\lambda).\tilde{z}(\lambda).d\lambda \end{aligned} \tag{6.4}$$

The $\tilde{x}, \tilde{y}, \tilde{z}$ functions defined in equation 6.5 are a sum of piece-wise Gaussian functions (defined in equation 6.6) : they characterise the CIE 1931 colour space that is still widely used nowadays.

$$\begin{aligned} \tilde{x}(\lambda) &= 1.056.g(\lambda; 599.8, 37.9, 31.0) + 0.632.g(\lambda; 442.0, 16.0, 26.7) \\ \tilde{y}(\lambda) &= 0.821.g(\lambda; 568.8, 46.9, 40.5) + 0.286.g(\lambda; 530.9, 16.3, 31.1) \\ \tilde{z}(\lambda) &= 1.217.g(\lambda; 437.0, 11.8, 36.0) + 0.681.g(\lambda; 459.0, 26.0, 13.8) \end{aligned} \tag{6.5}$$

$$\begin{aligned} g(x;\mu,\sigma_1,\sigma_2) &= exp(-0.5(x-\mu)^2/\sigma_1^2),\ x<\mu \\ &= exp(-0.5(x-\mu)^2/\sigma_2^2),\ x>\mu \end{aligned} \tag{6.6}$$

It is possible to go from the [XYZ] tristimulus space to the [RGB] colour space and vice versa, using linear algebra as shown in equation 6.7. The 1931 CIE standard only specifies the matrix used to convert [RGB] data to [XYZ] but the inverse can easily be computed, it is however preferable to avoid multiple conversions to limit round-trip errors. The CIE standard therefore only exactly specifies a single conversion matrix, its inverse would only be precise to several decimal places.

$$\begin{bmatrix} X \\ Y \\ Z \end{bmatrix} = \begin{bmatrix} 0.49000 & 0.31000 & 0.20000 \\ 0.17697 & 0.81240 & 0.01063 \\ 0.00000 & 0.01000 & 0.99000 \end{bmatrix} \cdot \begin{bmatrix} R \\ G \\ B \end{bmatrix} \tag{6.7}$$

This gamut was specifically created so that the Y value corresponds to the luminance of the color. The chromaticity can then be derived from the two normalised parameters x and y, derived from the XYZ values using equation 6.8. The xyY triplet is often used as a colour space can be represented using xy coordinates on a "chromaticity diagram" for a fixed Y (luminance) value.

$$x = \frac{X}{X+Y+Z} \quad y = \frac{Y}{X+Y+Z} \tag{6.8}$$

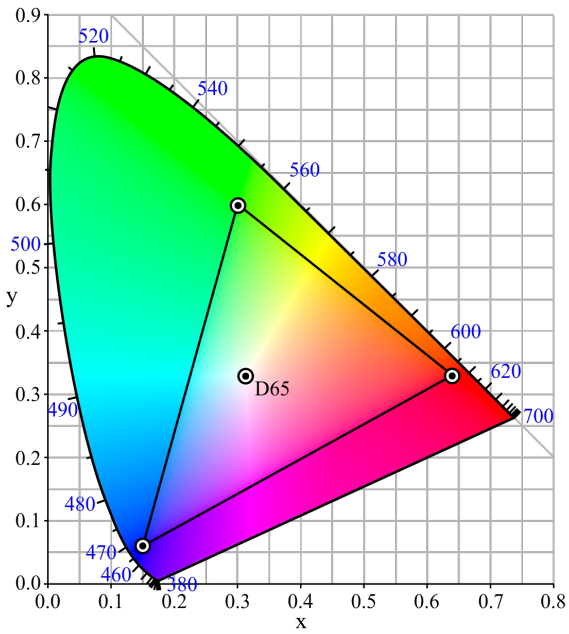

Figure 6.10: CIE 1931 gamut with standard RGB color space

This CIE standard allows us to predict a colour from a reflectance spectrum using a given illumination spectrum, we will use the natural sun illumination spectrum approximated as a blackbody. This illumination spectrum ignores all the atmospheric absorption bands but it does not drastically change the colour, the variable $L(\lambda)$ in equation 6.4 is calculated from the reflectance spectrum $R(\lambda)$ using equation

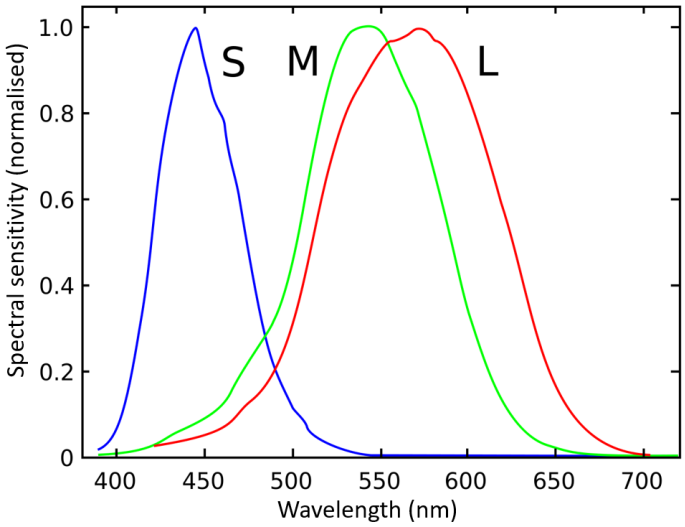

Figure 6.11: Spectral sensitivity to light versus wavelength of human cones of S, M and L (short, medium and long) types. Picture from User:Vanessaezekowitz.

6.9 with $T_{sun} = 5778$ K.

$$L(\lambda) = R(\lambda).I(\lambda) \quad I(\lambda) = \frac{8.\pi.h.c^2}{\lambda^5.\left(e^{\frac{h.c}{\lambda.k.T_{sun}}} - 1\right)} \tag{6.9}$$

One last note regarding the conversion of a given reflectance spectrum to an RGB triplet : sometimes the color cannot be represented in the rgb space at all. The entire gamut in figure 6.10 is not covered by the rgb color space that only spans over the black triangle. Therefore, it one wants to have a representation in the rgb space that is close enough to the real color, we need to normalise the calculated rgb values. If one of the rgb triplet value is negative, we apply the following operation : $rgb = rgb - min(rgb)$, this corresponds to adding a neutral gray scale. Then, in order to eliminate high values (larger than 1), we apply $rgb = rgb/max(rgb)$. This normalisation process is arbitrary but it is simple enough and therefore a good choice to "convert" xyY data in the rgb color space. This is a lossy process and reverting it will not produce the original color in the xyY space. The color resulting from this normalisation process will be saturated in brightness as at least one of the RGB coefficient will be equal to 1, it is therefore not possible to increase its intensity without changing the hue.

6.2.2 Color generation structure

Thanks to the 1931 CIE color space, we find a bridge between what seems to be a qualitative assessment and a set of quantitative values from which it is possible to draw a figure of merit. From there, we can try to maximise the distance in the colour space between the two operating states of the structure or any other figure of merit that seems appropriate to achieve colour modulation. Several plasmonic structures have been proposed for dynamic colour change [92–94] aka broadband reflectance modulation in the visible domain. A simple thin VO_2 film on top of a metallic substrate like gold is sufficient to achieve colour change, we show in figure 6.13 the colour changes achieved by thin films of thicknesses comprised between 10 and 200 nm. In figure 6.12, we show how the VO_2 thickness modulates the colour but also how it can be changed by changing the VO_2 composition. The colours have a maximum brightness due to the rgb normalisation process (necessary to represent the colours on a rgb screen or print the graph), a real VO_2 thin film is not necessarily as vivid as shown in figure 6.12.

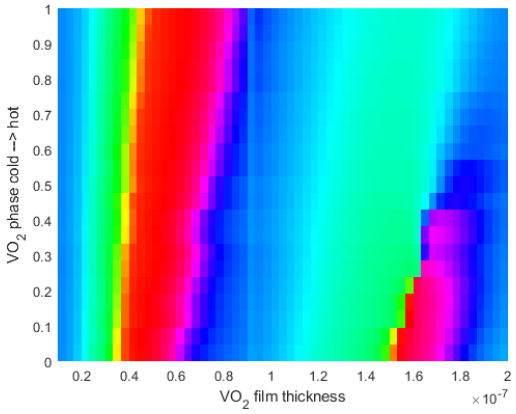

Figure 6.12: VO_2 thin film colour change achieved for a range of film thickness and a progressive transition of the VO_2 phase.

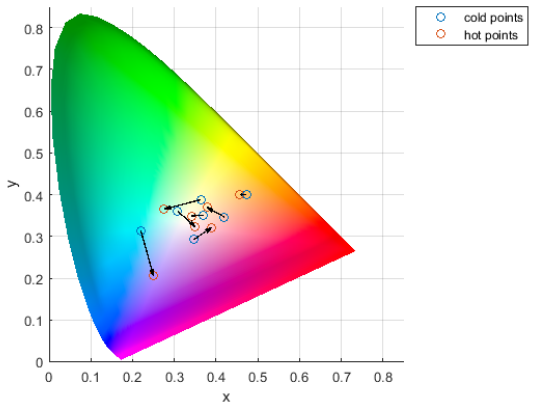

Figure 6.13: VO_2 thin film colour change achieved for various film thickness represented on the CIE 1931 gamut.

Other studies have shown colour change using resonators [92], some where the tuning mechanism is based on Vanadium dioxide, notably [93] that proposed silver nanoresonators where the resonance is tuned in the vicinity of a VO_2 film. The thin film structure proposed here achieves similar results but is simpler to manufacture and is easily tunable by using the appropriate film thickness for a given colour change.

Chapter 7

Conclusion and future work

Tunable resonant nanoantennas are a promising technology to achieve reconfigurable metasurfaces in the optical and NIR domains for LIDAR or optical communication applications. Several materials have been proposed and tested to achieve tunability with nano-scale elements, among them, Vanadium dioxide is one of the most promising. The wide index modulation achieved at transition, the possibility to engineer its micro-structure to tune the transition properties and the simplicity to trigger it make VO_2 an exceptional material in nanophotonics. We saw however that all resonant nanoantennas suffer from several flaws, all intrinsically linked to their resonant nature. These flaws are namely a non-2π phase shift, a high non-linearity between input modulation and output phase angle and most importantly a high amplitude-phase correlation. Since it is not possible to simultaneously solve all these issues, an alternative idea to bypass them is proposed : binary controlled phased arrays.
Instead of continuously tuning the phase of each antenna to achieve perfectly constructive interference at the anomalous reflection angle, we realise that only partially constructive interference are sufficient to achieve beam steering at the cost of a decrease in peak amplitude. We therefore choose to discretise the output phase and only use two operating states for each antenna (OFF/ON) with output phase angle of respectively 0 and 180°, this results in an amplitude decrease of about 60% compared to the ideal case but solves all the aforementioned challenges whilst drastically simplifying the operation of the nano phased array. The full 2π range is indeed covered by only two states, control is simplified to the extreme with only 1-bit of information necessary per antenna and it is possible to design the antenna so that the reflectance in both states is perfectly equal. Instead of very imperfectly implementing a perfect control algorithm, we perfectly implement an imperfect one.
A novel structure was then proposed, improving on a previously studied metal-insulator-metal

structure, we added a thermal insulation layer to limit thermal crosstalk between adjacent antennas. A thorough thermal analysis of the structure at the antenna and the array scale was conducted to design a realistic device where each antenna can be individually switched using Joule heating. Inverse design was then used to optimise the MIM structure for binary control using a combination of the particle swarm algorithm and the interior point algorithm. The resulting structure achieved a reflectance of 21.6% with a perfect π phase shift between both states, direct simulations of a full array show an excellent match with the analytical calculations from first principles. Exploiting the versatility of the structure and the inverse design algorithm, other geometries corresponding to different engineering constraints were proposed. We show that this structure can be adapted to other operating wavelengths and allows a range of array periods, materials and angles of incidence.

As seen in the literature and in this work, resonant structures showcase a large drop in reflectance, if this effect is an issue for beam steering applications, it can be exploited to achieve tunable reflectance. The antenna design developed for phase control applications was adapted by removing the thermal insulation layer and optimised to achieve a high reflectance contrast between its two operating states. An excellent broadband performance was achieved, for several wavelength bands, for example, we obtain R_0=0.00139 and $R_1 = 0.757$ for $\lambda \in [1450 - 1650\ nm]$. This structure is then compared to a simple stack structure composed of a VO_2 film and a SiO_2 film on top of an optically thick metallic backplane. If this structure showcased a slight drop in performance compared to the resonant VO_2 patch structure, the reduction in manufacturing complexity could make up for the loss in performance in some applications. Furthermore, this thin film structure displays excellent performance in colour generation applications where the reflectance spectrum in the visible domain is widely modified as the VO_2 film transitions.

During this project, a number of ideas that could potentially improve on this work have been raised but not explored in depth for various reasons. Most analytical derivations have been presented in 1D but can easily be extended to 2D metasurfaces even though the structure presented here cannot be directly extended to form a 2D phased array. The electrical contacts required for Joule heating would be much more complex to manufacture if the antenna structure was not a stripe but a column.

One can also note that we have only considered a structurally periodic (with uniform antenna spacing) phased array with uniform illumination (all the antennas are subjected to the

same incident field amplitude), this kind of device is not known for its optimal performance. Structurally aperiodic arrays tend to perform better in practice [16, 95] and amplitude tapering is also very useful to reduce side-lobes drastically. We did not extend the analysis to these special phased arrays to keep the analysis as reproducible and general as possible but performance in applications can be further improved using these concepts. While structural aperiodicity may prove be more taxing to achieve, as changing the gap between adjacent antennas may influence their response, amplitude tapering is almost guaranteed as the illumination from a laser source has a non-constant beam amplitude profile by nature.

A higher thermal contrast could also be implemented in a 2D phased array to enable multiplexing, carefully taking advantage of the thermal inertia of the device. Given the exceptional broadband properties of this structure, it is also possible to use multiple laser inputs to increase the scanning rate. They could be separated angularly in the steering direction to scan several points on the same line or orthogonally to it to scan several lines simultaneously. We note that this remarkable broadband resonance is directly linked to an excellent robustness to manufacturing inaccuracies, small deviations from the prescribed design will not result in a loss in performance.

Array-level inverse design could also be implemented to improve on the binary control algorithm with a possibility to enhance user-defined properties of the far-field [96]. Finally, the simple inverse design algorithm exploited to tune the antenna parameters could be used with another set of engineering constraints or FOM to get a different functionality as we showed in section 5.8.

Finally, binary control can be applied without any loss of generality to any phased array regardless of the mechanism used to tune the output phase. For example, this approach can be applied to phased arrays using other PCMs or external phase shifters at any wavelength and scale. If binary control is particularly well suited to solve the problems posed by resonant antennas, the extreme simplification it offers could make binary controlled phased arrays excellent candidates for low-cost RADARs.

Other structures offering a higher reflectance could be investigated in the future as a reflectance of just 21.6% leaves a lot of space for improvements. A way to achieve this would be reducing the quantity of VO_2 in the antenna, this could however lead to more manufacturing challenges. Similarly, improving the quality factor of the resonance could help enhancing the reflectance in both states but it could be at the expense of the stability of the structure's

performance with regard to manufacturing inaccuracy. Given the improvements that binary control allows for nano-resonator phased arrays, it is expected that not only VO_2 based structures would benefit from this novel control algorithm but also all structures using ITO, GST or graphene as resonance modulators. Resonant phased arrays could then outperform external phase shifters phased arrays, especially regarding power consumption, simplicity of control, footprint and manufacturing cost.

Bibliography

[1] Yonghwi Kim, Pin Chieh Wu, Ruzan Sokhoyan, Kelly Mauser, Rebecca Glaudell, Ghazaleh Kafaie Shirmanesh, and Harry A. Atwater. Phase Modulation with Electrically Tunable Vanadium Dioxide Phase-Change Metasurfaces. *Nano Letters*, 19(6):3961–3968, June 2019. ISSN 1530-6984. doi: 10.1021/acs.nanolett.9b01246. URL https://doi.org/10.1021/acs.nanolett.9b01246.

[2] Ali Forouzmand and Hossein Mosallaei. Dynamic beam control via Mie-resonance based phase-change metasurface: a theoretical investigation. *Optics Express*, 26(14):17948–17963, July 2018. ISSN 1094-4087. doi: 10.1364/OE.26.017948. URL https://opg.optica.org/oe/abstract.cfm?uri=oe-26-14-17948.

[3] Junghyun Park, Ju-Hyung Kang, Soo Jin Kim, Xiaoge Liu, and Mark L. Brongersma. Dynamic Reflection Phase and Polarization Control in Metasurfaces. *Nano Letters*, 17(1):407–413, January 2017. ISSN 1530-6984. doi: 10.1021/acs.nanolett.6b04378. URL https://doi.org/10.1021/acs.nanolett.6b04378.

[4] Ziqi Miao, Qiong Wu, Xin Li, Qiong He, Kun Ding, Zhenghua An, Yuanbo Zhang, and Lei Zhou. Widely Tunable Terahertz Phase Modulation with Gate-Controlled Graphene Metasurfaces. *Physical Review X*, 5(4):041027, November 2015. doi: 10.1103/PhysRevX.5.041027. URL https://link.aps.org/doi/10.1103/PhysRevX.5.041027.

[5] Michelle C. Sherrott, Philip W. C. Hon, Katherine T. Fountaine, Juan C. Garcia, Samuel M. Ponti, Victor W. Brar, Luke A. Sweatlock, and Harry A. Atwater. Experimental Demonstration of \textgreater230° Phase Modulation in Gate-Tunable Graphene–Gold Reconfigurable Mid-Infrared Metasurfaces. *Nano Letters*, 17(5):3027–3034, May 2017. ISSN 1530-6984. doi: 10.1021/acs.nanolett.7b00359. URL https://doi.org/10.1021/acs.nanolett.7b00359.

[6] Mohammed Reza M. Hashemi, Shang-Hua Yang, Tongyu Wang, Nelson Sepúlveda, and Mona Jarrahi. Electronically-Controlled Beam-Steering through Vanadium Dioxide Metasurfaces. *Scientific Reports*, 6(1):35439, October 2016. ISSN 2045-2322. doi: 10.1038/srep35439. URL https://www.nature.com/articles/srep35439.

[7] Yonghwi Kim. *Light Modulation with Vanadium Dioxide-Based Optical Devices*. phd, California Institute of Technology, 2022. URL https://resolver.caltech.edu/CaltechTHESIS:06232021-050358035.

[8] Matthieu Proffit, Sara Pelivani, Pascal Landais, and A. Louise Bradley. Electrically Driven Reprogrammable Vanadium Dioxide Metasurface Using Binary Control for Broadband Beam Steering. *ACS Applied Materials & Interfaces*, September 2022. ISSN 1944-8244. doi: 10.1021/acsami.2c10194. URL https://doi.org/10.1021/acsami.2c10194. Publisher: American Chemical Society.

[9] Maria Carolina Viganó. CAPABILITIES OF ARRAY ANTENNA WITH 1 BIT PHASE CONTROLS FOR MOBILE SATCOM TERMINAL APPLICATIONS. page 5.

[10] Adolf Prasch. *Die fortschritte auf dem gebiete der drahtlosen telegraphie ...* F. Enke., 1905.

[11] R.J. Mailloux. Phased array theory and technology. *Proceedings of the IEEE*, 70(3):246–291, March 1982. ISSN 1558-2256. doi: 10.1109/PROC.1982.12285.

[12] Nanfang Yu, Patrice Genevet, Mikhail A. Kats, Francesco Aieta, Jean-Philippe Tetienne, Federico Capasso, and Zeno Gaburro. Light Propagation with Phase Discontinuities: Generalized Laws of Reflection and Refraction. *Science*, 334(6054):333–337, October 2011. doi: 10.1126/science.1210713. URL https://www.science.org/doi/10.1126/science.1210713.

[13] Ching-Pai Hsu, Boda Li, Braulio Solano-Rivas, Amar R. Gohil, Pak Hung Chan, Andrew D. Moore, and Valentina Donzella. A Review and Perspective on Optical Phased Array for Automotive LiDAR. *IEEE Journal of Selected Topics in Quantum Electronics*, 27(1):1–16, January 2021. ISSN 1558-4542. doi: 10.1109/JSTQE.2020.3022948.

[14] Jingwen He, Tao Dong, and Yue Xu. Review of Photonic Integrated Optical Phased Arrays for Space Optical Communication. *IEEE Access*, 8:188284–188298, 2020. ISSN 2169-3536. doi: 10.1109/ACCESS.2020.3030627.

[15] David N. Hutchison, Jie Sun, Jonathan K. Doylend, Ranjeet Kumar, John Heck, Woosung Kim, Christopher T. Phare, Avi Feshali, and Haisheng Rong. High-resolution aliasing-free optical beam steering. *Optica*, 3(8):887–890, August 2016. ISSN 2334-2536. doi: 10.1364/OPTICA.3.000887. URL https://opg.optica.org/optica/abstract.cfm?uri=optica-3-8-887.

[16] Min Chul Shin, Aseema Mohanty, Kyle Watson, Gaurang R. Bhatt, Christopher T. Phare, Steven A. Miller, Moshe Zadka, Brian S. Lee, Xingchen Ji, Ipshita Datta, and Michal Lipson. Chip-scale blue light phased array. *Optics Letters*, 45(7):1934–1937, April 2020. ISSN 1539-4794. doi: 10.1364/OL.385201. URL https://opg.optica.org/ol/abstract.cfm?uri=ol-45-7-1934.

[17] David Kwong, Amir Hosseini, John Covey, Yang Zhang, Xiaochuan Xu, Harish Subbaraman, and Ray T. Chen. On-chip silicon optical phased array for two-dimensional beam steering. *Optics Letters*, 39(4):941–944, February 2014. ISSN 1539-4794. doi: 10.1364/OL.39.000941. URL https://opg.optica.org/ol/abstract.cfm?uri=ol-39-4-941.

[18] J. Komma, C. Schwarz, G. Hofmann, D. Heinert, and R. Nawrodt. Thermo-optic coefficient of silicon at 1550 nm and cryogenic temperatures. *Applied Physics Letters*, 101(4):041905, July 2012. ISSN 0003-6951. doi: 10.1063/1.4738989. URL https://aip.scitation.org/doi/10.1063/1.4738989.

[19] Martijn J. R. Heck. Highly integrated optical phased arrays: photonic integrated circuits for optical beam shaping and beam steering. *Nanophotonics*, 6(1):93–107, January 2017. ISSN 2192-8614. doi: 10.1515/nanoph-2015-0152. URL https://www.degruyter.com/document/doi/10.1515/nanoph-2015-0152/html.

[20] Huaqing Qiu, Yong Liu, Chao Luan, Deming Kong, Xiaowei Guan, Yunhong Ding, and Hao Hu. Energy-efficient thermo-optic silicon phase shifter with well-balanced overall performance. *Optics Letters*, 45(17):4806, September 2020. ISSN 0146-9592, 1539-4794. doi: 10.1364/OL.400230. URL https://opg.optica.org/abstract.cfm?URI=ol-45-17-4806.

[21] Tin Komljenovic and Paolo Pintus. On-chip calibration and control of optical phased arrays. *Optics Express*, 26(3):3199–3210, February 2018. ISSN 1094-4087. doi: 10.1364/OE.26.003199. URL https://opg.optica.org/oe/abstract.cfm?uri=oe-26-3-3199.

[22] Ali Forouzmand and Hossein Mosallaei. Electro-optical Amplitude and Phase Modulators Based on Tunable Guided-Mode Resonance Effect. *ACS Photonics*, 6(11):2860–2869, November 2019. doi: 10.1021/acsphotonics.9b00950. URL https://doi.org/10.1021/acsphotonics.9b00950.

[23] Ghazaleh Kafaie Shirmanesh, Ruzan Sokhoyan, Pin Chieh Wu, and Harry A. Atwater. Electro-optically Tunable Multifunctional Metasurfaces. *ACS Nano*, 14(6):6912–6920, June 2020. ISSN 1936-0851. doi: 10.1021/acsnano.0c01269. URL https://doi.org/10.1021/acsnano.0c01269.

[24] Sajjad Abdollahramezani, Omid Hemmatyar, Mohammad Taghinejad, Hossein Taghinejad, Alex Krasnok, Ali A. Eftekhar, Christian Teichrib, Sanchit Deshmukh, Mostafa A. El-Sayed, Eric Pop, Matthias Wuttig, Andrea Alù, Wenshan Cai, and Ali Adibi. Electrically driven reprogrammable phase-change metasurface reaching 80% efficiency. *Nature Communications*, 13(1):1696, March 2022. ISSN 2041-1723. doi: 10.1038/s41467-022-29374-6. URL https://www.nature.com/articles/s41467-022-29374-6.

[25] Yiguo Chen, Xiong Li, Yannick Sonnefraud, Antonio I. Fernández-Domínguez, Xiangang Luo, Minghui Hong, and Stefan A. Maier. Engineering the Phase Front of Light with Phase-Change Material Based Planar lenses. *Scientific Reports*, 5(1):8660, March 2015. ISSN 2045-2322. doi: 10.1038/srep08660. URL https://www.nature.com/articles/srep08660.

[26] H.-S. Philip Wong, Simone Raoux, SangBum Kim, Jiale Liang, John P. Reifenberg, Bipin Rajendran, Mehdi Asheghi, and Kenneth E. Goodson. Phase Change Memory. *Proceedings of the IEEE*, 98(12): 2201–2227, December 2010. ISSN 1558-2256. doi: 10.1109/JPROC.2010.2070050. Conference Name: Proceedings of the IEEE.

[27] Andrew Sarangan, Josh Duran, Vladimir Vasilyev, Nicholaos Limberopoulos, Ilya Vitebskiy, and Igor Anisimov. Broadband Reflective Optical Limiter Using GST Phase Change Material. *IEEE Photonics Journal*, 10(2):1–9, April 2018. ISSN 1943-0655. doi: 10.1109/JPHOT.2018.2796448.

[28] Carlota Ruiz de Galarreta, Arseny M. Alexeev, Yat-Yin Au, Martin Lopez-Garcia, Maciej Klemm, Martin Cryan, Jacopo Bertolotti, and C. David Wright. Nonvolatile Reconfigurable Phase-Change Metadevices for Beam Steering in the Near Infrared. *Advanced Functional Materials*, 28(10):1704993, 2018. ISSN 1616-3028. doi: 10.1002/adfm.201704993. URL https://onlinelibrary.wiley.com/doi/abs/10.1002/adfm.201704993.

[29] Carlota Ruiz de Galarreta, Arseny Alexeev, Jacopo Bertolotti, and C. David Wright. Phase-Change Metasurfaces for Dyamic Beam Steering and Beam Shaping in the Infrared. In *2018 IEEE International Symposium on Circuits and Systems (ISCAS)*, pages 1–5, May 2018. doi: 10.1109/ISCAS.2018.8351784.

[30] Gregory Kaplan, Koray Aydin, and Jacob Scheuer. Dynamically controlled plasmonic nano-antenna phased array utilizing vanadium dioxide [Invited]. *Optical Materials Express*, 5(11):2513–2524, November 2015. ISSN 2159-3930. doi: 10.1364/OME.5.002513. URL https://opg.optica.org/ome/abstract.cfm?uri=ome-5-11-2513.

[31] Antonio Cala' Lesina, Antonio Cala' Lesina, Antonio Cala' Lesina, Antonio Cala' Lesina, Antonio Cala' Lesina, Antonio Cala' Lesina, Dominic Goodwill, Eric Bernier, Lora Ramunno, Lora Ramunno, Pierre Berini, Pierre Berini, and Pierre Berini. On the performance of optical phased array technology for beam steering: effect of pixel limitations. *Optics Express*, 28(21):31637–31657, October 2020. ISSN 1094-4087. doi: 10.1364/OE.402894. URL https://opg.optica.org/oe/abstract.cfm?uri=oe-28-21-31637.

[32] R. Haupt. Reducing grating lobes due to subarray amplitude tapering. *IEEE Transactions on Antennas and Propagation*, 33(8):846–850, August 1985. ISSN 1558-2221. doi: 10.1109/TAP.1985.1143682. Conference Name: IEEE Transactions on Antennas and Propagation.

[33] Yuanyuan Cui, Yujie Ke, Chang Liu, Zhang Chen, Ning Wang, Liangmiao Zhang, Yang Zhou, Shancheng Wang, Yanfeng Gao, and Yi Long. Thermochromic VO2 for Energy-Efficient Smart Windows. *Joule*, 2(9):1707–1746, September 2018. ISSN 2542-4351. doi: 10.1016/j.joule.2018.06.018. URL https://www.sciencedirect.com/science/article/pii/S2542435118302836.

[34] Sumaiya Kabir, Shruti Nirantar, Liangchen Zhu, Cuong Ton-That, Shubhendra Kumar Jain, Aminuddin Bin Ahmad Kayani, Billy J. Murdoch, Sharath Sriram, Sumeet Walia, and Madhu Bhaskaran. Phase change vanadium dioxide light sensors. *Applied Materials Today*, 21:100833, December 2020. ISSN 2352-9407. doi: 10.1016/j.apmt.2020.100833. URL https://www.sciencedirect.com/science/article/pii/S235294072030281X.

[35] Miao Sun, Mohammad Taha, Sumeet Walia, Madhu Bhaskaran, Sharath Sriram, William Shieh, and Ranjith Rajasekharan Unnithan. A Photonic Switch Based on a Hybrid Combination of Metallic Nanoholes and Phase-change Vanadium Dioxide. *Scientific Reports*, 8(1):11106, July 2018. ISSN 2045-2322. doi: 10.1038/s41598-018-29476-6. URL https://www.nature.com/articles/s41598-018-29476-6. Number: 1 Publisher: Nature Publishing Group.

[36] Elisabetta Corti, Bernd Gotsmann, Kirsten Moselund, Adrian M. Ionescu, John Robertson, and Siegfried Karg. Scaled resistively-coupled VO2 oscillators for neuromorphic computing. *Solid-State Electronics*, 168:107729, June 2020. ISSN 0038-1101. doi: 10.1016/j.sse.2019.107729. URL https://www.sciencedirect.com/science/article/pii/S0038110119307324.

[37] Tero Timonen. X-Ray Diffraction Studies of VO2 Thin Films. page 68.

[38] Hisao Futaki and Minoru Aoki. Effects of Various Doping Elements on the Transition Temperature of Vanadium Oxide Semiconductors. *Japanese Journal of Applied Physics*, 8(8):1008–1013, August 1969. ISSN 0021-4922, 1347-4065. doi: 10.1143/JJAP.8.1008. URL https://iopscience.iop.org/article/10.1143/JJAP.8.1008.

[39] Hans W. Verleur, A. S. Barker, and C. N. Berglund. Optical Properties of V${\textbackslashmathrm{O}}_{2}$ between 0.25 and 5 eV. *Physical Review*, 172(3):788–798, August 1968. doi: 10.1103/PhysRev.172.788. URL https://link.aps.org/doi/10.1103/PhysRev.172.788.

[40] Erieta-Katerina Koussi, Florent Bourquard, Teddy Tite, Damien Jamon, Florence Garrelie, and Yves Jourlin. Synthesis of vanadium oxides by pulsed laser deposition and rapid thermal annealing. *Applied Surface Science*, 521:146267, August 2020. ISSN 0169-4332. doi: 10.1016/j.apsusc.2020.146267. URL https://www.sciencedirect.com/science/article/pii/S0169433220310230.

[41] Stephen Cunningham, Stephen Cunningham, Calin Hrelescu, Calin Hrelescu, and A. Louise Bradley. Plasmonic nanodiscs on vanadium dioxide thin films for tunable luminescence enhancement. *Optics Express*, 29(14):22288–22298, July 2021. ISSN 1094-4087. doi: 10.1364/OE.434135. URL https://opg.optica.org/oe/abstract.cfm?uri=oe-29-14-22288.

[42] Marc Currie, Michael A. Mastro, and Virginia D. Wheeler. Atomic Layer Deposition of Vanadium Dioxide and a Temperature-dependent Optical Model. *JoVE (Journal of Visualized Experiments)*, (135):e57103, May 2018. ISSN 1940-087X. doi: 10.3791/57103. URL https://www.jove.com/v/57103/atomic-layer-deposition-vanadium-dioxide-temperature-dependent.

[43] Zewei Shao, Xun Cao, Hongjie Luo, and Ping Jin. Recent progress in the phase-transition mechanism and modulation of vanadium dioxide materials. *NPG Asia Materials*, 10(7):581–605, July 2018. ISSN 1884-4049, 1884-4057. doi: 10.1038/s41427-018-0061-2. URL http://www.nature.com/articles/s41427-018-0061-2.

[44] Hyun-Tak Kim, Byung-Gyu Chae, Doo-Hyeb Youn, Sung-Lyul Maeng, Gyungock Kim, Kwang-Yong Kang, and Yong-Sik Lim. Mechanism and observation of Mott transition in VO$\less$sub$\greater$2$\less$/sub$\greater$-based two- and three-terminal devices. *New Journal of Physics*, 6:52–52, May 2004. ISSN 1367-2630. doi: 10.1088/1367-2630/6/1/052. URL https://doi.org/10.1088/1367-2630/6/1/052. Publisher: IOP Publishing.

[45] A. Cavalleri, Cs. Tóth, C. W. Siders, J. A. Squier, F. Ráksi, P. Forget, and J. C. Kieffer. Femtosecond Structural Dynamics in ${\textbackslashmathrm{VO}}_{2}$ during an Ultrafast Solid-Solid Phase Transition. *Physical Review Letters*, 87(23):237401, November 2001. doi: 10.1103/PhysRevLett.87.237401. URL https://link.aps.org/doi/10.1103/PhysRevLett.87.237401.

[46] M. M. Qazilbash, A. Tripathi, A. A. Schafgans, Bong-Jun Kim, Hyun-Tak Kim, Zhonghou Cai, M. V. Holt, J. M. Maser, F. Keilmann, O. G. Shpyrko, and D. N. Basov. Nanoscale imaging of the electronic and structural transitions in vanadium dioxide. *Physical Review B*, 83(16):165108, April 2011. doi: 10.1103/PhysRevB.83.165108. URL https://link.aps.org/doi/10.1103/PhysRevB.83.165108.

[47] J. Y. Suh, R. Lopez, L. C. Feldman, and R. F. Haglund. Semiconductor to metal phase transition in the nucleation and growth of VO2 nanoparticles and thin films. *Journal of Applied Physics*, 96(2):1209–1213, July 2004. ISSN 0021-8979. doi: 10.1063/1.1762995. URL https://aip.scitation.org/doi/10.1063/1.1762995.

[48] Devanshi Bhardwaj, Ankur Goswami, and A. M. Umarji. Synthesis of phase pure vanadium dioxide (VO2) thin film by reactive pulsed laser deposition. *Journal of Applied Physics*, 124(13):135301, October 2018. ISSN 0021-8979. doi: 10.1063/1.5046455. URL https://aip.scitation.org/doi/10.1063/1.5046455.

[49] Syed A. Bukhari, Sooraj Kumar, Pawan Kumar, Sarang P. Gumfekar, Hyun-Joong Chung, Thomas Thundat, and Ankur Goswami. The effect of oxygen flow rate on metal–insulator transition (MIT) characteristics of vanadium dioxide (VO2) thin films by pulsed laser deposition (PLD). *Applied Surface Science*, 529:146995, November 2020. ISSN 0169-4332. doi: 10.1016/j.apsusc.2020.146995. URL https://www.sciencedirect.com/science/article/pii/S0169433220317529.

[50] Nicolas Émond, Ali Hendaoui, Akram Ibrahim, Ibraheem Al-Naib, Tsuneyuki Ozaki, and Mohamed Chaker. Transmission of reactive pulsed laser deposited VO2 films in the THz domain. *Applied Surface Science*, 379:377–383, August 2016. ISSN 0169-4332. doi: 10.1016/j.apsusc.2016.04.018. URL https://www.sciencedirect.com/science/article/pii/S0169433216307589.

[51] Georges Hamaoui, Nicolas Horny, Cindy Lorena Gomez-Heredia, Jorge Andres Ramirez-Rincon, Jose Ordonez-Miranda, Corinne Champeaux, Frederic Dumas-Bouchiat, Juan Jose Alvarado-Gil, Younes Ezzahri, Karl Joulain, and Mihai Chirtoc. Thermophysical characterisation of VO2 thin films hysteresis and its application in thermal rectification. *Scientific Reports*, 9(1):8728, June 2019. ISSN 2045-2322. doi: 10.1038/s41598-019-45436-0. URL https://www.nature.com/articles/s41598-019-45436-0.

[52] Jaewoo Jeong, Nagaphani Aetukuri, Tanja Graf, Thomas D. Schladt, Mahesh G. Samant, and Stuart S. P. Parkin. Suppression of Metal-Insulator Transition in VO2 by Electric Field–Induced Oxygen Vacancy Formation. *Science*, 339(6126):1402–1405, March 2013. doi: 10.1126/science.1230512. URL https://www.science.org/doi/10.1126/science.1230512. Publisher: American Association for the Advancement of Science.

[53] Keisuke Shibuya and Akihito Sawa. Modulation of Metal–Insulator Transition in VO2 by Electrolyte Gating-Induced Protonation. *Advanced Electronic Materials*, 2(2):1500131, 2016. ISSN 2199-160X. doi: 10.1002/aelm.201500131. URL https://onlinelibrary.wiley.com/doi/abs/10.1002/aelm.201500131. _eprint: https://onlinelibrary.wiley.com/doi/pdf/10.1002/aelm.201500131.

[54] A. Tselev, I. A. Luk'yanchuk, I. N. Ivanov, J. D. Budai, J. Z. Tischler, E. Strelcov, A. Kolmakov, and S. V. Kalinin. Symmetry Relationship and Strain-Induced Transitions between Insulating M1 and M2 and Metallic R phases of Vanadium Dioxide. *Nano Letters*, 10(11):4409–4416, November 2010. ISSN 1530-6984. doi: 10.1021/nl1020443. URL https://doi.org/10.1021/nl1020443.

[55] Sung-Hwan Bae, Sangmin Lee, Hyun Koo, Long Lin, Bong Hyun Jo, Chan Park, and Zhong Lin Wang. The Memristive Properties of a Single VO2 Nanowire with Switching Controlled by Self-Heating. *Advanced Materials*, 25(36):5098–5103, 2013. ISSN 1521-4095. doi: 10.1002/adma.201302511. URL https://onlinelibrary.wiley.com/doi/abs/10.1002/adma.201302511. _eprint: https://onlinelibrary.wiley.com/doi/pdf/10.1002/adma.201302511.

[56] C.N. Berglund. Thermal filaments in vanadium dioxide. *IEEE Transactions on Electron Devices*, 16(5):432–437, May 1969. ISSN 1557-9646. doi: 10.1109/T-ED.1969.16773.

[57] Minseok Kim, Junho Jeong, Joyce K. S. Poon, and George V. Eleftheriades. Vanadium-dioxide-assisted digital optical metasurfaces for dynamic wavefront engineering. *JOSA B*, 33(5):980–988, May 2016. ISSN 1520-8540. doi: 10.1364/JOSAB.33.000980. URL https://opg.optica.org/josab/abstract.cfm?uri=josab-33-5-980.

[58] M. Soltani, M. Chaker, E. Haddad, R. V. Kruzelecky, and D. Nikanpour. Optical switching of vanadium dioxide thin films deposited by reactive pulsed laser deposition. *Journal of Vacuum Science & Technology A: Vacuum, Surfaces, and Films*, 22(3):859, 2004. ISSN 07342101. doi: 10.1116/1.1722506. URL http://scitation.aip.org/content/avs/journal/jvsta/22/3/10.1116/1.1722506.

[59] Robert E. Marvel, Robert R. Harl, Valentin Craciun, Bridget R. Rogers, and Richard F. Haglund. Influence of deposition process and substrate on the phase transition of vanadium dioxide thin films. *Acta Materialia*, 91:217–226, June 2015. ISSN 1359-6454. doi: 10.1016/j.actamat.2015.03.009. URL https://www.sciencedirect.com/science/article/pii/S1359645415001664.

[60] Ashok P, Yogesh Singh Chauhan, and Amit Verma. Vanadium dioxide thin films synthesized using low thermal budget atmospheric oxidation. *Thin Solid Films*, 706:138003, July 2020. ISSN 0040-6090. doi: 10.1016/j.tsf.2020.138003. URL https://www.sciencedirect.com/science/article/pii/S0040609020302170.

[61] Joyeeta Nag, E. Andrew Payzant, Karren L. More, and Richard F. Haglund. Enhanced performance of room-temperature-grown epitaxial thin films of vanadium dioxide. *Applied Physics Letters*, 98(25):251916, June 2011. ISSN 0003-6951. doi: 10.1063/1.3600333. URL https://aip.scitation.org/doi/full/10.1063/1.3600333.

[62] Amar Srivastava, Helene Rotella, Surajit Saha, Banabir Pal, Gopinadhan Kalon, Sinu Mathew, Mallikarjuna Motapothula, Michal Dykas, Ping Yang, Eiji Okunishi, D. D. Sarma, and T. Venkatesan. Selective growth of single phase VO2(A, B, and M) polymorph thin films. *APL Materials*, 3(2):026101, February 2015. doi: 10.1063/1.4906880. URL https://aip.scitation.org/doi/10.1063/1.4906880.

[63] Ryan McGee, Ankur Goswami, Behnam Khorshidi, Kristi McGuire, Kalvin Schofield, and Thomas Thundat. Effect of process parameters on phase stability and metal-insulator transition of vanadium dioxide (VO2) thin films by pulsed laser deposition. *Acta Materialia*, 137:12–21, September 2017. ISSN 1359-6454. doi: 10.1016/j.actamat.2017.07.025. URL https://www.sciencedirect.com/science/article/pii/S1359645417305864.

[64] Deyi Fu, Kai Liu, Tao Tao, Kelvin Lo, Chun Cheng, Bin Liu, Rong Zhang, Hans A. Bechtel, and Junqiao Wu. Comprehensive study of the metal-insulator transition in pulsed laser deposited epitaxial VO2 thin films. *Journal of Applied Physics*, 113(4):043707, January 2013. ISSN 0021-8979. doi: 10.1063/1.4788804. URL https://aip.scitation.org/doi/full/10.1063/1.4788804.

[65] Sam Lin, Yixin Chen, and Zi Jing Wong. High-performance optical beam steering with nanophotonics. *Nanophotonics*, March 2022. ISSN 2192-8614. doi: 10.1515/nanoph-2021-0805. URL https://www.degruyter.com/document/doi/10.1515/nanoph-2021-0805/html?lang=en.

[66] Seyedeh Mahsa Kamali, Ehsan Arbabi, Amir Arbabi, and Andrei Faraon. A review of dielectric optical metasurfaces for wavefront control. *Nanophotonics*, 7(6):1041–1068, June 2018. ISSN 2192-8614. doi: 10.1515/nanoph-2017-0129. URL https://www.degruyter.com/document/doi/10.1515/nanoph-2017-0129/html.

[67] Fei Ding, Anders Pors, and Sergey I. Bozhevolnyi. Gradient metasurfaces: a review of fundamentals and applications. *Reports on Progress in Physics*, 81(2):026401, December 2017. ISSN 0034-4885. doi: 10.1088/1361-6633/aa8732. URL https://doi.org/10.1088/1361-6633/aa8732.

[68] Longfang Zou, Withawat Withayachumnankul, Charan M. Shah, Arnan Mitchell, Madhu Bhaskaran, Sharath Sriram, and Christophe Fumeaux. Dielectric resonator nanoantennas at visible frequencies. *Optics Express*, 21(1):1344–1352, January 2013. ISSN 1094-4087. doi: 10.1364/OE.21.001344. URL https://opg.optica.org/oe/abstract.cfm?uri=oe-21-1-1344.

[69] Cheng Hung Chu, Ming Lun Tseng, Jie Chen, Pin Chieh Wu, Yi-Hao Chen, Hsiang-Chu Wang, Ting-Yu Chen, Wen Ting Hsieh, Hui Jun Wu, Greg Sun, and Din Ping Tsai. Active dielectric metasurface based on phase-change medium. *Laser & Photonics Reviews*, 10(6):986–994, 2016. ISSN 1863-8899. doi: 10.1002/lpor.201600106. URL https://onlinelibrary.wiley.com/doi/abs/10.1002/lpor.201600106.

[70] Yao-Wei Huang, Ho Wai Howard Lee, Ruzan Sokhoyan, Ragip A. Pala, Krishnan Thyagarajan, Seunghoon Han, Din Ping Tsai, and Harry A. Atwater. Gate-Tunable Conducting Oxide Metasurfaces. *Nano Letters*, 16(9):5319–5325, September 2016. ISSN 1530-6984. doi: 10.1021/acs.nanolett.6b00555. URL https://doi.org/10.1021/acs.nanolett.6b00555.

[71] Jordan A. Ramsey, Kendrick Q. Henderson, and Nima Ghalichechian. Reconfigurable Reflectarray Unit Cell using Vanadium Dioxide. In *2021 IEEE International Symposium on Antennas and Propagation and USNC-URSI Radio Science Meeting (APS/URSI)*, pages 1763–1764, December 2021. doi: 10.1109/APS/URSI47566.2021.9704486.

[72] Tie Jun Cui, Mei Qing Qi, Xiang Wan, Jie Zhao, and Qiang Cheng. Coding metamaterials, digital metamaterials and programmable metamaterials. *Light: Science & Applications*, 3(10):e218–e218, October 2014. ISSN 2047-7538. doi: 10.1038/lsa.2014.99. URL https://www.nature.com/articles/lsa201499.

[73] Lianlin Li, Tie Jun Cui, Wei Ji, Shuo Liu, Jun Ding, Xiang Wan, Yun Bo Li, Menghua Jiang, Cheng-Wei Qiu, and Shuang Zhang. Electromagnetic reprogrammable coding-metasurface holograms. *Nature Communications*, 8(1):197, August 2017. ISSN 2041-1723. doi: 10.1038/s41467-017-00164-9. URL https://www.nature.com/articles/s41467-017-00164-9.

[74] Vedaprabhu Basavarajappa, Beatriz Bedia Exposito, Lorena Cabria, and Jose Basterrechea. Binary phase-controlled multi-beam-switching antenna array for reconfigurable 5G applications. *EURASIP Journal on Wireless Communications and Networking*, 2019(1):180, July 2019. ISSN 1687-1499. doi: 10.1186/s13638-019-1508-z. URL https://doi.org/10.1186/s13638-019-1508-z.

[75] Karel Acoleyen, Wim Bogaerts, Jana Jágerská, Nicolas Thomas, Romuald Houdré, and Roel Baets. Off-chip beam steering with a one-dimensional optical phased array. *Optics letters*, 34:1477–9, June 2009. doi: 10.1364/OL.34.001477.

[76] Kane Yee. Numerical solution of initial boundary value problems involving maxwell's equations in isotropic media. *IEEE Transactions on Antennas and Propagation*, 14(3):302–307, May 1966. ISSN 1558-2221. doi: 10.1109/TAP.1966.1138693. Conference Name: IEEE Transactions on Antennas and Propagation.

[77] John B Schneider. Understanding the Finite-Difference Time-Domain Method. page 403.

[78] PML boundary conditions in FDTD and MODE, . URL https://optics.ansys.com/hc/en-us/articles/360034382674-PML-boundary-conditions-in-FDTD-and-MODE. Publication Title: Lumerical Support.

[79] Frequency-domain Profile and Power monitor - Simulation object, . URL https://optics.ansys.com/hc/en-us/articles/360034902393-Frequency-domain-Profile-and-Power-monitor-Simulation-object. Publication Title: Lumerical Support.

[80] Sawyer D. Campbell, David Sell, Ronald P. Jenkins, Eric B. Whiting, Jonathan A. Fan, and Douglas H. Werner. Review of numerical optimization techniques for meta-device design. *Optical Materials Express*, 9(4):1842–1863, April 2019. ISSN 2159-3930. doi: 10.1364/OME.9.001842. URL https://opg.optica.org/ome/abstract.cfm?uri=ome-9-4-1842. Publisher: Optica Publishing Group.

[81] Wenhui Zhu, Guang Zheng, Sen Cao, and Hu He. Thermal conductivity of amorphous SiO2 thin film: A molecular dynamics study. *Scientific Reports*, 8:10537, July 2018. ISSN 2045-2322. doi: 10.1038/s41598-018-28925-6. URL https://www.ncbi.nlm.nih.gov/pmc/articles/PMC6043512/.

[82] Tun Cao, Guangzhao Zheng, Shuai Wang, and Chenwei Wei. Ultrafast beam steering using gradient Au- Ge_2Sb_2Te_5 -Au plasmonic resonators. *Optics Express*, 23(14):18029–18039, July 2015. ISSN 1094-4087. doi: 10.1364/OE.23.018029. URL https://opg.optica.org/oe/abstract.cfm?uri=oe-23-14-18029.

[83] Dong-Wook Oh, Changhyun Ko, Shriram Ramanathan, and David G. Cahill. Thermal conductivity and dynamic heat capacity across the metal-insulator transition in thin film VO2. *Applied Physics Letters*, 96(15):151906, April 2010. ISSN 0003-6951. doi: 10.1063/1.3394016. URL https://aip.scitation.org/doi/10.1063/1.3394016.

[84] C. Durkan, M. A. Schneider, and M. E. Welland. Analysis of failure mechanisms in electrically stressed Au nanowires. *Journal of Applied Physics*, 86(3):1280–1286, August 1999. ISSN 0021-8979. doi: 10.1063/1.370882. URL https://aip.scitation.org/doi/10.1063/1.370882.

[85] Clemens J. M. Lasance. How to Estimate Heat Spreading Effects in Practice. *Journal of Electronic Packaging*, 132(3), September 2010. ISSN 1043-7398. doi: 10.1115/1.4001856. URL https://doi.org/10.1115/1.4001856.

[86] A. J. Robinson, J. Colenbrander, R. Kempers, and R. Chen. Solid and Vapor Chamber Integrated Heat Spreaders: Which to Choose and Why. *IEEE Transactions on Components, Packaging and Manufacturing Technology*, 8(9):1581–1592, September 2018. ISSN 2156-3985. doi: 10.1109/TCPMT.2018.2822400.

[87] Elissa Klopfer, Sahil Dagli, David Barton, Mark Lawrence, and Jennifer A. Dionne. High-Quality-Factor Silicon-on-Lithium Niobate Metasurfaces for Electro-optically Reconfigurable Wavefront Shaping. *Nano Letters*, 22(4):1703–1709, February 2022. ISSN 1530-6984. doi: 10.1021/acs.nanolett.1c04723. URL https://doi.org/10.1021/acs.nanolett.1c04723.

[88] stackrt - Script command, . URL https://optics.ansys.com/hc/en-us/articles/360034406254-stackrt-Script-command.

[89] Byoungsu Ko, Trevon Badloe, Soo-Jung Kim, Sung-Hoon Hong, and Junsuk Rho. Employing vanadium dioxide nanoparticles for flexible metasurfaces with switchable absorption properties at near-infrared frequencies. *Journal of Optics*, 22(11):114002, October 2020. ISSN 2040-8986. doi: 10.1088/2040-8986/abbc55. URL https://doi.org/10.1088/2040-8986/abbc55. Publisher: IOP Publishing.

[90] Sandeep Kumar Chamoli, Gopal Verma, Subhash C. Singh, and Chunlei Guo. Phase change material-based nano-cavity as an efficient optical modulator. *Nanotechnology*, 32(9):095207, December 2020. ISSN 0957-4484. doi: 10.1088/1361-6528/abcb7a. URL https://doi.org/10.1088/1361-6528/abcb7a. Publisher: IOP Publishing.

[91] Xike Li, Shiwei Tang, Fei Ding, Shuomin Zhong, Yuanqing Yang, Tao Jiang, and Jun Zhou. Switchable multifunctional terahertz metasurfaces employing vanadium dioxide. *Scientific Reports*, 9(1):5454, April 2019. ISSN 2045-2322. doi: 10.1038/s41598-019-41915-6. URL https://www.nature.com/articles/s41598-019-41915-6.

[92] Guoping Wang, Xuechen Chen, Sheng Liu, Chingping Wong, and Sheng Chu. Mechanical Chameleon through Dynamic Real-Time Plasmonic Tuning. *ACS Nano*, 10(2):1788–1794, February 2016. ISSN 1936-0851. doi: 10.1021/acsnano.5b07472. URL https://doi.org/10.1021/acsnano.5b07472.

[93] Shichao Song, Xiaoliang Ma, Mingbo Pu, Xiong Li, Yinghui Guo, Ping Gao, and Xiangang Luo. Tailoring active color rendering and multiband photodetection in a vanadium-dioxide-based metamaterial absorber. *Photonics Research*, 6(6):492–497, June 2018. ISSN 2327-9125. doi: 10.1364/PRJ.6.000492. URL https://opg.optica.org/prj/abstract.cfm?uri=prj-6-6-492.

[94] K. Wilson, C. A. Marocico, and A. L. Bradley. Dynamic structural colour using vanadium dioxide thin films. *Journal of Physics D: Applied Physics*, 51(25):255101, May 2018. ISSN 0022-3727. doi: 10.1088/1361-6463/aac47c. URL https://doi.org/10.1088/1361-6463/aac47c. Publisher: IOP Publishing.

[95] Benjamin M W Baggett. Optimization of Aperiodically Spaced Phased Arrays for Wideband Applications. page 137.

[96] Prachi Thureja, Ghazaleh Kafaie Shirmanesh, Katherine T. Fountaine, Ruzan Sokhoyan, Meir Grajower, and Harry A. Atwater. Array-Level Inverse Design of Beam Steering Active Metasurfaces. *ACS Nano*, 14(11):15042–15055, November 2020. ISSN 1936-0851. doi: 10.1021/acsnano.0c05026. URL https://doi.org/10.1021/acsnano.0c05026.

[97] Ryan McGee, Ankur Goswami, Soupitak Pal, Kalvin Schofield, Syed Asad Manzoor Bukhari, and Thomas Thundat. Sharpness and intensity modulation of the metal-insulator transition in ultrathin ${\mathrm{VO}}_{2}$ films by interfacial structure manipulation. *Physical Review Materials*, 2(3):034605, March 2018. doi: 10.1103/PhysRevMaterials.2.034605. URL https://link.aps.org/doi/10.1103/PhysRevMaterials.2.034605. Publisher: American Physical Society.

[98] Mark Borek, F. Qian, V. Nagabushnam, and R. K. Singh. Pulsed laser deposition of oriented VO2 thin films on R-cut sapphire substrates. *Applied Physics Letters*, 63(24):3288–3290, December 1993. ISSN 0003-6951. doi: 10.1063/1.110177. URL https://aip.scitation.org/doi/10.1063/1.110177. Publisher: American Institute of Physics.

[99] Slimane Lafane, Smail Malek, Jackie Nel, and Samira Abdelli-Messaci. Room temperature and high-pressure-pulsed laser deposition of nanocrystalline VO2 thin films on glass substrate: plasma and film analyses. *Applied Physics A*, 127(1):75, January 2021. ISSN 1432-0630. doi: 10.1007/s00339-020-04174-1. URL https://doi.org/10.1007/s00339-020-04174-1.

[100] Devanshi Bhardwaj, Deependra Kumar Singh, S. B. Krupanidhi, and A. M. Umarji. Fabrication of smooth thin film of vanadium oxides ($$\hbox {VO}_x$$) using pulsed laser deposition. *Applied Physics A*, 126(3):157, February 2020. ISSN 1432-0630. doi: 10.1007/s00339-020-3310-5. URL https://doi.org/10.1007/s00339-020-3310-5.

[101] S. Lysenko, A. Rúa, V. Vikhnin, F. Fernández, and H. Liu. Insulator-to-metal phase transition and recovery processes in ${\mathrm{V}}{\mathrm{O}}_{2}$ thin films after femtosecond laser excitation. *Physical Review B*, 76(3):035104, July 2007. doi: 10.1103/PhysRevB.76.035104. URL https://link.aps.org/doi/10.1103/PhysRevB.76.035104. Publisher: American Physical Society.

[102] D. H. Kim and H. S. Kwok. Pulsed laser deposition of VO2 thin films. *Applied Physics Letters*, 65(25):3188, June 1998. ISSN 0003-6951. doi: 10.1063/1.112476. URL https://aip.scitation.org/doi/abs/10.1063/1.112476. Publisher: American Institute of PhysicsAIP.

Appendix A

Appendix

The optimisation algorithm setup used on matlab (requires the global optimisation toolbox) can be found below :

```
x0 = (lb+ub)/2 ; %typical x value between the boundaries
% Hybrid optimisation : fmincon settings
options_fmincon = optimoptions('fmincon');
options_fmincon = optimoptions(options_fmincon,'Algorithm','sqp'); %alt: sqp
options_fmincon = optimoptions(options_fmincon,'MaxIter', 20);
options_fmincon = optimoptions(options_fmincon,'TypicalX', x0);
options_fmincon = optimoptions(options_fmincon,'PlotFcns', { @optimplotfval });
options_fmincon = optimoptions(options_fmincon,'Display','iter-detailed');
options_fmincon = optimoptions(options_fmincon,'DiffMaxChange',0.02);
options_fmincon = optimoptions(options_fmincon,'FiniteDifferenceStepSize',0.02);

% Main optimization settings
options = optimoptions('particleswarm') ;
options = optimoptions(options, 'Display', 'iter');
options = optimoptions(options,'MaxIterations', 40);
options = optimoptions(options,'MaxTime',10*3600);
options = optimoptions(options,'SwarmSize',100);
options = optimoptions(options,'HybridFcn', {@fmincon, options_fmincon}); %use this
    line to activate hybrid optimisation
```

The number of iterations, maximum time and swarm size were varied during the project, the values shown above were typical of an overnight simulation. The dimensions were expressed in nm (for the FiniteDifferenceStepSize setting).

The table in the two following pages is a brief summary of the literature around pulsed laser deposition of VO_2 thin film and aggregates the deposition conditions in these studies.

Reference	Study year	Phase formed	$T°$ ($C°$)	Substrate	base pressure	O_2 pressure	Pulse energy	Pulse rate	Fluence	Target distance	Notes
[97]	2018	VO2 M1	400	c-sapphire (0001)	1e-5 torr	100e-3 torr	0.078 J	10 Hz	2.6 J/cm2	31mm	
[97]	2018	VO2 A	500	c-sapphire (0001)	1e-5 torr	100e-3 torr	0.078 J	10 Hz	2.6 J/cm2	31mm	
[97]	2018	VO2 M1	550	c-sapphire (0001)	1e-5 torr	100e-3 torr	0.078 J	10 Hz	2.6 J/cm2	31mm	
[97]	2018	VO2 M1	600	c-sapphire (0001)	1e-5 torr	100e-3 torr	0.078 J	10 Hz	2.6 J/cm2	31mm	
[97]	2018	VO2 mixed	400	p-Si (100)	1e-5 torr	100e-3 torr	0.078 J	10 Hz	2.6 J/cm2	31mm	
[97]	2018	VO2 A	500	p-Si (100)	1e-5 torr	100e-3 torr	0.078 J	10 Hz	2.6 J/cm2	31mm	
[97]	2018	VO2 M1	550	p-Si (100)	1e-5 torr	100e-3 torr	0.078 J	10 Hz	2.6 J/cm2	31mm	
[97]	2018	VO2 M1	600	p-Si (100)	1e-5 torr	100e-3 torr	0.078 J	10 Hz	2.6 J/cm2	31mm	
[97]	2018	VO2	600	SiO2	1e-5 torr	50e-3 torr	0.078 J	10 Hz	2.6 J/cm2	31mm	Optimised value from Taguchi method
[49]	2020	VO1.838	600	Si/SiO2	1.5e-6 mbar	50 e-3 torr	-	11 Hz	2.6 J/cm2	31mm	0_2 flow : 0.5 sccm
[49]	2020	VO1.304	600	Si/SiO2	1.5e-6 mbar	50e-3 torr	-	12 Hz	2.6 J/cm2	31mm	0_2 flow : 1 sccm
[49]	2020	VO1.732	600	Si/SiO2	1.5e-6 mbar	50 e-3 torr	-	12 Hz	2.6 J/cm2	31mm	0_2 flow : 5 sccm
[49]	2020	VO2.367	600	Si/SiO2	1.5e-6 mbar	50 e-3 torr	-	13 Hz	2.6 J/cm2	31mm	0_2 flow : 10 sccm
[49]	2020	VO2.081	600	Si/SiO2	1.5e-6 mbar	50 e-3 torr	-	14 Hz	2.6 J/cm2	31mm	0_2 flow : 30 sccm
[49]	2020	VO1.353	600	Si/SiO2	1.5e-6 mbar	50 e-3 torr	-	15 Hz	2.6 J/cm2	31mm	0_2 flow : 50 sccm
[49]	2020	VO2.300	600	Si/SiO2	1.5e-6 mbar	50 e-3 torr	-	16 Hz	2.6 J/cm2	31mm	0_2 flow : 90 sccm
[62]	2015	VO2 A, B and M	500	SrTiO3	-	[0.1-7.5] e-3 torr	-	[2–¿10] Hz	2J/cm2	-	A phase diagram was obtained for A, B and M_1 VO_2
[48]	2018	V2O3	600	Si/SiO2	1e-6 torr	1e-4 torr	-	10	2.6J/cm2	31mm	
[48]	2018	V2O3	600	Si/SiO2	1e-6 torr	5e-4 torr	-	10	2.6J/cm2	31mm	
[48]	2018	V2O3	600	Si/SiO2	1e-6 torr	1e-3 torr	-	10	2.6J/cm2	31mm	
[48]	2018	VO2	600	Si/SiO2	1e-6 torr	1e-2 torr	-	10	2.6J/cm2	31mm	
[48]	2018	VO2	600	Si/SiO2	1e-6 torr	5e-2 torr	-	10	2.6J/cm2	31mm	
[48]	2018	V2O5	600	Si/SiO2	1e-6 torr	1e-1 torr	-	10	2.6J/cm2	31mm	
[97]	2018	VO2 M1	400	c-sapphire (0001)	1e-5 torr	100e-3 torr	0.078 J	10 Hz	2.6 J/cm2	31mm	
[97]	2018	VO2 A	500	c-sapphire (0001)	1e-5 torr	100e-3 torr	0.078 J	10 Hz	2.6 J/cm2	31mm	
[97]	2018	VO2 M1	550	c-sapphire (0001)	1e-5 torr	100e-3 torr	0.078 J	10 Hz	2.6 J/cm2	31mm	
[97]	2018	VO2 M1	600	c-sapphire (0001)	1e-5 torr	100e-3 torr	0.078 J	10 Hz	2.6 J/cm2	31mm	
[97]	2018	VO2 mixed	400	p-Si (100)	1e-5 torr	100e-3 torr	0.078 J	10 Hz	2.6 J/cm2	31mm	
[97]	2018	VO2 A	500	p-Si (100)	1e-5 torr	100e-3 torr	0.078 J	10 Hz	2.6 J/cm2	31mm	
[97]	2018	VO2 M1	550	p-Si (100)	1e-5 torr	100e-3 torr	0.078 J	10 Hz	2.6 J/cm2	31mm	
[97]	2018	VO2 M1	600	p-Si (100)	1e-5 torr	100e-3 torr	0.078 J	10 Hz	2.6 J/cm2	31mm	
[97]	2018	VO2	600	SiO2	1e-5 torr	50e-3 torr	0.078 J	10 Hz	2.6 J/cm2	31mm	Optimised value from Taguchi method
[62]	2015	VO2 A, B and M	500	SrTiO3	-	[0.1-7.5] e-3 torr	-	[2–¿10] Hz	2J/cm2	-	A phase diagram was obtained for A, B and M_1 VO_2
[48]	2018	V2O3	600	Si/SiO2	1e-6 torr	1e-4 torr	-	10	2.6J/cm2	31mm	
[48]	2018	V2O3	600	Si/SiO2	1e-6 torr	5e-4 torr	-	10	2.6J/cm2	31mm	
[48]	2018	V2O3	600	Si/SiO2	1e-6 torr	1e-3 torr	-	10	2.6J/cm2	31mm	
[48]	2018	VO2	600	Si/SiO2	1e-6 torr	1e-2 torr	-	10	2.6J/cm2	31mm	
[48]	2018	VO2	600	Si/SiO2	1e-6 torr	5e-2 torr	-	10	2.6J/cm2	31mm	
[48]	2018	V2O5	600	Si/SiO2	1e-6 torr	1e-1 torr	-	10	2.6J/cm2	31mm	
[50]	2015	VO2	500	SiO2	1e-5 torr	[2-25] e-3 torr	-	10 Hz	2J/cm2	65mm	

Reference	Study year	Phase formed	T° (°C)	Substrate	base pressure	O_2 pressure	Pulse energy	Pulse rate	Fluence	Target distance	Notes
[49]	2020	VO1.838	600	Si/SiO2	1.5e-6 mbar	50 e-3 torr	-	11 Hz	2.6 J/cm2	31mm	0_2 flow : 0.5 sccm
[49]	2020	VO1.304	600	Si/SiO2	1.5e-6 mbar	50e-3 torr	-	12 Hz	2.6 J/cm2	31mm	0_2 flow : 1 sccm
[49]	2020	VO1.732	600	Si/SiO2	1.5e-6 mbar	50 e-3 torr	-	12 Hz	2.6 J/cm2	31mm	0_2 flow : 5 sccm
[49]	2020	VO2.367	600	Si/SiO2	1.5e-6 mbar	50 e-3 torr	-	13 Hz	2.6 J/cm2	31mm	0_2 flow : 10 sccm
[49]	2020	VO2.081	600	Si/SiO2	1.5e-6 mbar	50 e-3 torr	-	14 Hz	2.6 J/cm2	31mm	0_2 flow : 30 sccm
[49]	2020	VO1.353	600	Si/SiO2	1.5e-6 mbar	50 e-3 torr	-	15 Hz	2.6 J/cm2	31mm	0_2 flow : 50 sccm
[49]	2020	VO2.300	600	Si/SiO2	1.5e-6 mbar	50 e-3 torr	-	16 Hz	2.6 J/cm2	31mm	0_2 flow : 90 sccm
[98]	1993	VO2	500-525	Al2O3	-	1 e-2 torr	-	-	-	-	
[40]	2020	VO2	RT	TiO2 on SiO2 - Si - quartz - fused silica	1.8e-7 mbar	0.1-30	117 mJ	10Hz	5J/cm2	50mm	
[99]	2021	VO2 - A	RT	Corning glass (1737)	-	5 mbar		5 Hz	2 J/cm2	11 mm	-
[100]	2020	V2O3 + V2O5	500	Si/SiO2	1e-6 torr	1e-3 mbar	200 mJ	10Hz		35mm	
[100]	2020	V3O5	600	Si/SiO2	1e-6 torr	1e-3 mbar	150 mJ	10Hz		30mm	
[100]	2020	V3O5	700	Si/SiO2	1e-6 torr	1e-3 mbar	100 mJ	10Hz		40mm	
[100]	2020	V3O5	500	Si/SiO2	1e-6 torr	7.5e-3 mbar	100 mJ	10Hz		30mm	
[100]	2020	VO2	600	Si/SiO2	1e-6 torr	7.5e-3 mbar	200 mJ	10Hz		40mm	
[100]	2020	V7O16	700	Si/SiO2	1e-6 torr	7.5e-3 mbar	100 mJ	10Hz		35mm	
[100]	2020	V7O16	500	Si/SiO2	1e-6 torr	5e-2 mbar	100 mJ	10Hz		40mm	
[100]	2020	VO2	600	Si/SiO2	1e-6 torr	5e-2 mbar	150 mJ	10Hz		35mm	
[100]	2020	VO2	700	Si/SiO2	1e-6 torr	5e-2 mbar	100 mJ	10Hz		30mm	
[101]	2007	VO2	550	SiO2	-	30 e-3 torr	-	10Hz	4 J/cm2	-	
[101]	2007	VO2	550	MgO	-	30 e-3 torr	-	10Hz	4 J/cm2	-	
[101]	2007	VO2	550	Al2O3	-	30 e-3 torr	-	10Hz	4 J/cm2	-	
[102]	1994	VO2	630	(0001) Al2O3	10e-5 torr	20e-3 torr			2-3 J/cm2	50mm	V_2O_3 target
[102]	1994	VO2	630	(1010) Al2O3	10e-5 torr	30e-3 torr			2-3J/cm2	50mm	V_2O_3 target
[58]	2004	VO2	520	SiO2/(100)Si/(1000 Al2O3)	-	2.25 to 4.5e-3 torr	-	-	5J/cm2	-	
[59]	2015	VO2/V2O5 (35/65)	RT	(100) Si	9e-7 torr	11e-3 torr		25 Hz	4J/cm2	80mm	0_2 flow : 2 sccm post annealing
[59]	2015	VO2/V2O5 (35/65)	RT	(0001) Al2O3	9e-7 torr	11e-3 torr		25 Hz	4J/cm3	80mm	0_2 flow : 2 sccm post annealing
[59]	2015	VO2/V2O5 (35/65)	RT	SiO2 glass (Corning 1737)	9e-7 torr	11e-3 torr		25 Hz	4J/cm4	80mm	0_2 flow : 2 sccm post annealing